High-Fidelity Quantum State Control of a Trapped Molecular Ion

by

Dalton Chaffee

B.S., Purdue University, 2017

M.S., University of Colorado–Boulder, 2020

A thesis submitted to the

Faculty of the Graduate School of the

University of Colorado in partial fulfillment

of the requirements for the degree of

Doctor of Philosophy

Department of Physics

2025

Committee Members:

Chin-wen Chou, Chair

Heather Lewandowski

David J. Nesbitt

Scott Glancy

J. Mathias Weber

Chaffee, Dalton (Ph.D., Physics)

High-Fidelity Quantum State Control of a Trapped Molecular Ion

Thesis directed by Dr. Chin-wen Chou

Ultracold molecules are a promising next-generation platform for quantum information science, precision measurement, and ultracold chemistry. However, quantum state control in molecules remains less developed than in atoms due to the added complexity from their rotational and vibrational degrees of freedom. In this thesis, I describe the development and operation of a cryogenic molecular ion-trapping experiment designed to overcome these challenges using quantum logic spectroscopy techniques. A single molecule is co-trapped with a Ca^+ ion for cooling and readout, while far-detuned Raman beams are used for internal molecular state control. Cryogenically cooled radiation shields reduce the thermal radiation incident upon the trapped molecule, which can drive undesirable rovibrational transitions. The apparatus also features a molecular beam machine for loading a variety of species via resonance-enhanced multiphoton ionization. We demonstrate an unprecedented level of control of a molecule, using an adaptive Bayesian scheme to realize single-state preparation and non-destructive measurement of CaH^+ with a single-state fidelity exceeding 99.4%. The demonstrated techniques are applicable to a broad class of molecular ion species, establishing a robust platform for molecular physics studies with high-fidelity molecular quantum state control.

Dedication

To my father, who taught me how to solve problems—and how to live life.

Acknowledgements

Thank you first to James, my advisor, for setting me up for success in the lab, being receptive to my ideas and needs inside and outside of work, and carefully proofreading this thesis. You have taught me much about being a disciplined and dedicated experimental physicist. Thank you also to Didi, Dave H., and Dave L. for all of the keen technical advice over the years. I was incredibly lucky to have labmates throughout my entire Ph.D. that not only contributed greatly to the science we accomplished and my personal growth as a scientist, but also made the lab a fun place to go every day and proved to be dear friends. Julian, April R., Baruch, and April S.—I would not have made it through without you. Beyond the cryomol team, the entire Ion Storage Group, past and present, has provided a truly welcoming and scientifically stimulating work environment. I will miss you all.

I made many lifelong friends within my program cohort. Thank you in particular to Alex and Giaco, who have provided unfailing friendship throughout my Ph.D. and participated in every annual skyline traverse. Outside of the department, I stumbled upon an amazing collection of humans when I joined the Strangers ultimate team—thank you all for taking me in, loving me, and keeping me sane for the past 6 years.

Thank you to my family for the lifelong love and support. Dad—we miss you every day. Mom—I probably wouldn't be here if you hadn't pushed me into taking physics as a high school sophomore. Jenna—did we manage a Colorado backpacking trip every year? And finally, thank you to Claire, the love of my life, for taking care of me and inspiring me. The whole Ph.D. was worth it just to meet you.

Contents

Chapter

Appendix

Tables

Table

Figures

Figure

Chapter 1

Introduction and Background

In recent years, many new research avenues for scientific discovery in ultracold molecules have been identified and pursued. Molecules have the potential to enable advances in precision measurement, quantum information processing, and cold chemistry. However, these experiments are often limited by the availability of methods for control of the molecules' quantum mechanical states, whereas analogous methods have proven instrumental in catalyzing advances in atomic physics experiments over the last few decades. Developing generalizable, high-fidelity control techniques for molecular quantum states remains a critical step toward unlocking the full potential of cold molecules.

Over the course of my Ph.D., I have designed, constructed, and operated an experiment that exhibits unprecedented quantum-state control of a molecule via quantum-logic spectroscopy techniques applied to a molecular ion trapped in a cryogenic environment; such techniques could be applied to a broad class of molecular species. In this thesis, I will discuss the experimental apparatus and methods, demonstration of high-fidelity state preparation, manipulation, and measurement of CaH^+, and implementation of a molecular beam for loading a wide range of molecular ions. To provide context and motivation, I will begin with an overview of the current state of the field, highlighting both progress and limitations in molecular quantum state control.

1.1 Quantum control of atoms and molecules

Quantum state-level control of atomic systems is a mature field that has enjoyed impressive development in recent decades. A modern atomic physics experiment typically involves doing all of the following operations to the atom(s):

(1) Spatial trapping

(2) Cooling to near the motional ground state in the trap

(3) Quantum state preparation

(4) Interrogating a feature of interest

(5) Quantum state measurement

I henceforth refer to operations 1-3 and 5 as *quantum state control*, whereas operation 4 represents the scientific or technical application of the experiment. Invention, improvement, and extension of quantum state control techniques is often a prerequisite for advancement of applications. For example, development of magneto-optical traps has paved the way to realization of Bose-Einstein Condensates (BECs) [1, 2], while atoms in optical lattice traps [3] and tweezer arrays [4] have expedited novel quantum simulations [5, 6]. Laser cooling techniques have enabled cooling of a trapped atom to its motional ground state, allowing for precision operation and measurement; notable examples include atomic clocks with accuracies better than a part in 10^{-18} [7, 8] and precision measurements of fundamental atomic properties that stretch understanding of the Standard Model [9, 10]. Preparation and measurement of a single quantum state, involving manipulation of internal electronic and hyperfine degrees of freedom, has been demonstrated with near 99.99% fidelity [11, 12] and opens the door for high-fidelity, large-scale quantum computation [13].

Quantum state control has been realized in more than a dozen atomic species.[1] For a given experiment, the species is typically chosen according to the criteria of the application; examples

---

[1] Nine species are represented in the collection of experiments cited in the preceding paragraph alone!

include low sensitivity to external perturbations [7], tunable particle-particle interactions [14], or high sensitivity to the quantity to be measured [15]. A toolbox of quantum state control techniques exists to achieve these criteria across atomic systems. Particles are confined using electromagnetic fields, including radio-frequency ion traps and optical traps for neutral atoms. An electronic transition is chosen for fast (∼ns timescale) cycling (decaying back to the original state after excitation) to allow for efficient cooling from ambient temperature, while manipulation of other electronic and hyperfine transitions may be used for further cooling and state preparation. The cycling transition is then used for efficient state detection.

Molecules are a natural extension to modern atomic physics experiments. Compared to atoms, molecules provide a nearly limitless expansion to the variety of species, and their additional rotational and vibrational degrees of freedom can provide clear advantages in many applications. Indeed, many experiments are already leveraging molecules' capabilities, including in precision measurements [16–19]; demonstrations of molecular quantum gates [20–23], clocks [24], and BECs [25]; and ultracold chemistry investigations [26–28]. Proposed applications of note include enhanced sensitivity to possible variation in the proton-to-electron mass ratio [29], detection of parity violation [30], precision measurement for enhanced understanding of cosmic spectra [31], and quantum information transduction [32] for, e.g., quantum networking.

Despite all of this progress and opportunity, the challenges introduced by molecules' additional degrees of freedom have caused quantum control techniques for molecules to lag well behind those for atoms. Spontaneous decay from an excited electronic level does not, in general, return the molecule to a deterministic vibrational level; instead, it may decay to one of many vibrational levels with branching ratios determined by the Franck-Condon factors (FCFs), precluding fast cycling transitions for cooling and detection. To make matters worse, single photons can drive rotational and vibrational transitions in polar molecules via interaction with the electric dipole moment. As ambient thermal radiation (TR) often has high spectral overlap with molecular rovibrational transitions, this effect can substantially hinder efforts to prepare and keep a molecule in a particular quantum state. The situation is illustrated in Fig. 1.1.

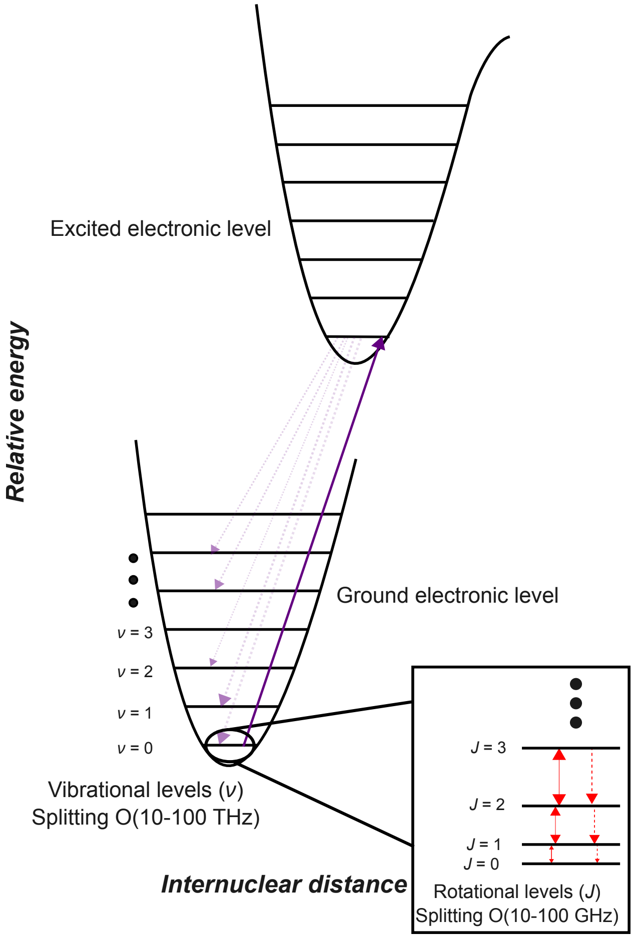

Figure 1.1: Challenges of molecular quantum state control due to vibrational and rotational degrees of freedom. Laser excitation to an excited electronic state (solid purple arrow) does not lead to a cycling transition because spontaneous decay (dashed purple arrows) typically populates multiple vibrational levels. Many rotational levels lie within a vibrational level; thermal radiation (solid red arrows) and spontaneous decay (dashed red arrows) can move the molecule up and down the rotational and vibrational ladders.

A number of strategies exist to overcome the challenges of molecular quantum state control. One example is direct laser cooling of molecules specially-chosen for favorable FCFs, for which decay from an excited state predominantly populates only one or a few vibrational levels; with appropriate repump laser light, efficient photon cycling is then possible [33–36]. An alternative approach is forming molecules directly into the desired quantum state. This has been demonstrated for diatomic neutral molecules by preparing two separate species of atoms in a particular state using standard atomic control techniques, then adiabatically associating the atoms into a molecule [25, 37–39].

However, the scope of these techniques is limited. They are only applicable to specific molecular species and, for experiments using the latter approach, state detection is destructive. To build a broader toolbox for molecular quantum state control, a different strategy is needed.

1.2 Quantum-logic spectroscopy of trapped molecular ions

Performing experiments with molecular ions in ion traps provides several natural advantages over neutral molecules. The trapping mechanism itself is independent of the internal state of the ions. Furthermore, multiple ions confined within the same trapping potential interact strongly due to their mutual Coulomb interaction and will thus have shared motional normal modes. If a molecular ion of interest is co-trapped with a well-controlled atomic *auxiliary* ion, the molecular ion can be sympathetically cooled via the auxiliary ion. A technique known as quantum logic-spectroscopy (QLS) [40] allows information about the molecular ion to be transferred to, and read out from, the auxiliary ion by mapping information about the molecule's internal state onto the shared motion among the ions. Unlike some other methods of molecular quantum-state control, QLS poses few requirements on the internal structure of the molecule, permits preparation in a specific quantum state, and allows for non-destructive state measurement.

QLS techniques have recently been applied to molecular ions with promising results [41–44]. In Ref. [42], resonant multiphoton ionization (REMPI) is used to ionize N_2 preferentially into a particular rotational level for ion trap loading, and a form of QLS is used to detect the presence or absence of the molecule within that rotational manifold[2]; however, preparation of a single quantum state is not demonstrated. In Ref. [43], preparation of a single quantum state of $H_2{}^+$ is demonstrated, but state preparation and measurement (SPAM) fidelities are limited by the quality of quantum-logic operations. These two experiments also benefit from the long rotational state lifetimes afforded by non-polar molecules; in contrast, experiments working with polar molecules [41, 44] must contend with stimulated rotational transitions due to TR.

---

[2] Rotational levels are typically split into multiple sublevels, as discussed in Section 2.1; I will often refer to a rotational level as a *rotational manifold* to stress that it consists of more than one quanum state.

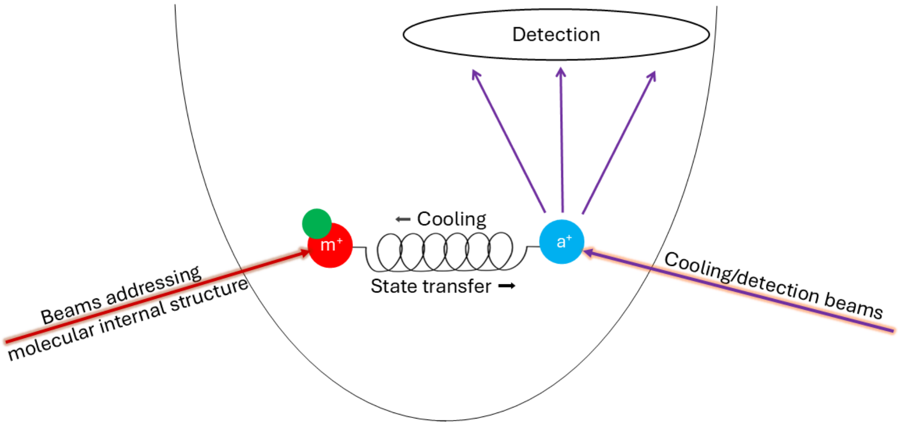

Figure 1.2: Controlling a molecular ion (denoted m^+) with a co-trapped atomic ion (denoted a^+) as the auxiliary ion. The ions' motions are coupled though their mutual Coloumb interaction, allowing for sympathetic cooling and state transfer via QLS techniques.

The experimental apparatus central to my Ph.D. work is a second-generation system that builds upon a room-temperature molecular ion apparatus developed within the NIST Ion Storage Group since 2013. The room-temperature experiment has studied CaH^+ via QLS with a co-trapped Ca^+ ion, driving transitions between molecular states with pairs of far-detuned Raman beams. Novel demonstrations include projective molecular state preparation [44], spectroscopy between rotational manifolds using a frequency comb [45], atom-molecule entanglement [32], precision measurement of the dipole moment of a trapped molecular ion [46], and efficient tracking and reversal of TR effects [47]; select results are shown in Fig. 1.3. Many of the underlying molecular control techniques discussed in this thesis, and particularly those applied to CaH^+, were pioneered in the room-temperature apparatus.

Despite the impressive results from the room-temperature experiment, it faces several key limitations preventing realization of the platform's full promise. For one, the room-temperature TR interacting with the molecular ion stimulates rotational transitions on $O(100\text{ ms} - 1\text{ s})$ timescales, limiting the measurement fidelity and experimental data rate. For another, the experiment is designed for loading of CaH^+ (via a reaction of leaked H_2 with an already-trapped Ca^+ ion), without

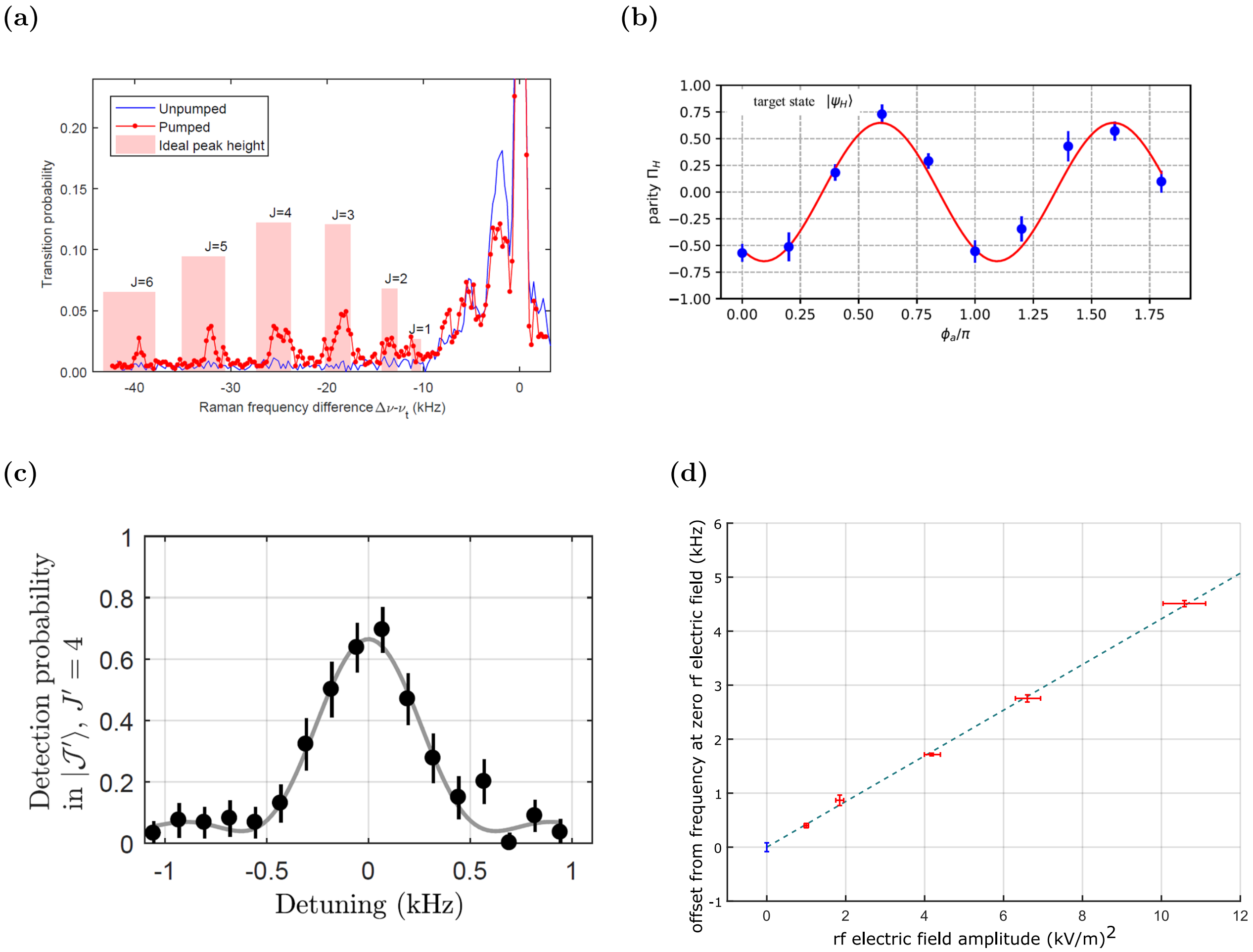

Figure 1.3: Select results from the first-generation, room-temperature NIST molecular ion apparatus. (a) A frequency scan of the detuning between Raman beams addressing a CaH^+ molecule. If a transition is driven between molecular sublevels, that information is transferred to a co-trapped Ca^+ ion via QLS and detected via Ca^+ fluorescence. (b) A parity fringe demonstrating entanglement between the trapped molecule and atom. (c) Detection of CaH^+ in rotational manifold $J = 4$ after preparation in $J = 2$ and application of a frequency comb as a Raman drive. (d) A measurement of the shift on a particular molecular transition due to an RF electric field from the trapping potential. The slope is used to infer the molecule's dipole moment.

consideration for loading other molecular species. Finally, the ion trap itself exhibits relatively high heating rates and micromotion that limit state manipulation fidelity and impose systematic errors. To make further progress and extend to new molecules, improvements are required.

1.3 Features of the NIST cryogenic molecular ion experiment

The second-generation apparatus described in this thesis addresses the limitations of the room-temperature apparatus. By using a liquid helium cryostat to cool the ion's surrounding environment, we observe an order-of-magnitude increase in rotational state lifetimes. We integrate a molecular beam machine and a dye laser for loading myriad molecular species via REMPI without introducing prohibitive amounts of background gas. We also use an ion trap with lower motional heating and micromotion for high-fidelity operation. An adaptive, non-destructive molecular state detection scheme allows for demonstration of SPAM fidelities of greater than 99.4% for a single molecular quantum state in CaH^+, the highest such SPAM fidelity reported for a molecule.

The apparatus and techniques used in this thesis address each aspect of quantum state control in ways that are not specific to a particular molecular species. A broad class of molecules can be included in a molecular beam and ionized via REMPI for loading. Any molecular ion whose charge-to-mass ratio is within a factor of three or so of that of the auxiliary ion can be co-trapped and will have sufficiently similar normal motional mode participation to allow for efficient sympathetic cooling and quantum-logic state transfer. The Raman beams, the only laser beams addressing the molecule's internal state, are far-detuned from any internal transition, meaning their absolute wavelength is not molecule-specific. Another remarkable feature of our scheme is that the measurement is non-destructive—it leaves the molecule in its pre-measurement state, which is required for many applications and convenient for most others. Altogether, the techniques presented here open the door to a new regime of molecular experiments that have not previously been feasible.

1.4 Thesis organization

This thesis will present the design, development, and operation of the cryogenic molecular ion experiment within the NIST Ion Storage Group. In Chapter 2 I discuss the design of the ion trapping apparatus, with a particular focus on the design decisions required to minimize the TR incident on the trapped ions. In Chapter 3 I describe the basic atomic and molecular ion operations required for high-fidelity QLS operation. In Chapter 4, I present high-fidelity state preparation, manipulation, and measurement results achieved on a CaH^+ ion. Chapter 5 discusses the development of a molecular beam machine that has been integrated into our ion trapping apparatus for loading of various molecular species, and finally in Chapter 6 I summarize and present future prospects for performing novel experiments on molecular ions.

Chapter 2

A cryogenic ion trapping apparatus

Much of my Ph.D. was concerned with designing and building a cryogenic ion trapping apparatus that minimizes TR incident upon the trapped ions and is amenable to precision measurement experiments with molecules. While many of these concepts have previously been realized individually and in various combinations, putting them all together in one experiment was a serious and novel technical challenge. In this chapter, I briefly discuss molecular energy level structure, motivate the requirement of minimizing TR for experiments with polar molecules, describe the design of the ion trap apparatus, and finally consider the system's thermal budget. Design and implementation of the molecular beam source for molecular ion loading will be covered in Chapter 5.

2.1 Molecular energy level structure

Molecular spectra exhibit energy splittings spanning many orders of magnitude across electronic, vibrational, rotational, hyperfine, and rotational Zeeman levels, as shown in Fig. 2.1.

- **Electronic** splittings follow similar patterns to those in atoms and typically fall within ultraviolet, visible, or near-infrared (IR) frequencies.
- **Vibrational** and rotational splittings are due to relative (lab-frame) motion of the molecules' constituent atoms and are therefore not found in atomic structure. Vibrational splittings are due to spring-like interactions between each of the molecules' constituent atoms; a (non)linear molecule made up of N atoms will have 3N-5(3N-6) vibrational modes. Vibrational splittings

in "small" molecules ($\lesssim$5 constituent atoms) often fall within IR frequencies, although larger molecules may have lower-frequency modes.

- **Rotational** splittings are due to collective rotation of the molecule's atoms about its principle axis or axes. While diatomic and other linear molecules have a single rotational axis and thus rotational mode, non-linear molecules can have up to three distinct rotational modes depending on symmetry. They often fall within the ~10-300 GHz (mm-wave) regime.
- **Hyperfine** splittings follow similar patterns to those in atoms, typically falling within microwave frequencies.
- **Rotational Zeeman** splittings arise from interaction of an external magnetic field with rotation. For our experimental parameters, they are of O(10 kHz).

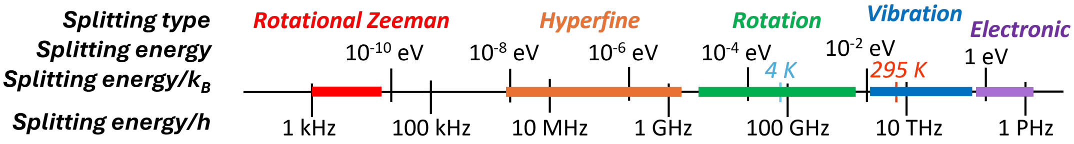

Figure 2.1: Typical energy scales of various types of energy splittings in molecules. Rotational and vibrational degrees of freedom are unique to molecules. For polar molecules, the temperature of ambient TR can be a primary factor determining rotational and vibrational state lifetimes. The scale of rotational Zeeman splittings assumes an applied magnetic field of O(0.1 mT), as is used in this work.

A single TR photon will move molecular population among levels that are connected by a dipole-allowed transition. For polar molecules,[1] some rotational and vibrational transitions are dipole allowed. Room-temperature TR has a characteristic energy scale $E = k_B T \approx 25$ meV, setting the scale of levels that are likely to be occupied.

To first order, the vibrational levels of a diatomic molecule correspond to those of a quantum harmonic oscillator. In this thesis, CaH^+ is the only molecule to be studied in detail. For CaH^+, the splitting between adjacent vibrational levels in the electronic ground state is $\Delta E_v \approx 180$ meV$\gg$25 meV,

---

[1] Only symmetric molecules—e.g. N_2, H_2, CO_2...—will have a net dipole moment of zero in the frame of the molecule, making them nonpolar. These special molecules can have nearly infinite theoretical rovibrational state lifetimes regardless of the TR environment.

so in a room-temperature TR environment the molecule will be in the ground vibrational (as well as electronic) state $> 99\%$ of the time. Furthermore, CaH$^+$ does not have relevant hyperfine structure, and we do not excite vibrational or electronic transitions. For these reasons, the remainder of this discussion will be confined to rotational manifold structure.

The rotational structure of a diatomic molecule can be estimated by the rigid rotor model. The Hamiltonian is:

$$H_{RR} = \frac{-\hbar^2}{2\mu}\nabla^2, \tag{2.1}$$

where μ is the reduced mass of the system and ∇^2 is the Laplacian operator. The corresponding Schrödinger equation $H_{RR}\Psi = E\Psi$ can be expressed in terms of spherical harmonics $Y_l^m(\theta, \phi)$:

$$H_{RR}Y_l^m(\theta, \phi) = \frac{\hbar^2}{2\mu r^2}J(J+1)Y_l^m(\theta, \phi), \tag{2.2}$$

where r is the bond length between the constituent atoms and rotational quantum number $J = 0, 1, 2\ldots$ The molecule's rotational constant B_R is defined as:

$$B_R \equiv \frac{\hbar}{4\pi c\mu r^2}, \tag{2.3}$$

where c is the speed of light. Without perturbation, the system has eigenstates at energies $E_J = hB_RJ(J+1)$ with $2J+1$ degeneracy. The degeneracy is lifted into Zeeman-type sublevels upon application of a magnetic field. More details of this sublevel structure for CaH$^+$ are provided in Section 3.3.3.

Smaller atoms typically form stronger, and thus shorter, bonds. Since $B_R \propto \frac{1}{r^2}$, monohydrides such as CaH$^+$ have some of the largest rotational constants, and thus level splittings, of any molecule. Even so, $B_{R,\mathrm{CaH}^+} = 142.5$ GHz, and the splitting $J = 0 \leftrightarrow 1$ is $2hB_{R,\mathrm{CaH}^+} \approx 1.2$ meV $\ll 25$ meV. In a room temperature TR environment, the molecular population will be spread over many rotational levels in equilibrium.

2.2 Cryogenic advantage

The cryogenic experiment presented here is a successor to a room-temperature molecular ion trapping experiment within the Ion Storage Group that has already demonstrated impressive control and precision measurement of a single trapped CaH^+ molecule [32, 44–47] with a co-trapped Ca^+ ion and QLS. However, the room-temperature TR environment, which is constantly driving rotational transitions $\Delta J = \pm 1$, poses a fundamental limitation on running such an experiment with a polar molecule.

Transition rates between rotational levels can be described by the Einstein coefficients, which dictate rates of photon emission and absorption. For a polar molecule interacting with a radiation field, the stimulated emission or absorption rate $B_{i\to f}$ between states i and f is:

$$B_{i\to f} = \frac{2\pi^2 d^2}{3\epsilon_0 h^2} u(\nu_{if}) cg_{if}^2, \tag{2.4}$$

where $u(\nu_{if})$ is the photon energy density at the transition frequency ν_{if}, d is the molecule's electric dipole moment, and cg_{if} is the Clebsch-Gordon coefficient between the initial and final state. Note that $cg_{if}^2 > 0$ only for transitions obeying $\Delta J = \pm 1$.

All surfaces will emit photons (TR) according to their temperature and emissivity. For an ideal blackbody at temperature T, the emitted photon energy density is given by Planck's law:

$$u(\nu, T) = \frac{8\pi h \nu^3}{c^3 (e^{h\nu/k_B T} - 1)}, \tag{2.5}$$

which is plotted for several temperatures and frequencies of interest in Fig. 2.2. Since u scales superlinearly with temperature, and commercial liquid-helium cryostats can reach base temperatures near the boiling point of helium at 4.2 K, cryogenic operation promises a reduction of stimulated transition rates by $\gtrsim \frac{295}{4.2} = 70$x in a cryogenic system relative to a room-temperature system.

For transitions obeying $\Delta J = -1$, the spontaneous emission rate $A_{i\to f}$ is:

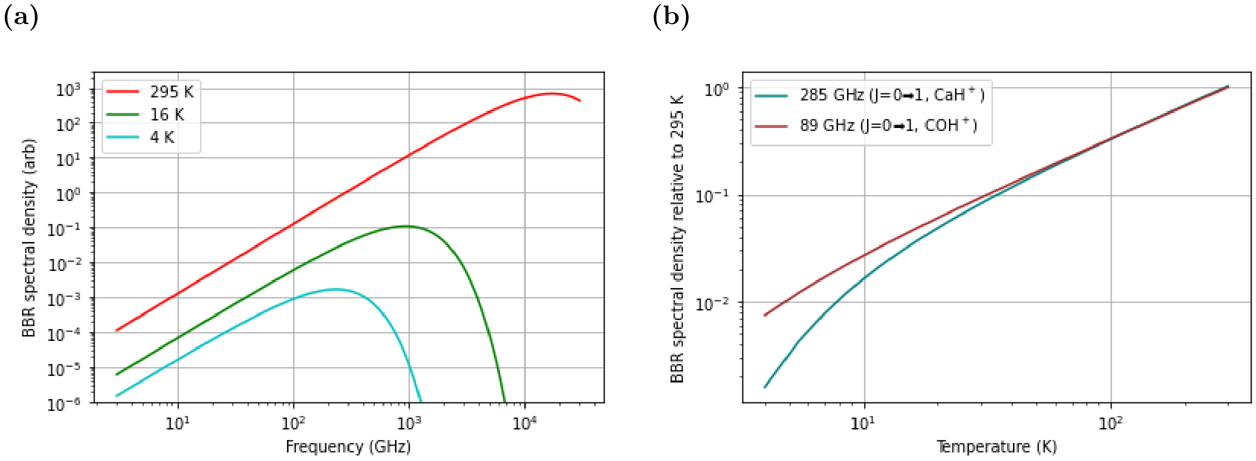

Figure 2.2: (a) Blackbody radiation (BBR) spectral density as a function of frequency at room temperature (295 K), measured experimental temperature (16 K), and liquid-helium temperature (4 K) vs frequency as stipulated by Eq. 2.5. (b) Fractional reduction in BBR spectral density vs temperature for the $J = 0 \leftrightarrow 1$ transition frequencies in CaH^{+} (285 GHz [46]) and COH^{+} (89 GHz [48]). The relationship is superlinear.

$$A_{i\to f} = \frac{16\pi^3 d^2}{3\epsilon_0 h c^3}\nu_{if}^3. \tag{2.6}$$

Because the spontaneous emission rate is independent of photon energy density, it does not depend on temperature and sets an upper limit for $\tau_{J>0}$.

A given rotational manifold typically has a multiplicity of rotational Zeeman sublevels. To calculate the average lifetime for a given initial sublevel $\tau_{Js(i)}$, the transition rates to all accessible final sublevels $Js(f)$ must be considered:

$$\tau_{Js(i)} = 1/(\sum_{f,\Delta J=\pm 1} B_{Js(i)\to Js(f)} + \sum_{f,\Delta J=-1} A_{Js(i)\to Js(f)}). \tag{2.7}$$

In the upper panel of Fig. 2.3, $\tau_{J\leq 3}$ (averaged across all $Js(i)$) are plotted for CaH^{+}. The lifetime of low-lying CaH^{+} rotational levels is O(1 second) at room temperature but is increased to ∼tens of seconds at cryogenic temperatures.

Besides limited state lifetimes, a related challenge imposed by TR is that in equilibrium, the molecule population is distributed in a statistical mixture of many rotational manifolds according to the Boltzmann distribution (whereby population in a particular level is proportional to $e^{-\frac{E_J}{k_B T}}$) and sublevel multiplicity. Given the characteristic energy scale $k_B T$, a diatomic molecule with rotational manifold energies near $hB_R J(J+1)$ will have a characteristic highest occupied J level given by:

$$J_{\mathrm{max\_occupied}} \sim \sqrt{\frac{k_B T}{hB_R}}. \tag{2.8}$$

The lower panel of Fig. 2.3 displays the expected population fraction of different rotational manifolds for CaH$^+$ as a function of temperature, accounting for a $2(2J+1)$ multiplicity. For this molecule at room temperature, the most-populated rotational manifolds have a population fraction of about 13%, while $J = 1$—the easiest manifold to work in due to its relatively long lifetime and low mulitplicity—has a population fraction of just 6.6%, a bane to experimental duty cycle. In contrast, at a temperature of 16 K (our measured experiment temperature), the $J = 1$ manifold has a population fraction of 47%.

Because of the considerations discussed in this section, one of the primary goals of the experimental system design is to reduce the TR experienced by the trapped ion as much as possible. This objective is implicit in many of the design decisions discussed throughout this chapter; it will be discussed explicitly in Section 2.7.

2.3 Ion Trap

At the heart of the experiment lies a linear radio frequency (RF) ion trap, which uses static and oscillating electric fields to spatially confine charged particles. In our experiment, the same ion can often be trapped for days at a time before being lost to, e.g., background gas collisions or accidental laser heating. Such highly stable confinement is of considerable utility for performing precision physics experiments.

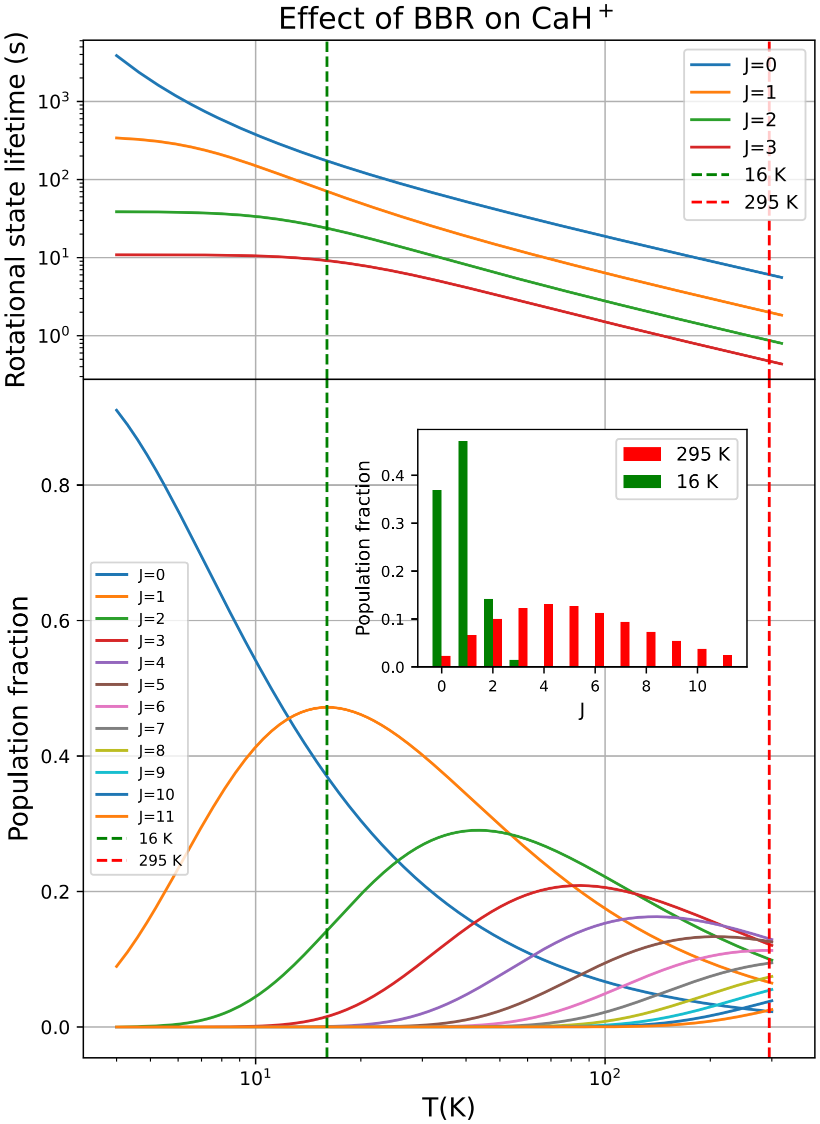

Figure 2.3: BBR effects on CaH$^+$. The upper panel shows the state lifetime τ_J of the lowest few rotational states of CaH$^+$ vs temperature. At high temperatures the increased photon density drives stimulated transitions that limit lifetimes, while at low temperatures, $\tau_{J>0}$ are limited by spontaneous emission and are thus insensitive to temperature. The lower panel shows equilibrium rotational level populations of CaH$^+$ vs temperature. The calculation considers the Boltzmann distribution and the multiplicity of states $2(2J+1)$. The inset compares the population fraction distribution at room temperature to that at the measured experiment temperature (16 K).

2.3.1 Ion trap background

A model linear RF trap [49–51] is depicted in Fig. 2.4. A DC potential provides confinement in one *axial* dimension (z) and an RF pseudopotential confines in the other 2 *radial* dimensions

(x, y). In particular, if pairs of opposing radial RF electrodes $RF_{\pm}$ have an applied voltage $V_{RF_{\pm}} = \pm(V_0 \cos(\Omega_{RF} t) + U_r)$[2] and opposing axial DC *endcap* electrodes have an applied voltage U_0, the total potential near the trap center ($x = y = z = 0$) is given by:

$$\Phi = (V_0 \cos(\Omega_{RF} t) + U_r)(1 + \frac{x^2 - y^2}{R^2}) + \frac{\kappa U_0}{Z_0^2}(z^2 - \frac{x^2 + y^2}{2}), \tag{2.9}$$

where R is the RF electrode-to-ion distance, Z_0 is the endcap-to-ion distance, and κ is a geometric factor of order 1. Note that the differential DC voltage $\pm U_r$ applied to the pairs of RF electrodes is not strictly necessary for trapping but serves to break radial motional mode degeneracy.

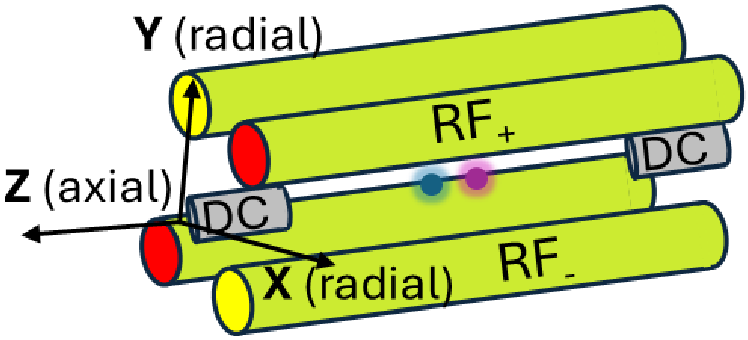

Figure 2.4: A model linear RF trap, which provides the basis for the trap used in this work. Trapped ions (blue and purple points) are confined in a line (in the z dimension) by RF and DC electrodes.

A single ion's radial motion is described by the Mathieu equations [52], which take the form [53–55]:

$$\frac{d^2 i}{dt^2} + [a_i + 2q_i \cos(\Omega_{RF} t)]\frac{\Omega_{RF}^2}{4} i = 0, i \in \{x, y\}, \tag{2.10}$$

with the parameterization

$$a_i \equiv \frac{4\alpha}{\Omega_{RF}^2}(\kappa U_0 \mp \frac{2U_r}{R^2}), q_i \equiv \pm\frac{4\alpha V_0}{\Omega_{RF}^2 R^2}, i \in \{x, y\},^{3} \tag{2.11}$$

---

[2] This notation differs with much of the literature by a factor of 2, since in our trap voltage is applied symmetrically to the two pairs of RF electrodes, rather than one pair being grounded.

where $\alpha \equiv \frac{q}{m}$ is the charge-to-mass ratio of the trapped ion. Our trap operates in the so-called first region of stability, where $a_i < |q_i| \ll 1$, $i \in \{x, y\}$. Then, Eq. 2.10 can be solved to first order in a_i and q_i. The resulting approximate solutions are harmonic oscillators.

The ion's axial equation of motion also corresponds to a harmonic oscillator:

$$\frac{d^2z}{dt^2} + \frac{2\alpha\kappa U_0}{Z_0^2} z = 0. \tag{2.12}$$

Thus, a single ion's *secular* motion is described by 3 harmonic (secular) frequencies given by:

$$\omega_i = \sqrt{\frac{2\alpha^2 V_0^2}{\Omega_{RF}^2 R^4} - \frac{\kappa\alpha U_0}{Z_0^2} \pm \frac{2\alpha U_r}{R^2}}, i \in \{x, y\}, \tag{2.13}$$

$$\omega_z = \frac{\sqrt{2\alpha\kappa U_0}}{Z_0}. \tag{2.14}$$

If multiple ions are confined in a single trapping potential and cooled such that their mean kinetic energy is small compared to their Coulomb interaction, the ions will form stable arrangements known as Coulomb crystals. A crystal of N ions will have 3N normal modes of motion whose frequencies can be calculated numerically and fine-tuned experimentally. The description of their motion can be quantized by expressing position and momentum variables in terms of harmonic oscillator ladder operators [56]. In this thesis, I will be primarily concerned with the 6 modes of a two-ion crystal. Then, the normal modes are well-described by one in-phase (IP) mode (where the ions simultaneously move in the same direction) and one out-of-phase (OOP) mode (where the ions move in opposite directions) for each dimension.

When the motion in a particular mode is cooled to near the motional ground state, it is often convenient to parametrize in terms of $\bar{n}$, the average number of motional quanta that the ions would possess if measured over many trials. While a room-temperature particle has $\bar{n} \sim \frac{k_B T}{\hbar\omega_i} \approx 10^6$ (for ω_i of O(MHz), as is the case in this work), our secular modes will often be laser-cooled to $\bar{n} < 1$ during

---

[3] Here and in Eq. 2.13, upper (lower) signs correspond to $x(y)$.

experiments. See Section 3.2 for details of laser cooling methods.

If a static electric field displaces the ion from the radial center ($x = y = 0$) of the RF potential, the RF electric field at the ion is non-vanishing and induces a second type of motion, known as *micromotion*, at frequency Ω_{RF}. In practice, some micromotion also exists in the axial direction due to the finite size of trap electrodes and imperfect trap construction. DC voltages on suitable trap electrodes are used to move the ion in all three dimensions to minimize the observed micromotion. More discussion on measuring and minimizing micromotion is provided in Section 3.2.4.

2.3.2 Our ion trap

Our experiment deploys a linear RF trap design known as the wheel trap, in which the RF ($RF_\pm$) and radial micromotion-compensation ($\mathrm{comp}_{H(V)}$) electrodes are constructed monolithically by depositing gold on a 500 μm-thick laser-machined diamond wafer (see Fig. 2.5a). This design has been optimized to trap small numbers of ions with low heating rates[4] and micromotion for precision measurement applications [7, 57]; the high thermal conductivity of diamond also helps to dissipate thermal load. Separate, titanium endcaps provide the axial confinement. The assembled trap structure is shown in Fig. 2.5b.

To provide the RF potential, about 4 watts of RF power are sent into a meandering-line resonator printed on a printed circuit board (PCB) (see Fig. 2.5c and Ref. [55]). The RF input is split by a balun to deliver equal and opposite RF amplitude to the $RF_\pm$ electrodes. A tunable capacitor on the resonator board allows for matching of the source and load impedances. Without a load, our resonator resonance frequency is $2\pi\times80$ MHz; when connected in situ, the resonance frequency drops to $2\pi\times67.6$ MHz due to the capacitance of the vacuum feedthrough, the in-vacuum cryogenic shield feedthroughs, and the trap itself. Similarly, we measure a quality factor of 170 for the unloaded resonator but 120 in situ due to lossy couplings.

Each endcap and compensation electrode is powered by a digital-to-analog converter (DAC)-

---

[4] Heating rate $\frac{d\bar{n}}{dt}$ is the rate of increase of motional quanta over time for a trapped ion with no laser light applied; it is typically attributed to surface effects on trap electrodes.

controlled, high-voltage amplifier that can output up to ±500 V. Each line passes through two out-of-vacuum, low-pass filtering stages; RF bias tees allow for the introduction of RF voltages on select trap DC electrodes for intentional excitation of secular motion. A fifth amplifier output provides a common DC bias to the RF electrodes, allowing for an endcap-to-RF electrode DC voltage differential of up to 1 kV. Another DAC output and a voltage divider circuit provide control of U_r. A diagram of the RF and DC signal paths is included in Appendix B.

Table 2.1: Geometrical and typical voltage parameters for our wheel trap. Single Ca^+ secular frequencies $(\omega_x, \omega_y, \omega_z) \approx 2\pi \times (3.8, 4.0, 2.5)$ MHz.

R	Z_0	κ	Ω_{RF}	V_0	U_0[5]	U_r
0.25 mm	3.9 mm	4.4	$2\pi\times67.6$ MHz	425 V	180 V	1 V

2.4 Vacuum

Maintaining ultra-high vacuum (UHV, $\lesssim 10^{-7}$ Pa) at the ion trap is critical for operating a precision QLS experiment; collisions with background gas can change the ions' order, heat the ion crystal, or cause ion loss from the trap. All connections to the vacuum chamber are made with CF connections and stainless steel vacuum components. The system was baked at 80° C for several days to reduce outgassing. When the experiment is cryogenically cooled, background gas pumping near the ion occurs via cryopumping (particles adsorbing onto cold surfaces). To enhance this effect, a small amount of activated charcoal, which has high adsorption capacity, is included inside the cold stage. In the room temperature compartment, a 55 L/s ion pump and a titanium sublimation pump (TSP) provide additional pumping and mitigate pressure spikes when the system is warming up. A computer-aided design (CAD) drawing of the system is provided in Fig. 2.6.

An ion gauge measures the vacuum pressure at room temperature to be $\sim 10^{-8}$ Pa during normal operation. Conductance from the ion to room temperature is poor, so this is not necessarily

---

[5] The axial micromotion minimum is found empirically to be displaced by 0.18 mm from the geometrical trap center. To access this location, we require a highly imbalanced endcap configuration, with the two endcap voltages $(U_1, U_2) \approx (700, 50)$ V. Note that $U_1 U_2 \approx U_0^2$.

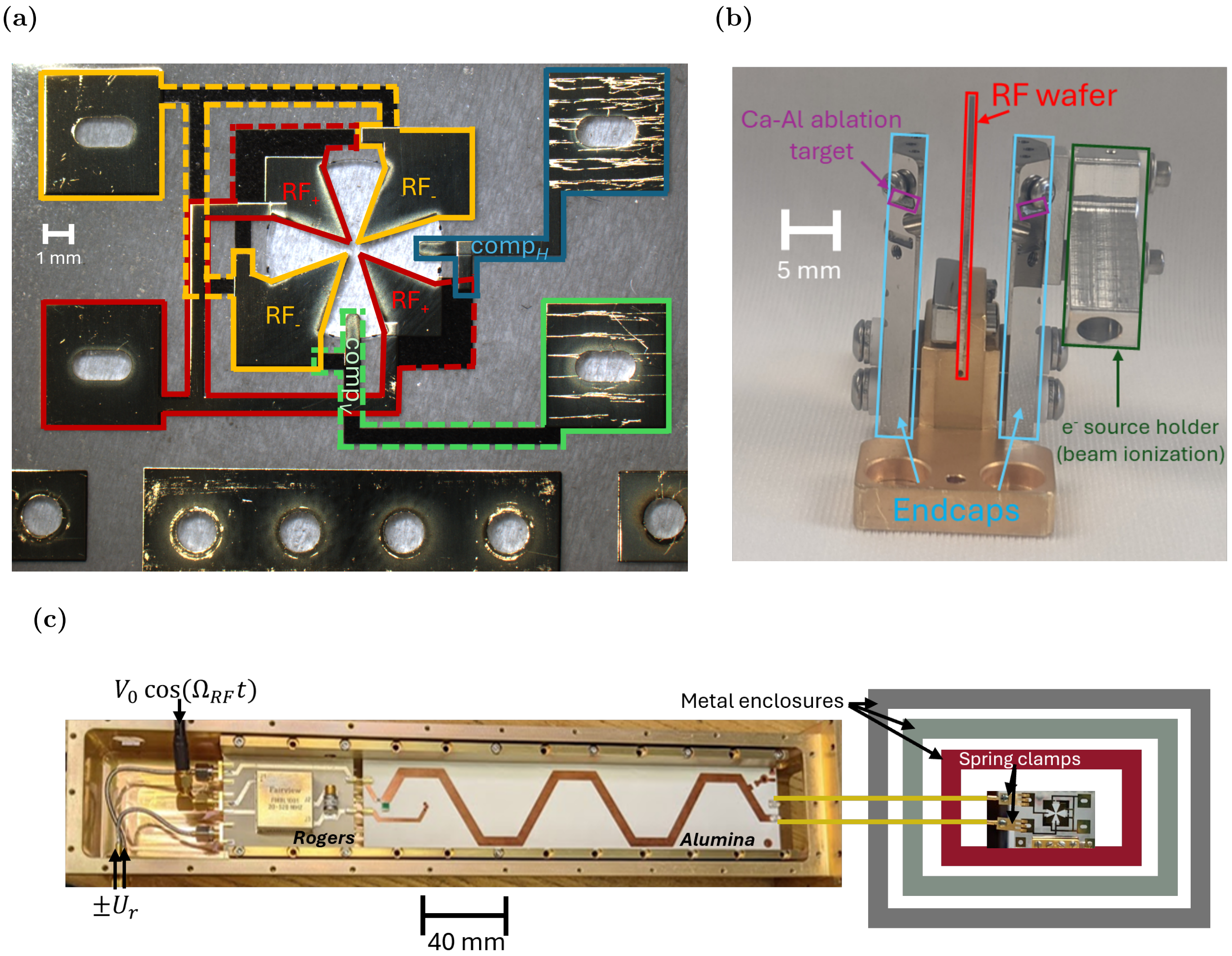

Figure 2.5: Ion trap images. **(a) Front view of the diamond trap wafer taken under a microscope.** RF voltages applied to the $RF_\pm$ electrodes provide radial confinement of the ion, while comp$_{H(V)}$ electrodes are used for radial micromotion minimization. Electrodes are printed on one or both sides of the wafer; dashed outlines indicate an electrode printed only on the back. The traces are optimized for balanced capacitance for minimal excess micromotion. **(b) Side view of the mounted trap**, including RF wafer and endcaps. The endcaps provide axial confinement of the ion. Ablation occurs on the front (not visible) face of the targets, which have lines of sight to the trapping region. A holder for an electron source as a potential ionization method for molecule loading is attached to one of the endcaps. **(c) Picture of RF meander-line resonator board and illustration of connection to the trap chip.** A balun on the Rogers PCB section ensures an equal and opposite RF signal is applied to each RF line (one of which, printed on the backside of the PCBs, is not visible); the differential DC voltage $\pm U_r$ between the lines serves to break radial mode degeneracy. The coupling loop of the resonator is on the alumina PCB section; see Ref. [55] for more details. RF lines must pass through layers of metal enclosures to reach the trap chip. Lossy couplings at these feedthroughs limit the Q factor achieved by the loaded resonator and are a significant contribution to the system's thermal load. Custom-made spring clamps connect the RF lines to the $RF_\pm$ electrodes.

an accurate measurement of the pressure experienced by the ion. Nevertheless, typical observed two-ion reorder rates of one reorder per several minutes are consistent with this value [58] and are sufficiently low for experimental operation.

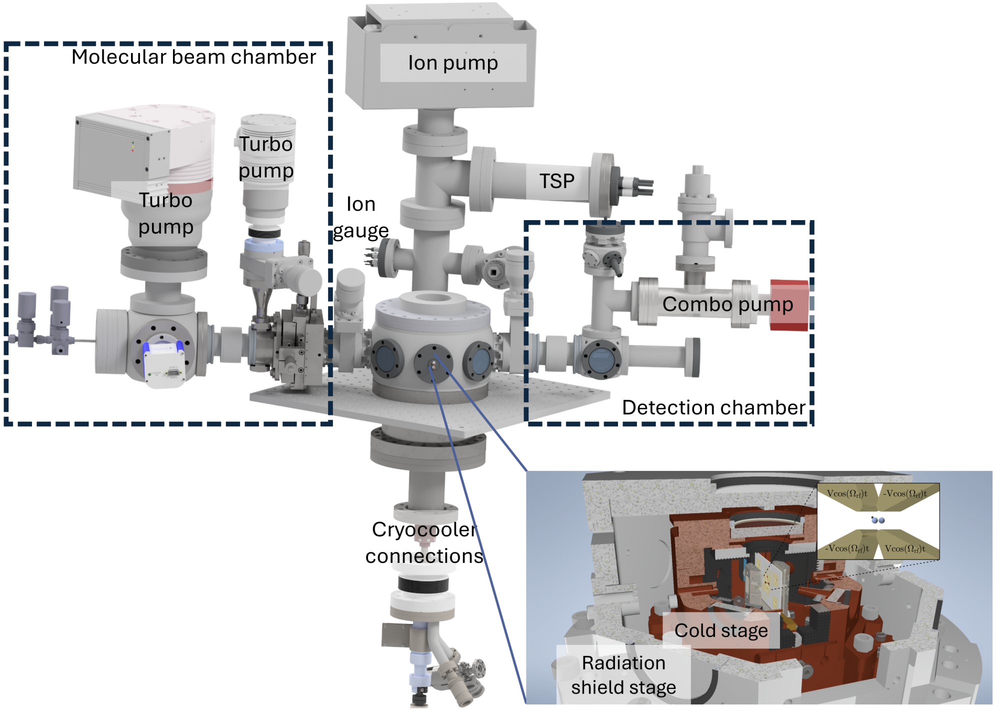

Figure 2.6: CAD model of the vacuum chamber. In the room temperature compartment, vacuum pumping occurs via an ion pump and a TSP, and the vacuum level is measured by an ion gauge. Within the cold stage, pumping is largely due to cryopumping, and the pressure can only be observed via 2-ion reorder events. The molecular beam chamber is pumped with turbo pumps and is separated from the ion trap chamber by a 3-mm aperture, while the detection chamber is pumped by an ion-getter combo pump and is closed off from the ion trap chamber via a gate valve under normal operating conditions; these auxiliary chambers are discussed further in Chapter 5. The inset shows a cutaway view of the nested cryogenic stages and the ion trap sitting at the center.

2.5 Cryocooling System

Cryogenic cooling power is provided via a Stinger cryostat from ColdEdge. Two compressors circulate helium gas within a closed-cycle Gifford McMahon liquid helium cryostat system designed to have low vibrations at the cold tip. The cold tip is mounted within a CF flange, and a 2 meter-long flexible hose delivers liquid helium from the cryocooler to the cold tip. More details of the Stinger system, including a schematic and select operating procedures, are described in Appendix A.

One consideration of using a closed-cycle cryogenic system is the vibrations due to the compressors. Vibrations can cause Doppler shifts of the laser beams as seen by the ion, limiting the precision of ion spectroscopy. The Stinger is designed to decouple the compressor vibrations from the experimental apparatus—it is quoted as having < 20 nm vibrations at the cold tip. We added another layer of vibration isolation by making all connections between the Stinger system and the ion trap flexible. Gold-coated copper braids connect the cold tip and radiation shield to the experimental apparatus, while a bellows provides the vacuum connection (the flexible connections also compensate for imperfect mechanical tolerances). The Stinger side of the bellows is secured to the base of the optical table, which is in turn decoupled from the tabletop via active vibration isolation (AVI) platforms. A diagram of the Stinger's thermal and mechanical connections to the experimental apparatus is provided in Fig. 2.7. For additional acoustic isolation, the cryocoolers and compressors are located behind a wall on an isolated floor from the lab.

Within the Stinger, cryogenic helium flows to the cold tip to reach temperatures as low as 4 K. A radiation shield reduces the blackbody thermal load on the cold tip and is cooled by the gas returning from the cold tip to as cold as 15 K. Additional thermal load imparted by the apparatus can increase these base temperatures. An important performance metric of the Stinger is the cooling power curve, which plots the achieved temperature as a function of heat load applied. Before connecting the Stinger to the apparatus, we directly measured this curve for both the cold tip and the radiation shield via a heater and temperature sensor attached directly to the end of the respective component. The test results can be seen in Fig. 2.8. Note that these results are not necessarily consistent across different Stinger systems.

Another factor determining the base temperature achieved at the ion is the temperature gradient between the Stinger and the experiment. We expect this to be dominated by the thermal resistance across the copper braids, although it could also be limited by the contact resistance of the physical connections. The resistance of the copper braids was estimated by the manufacturer as

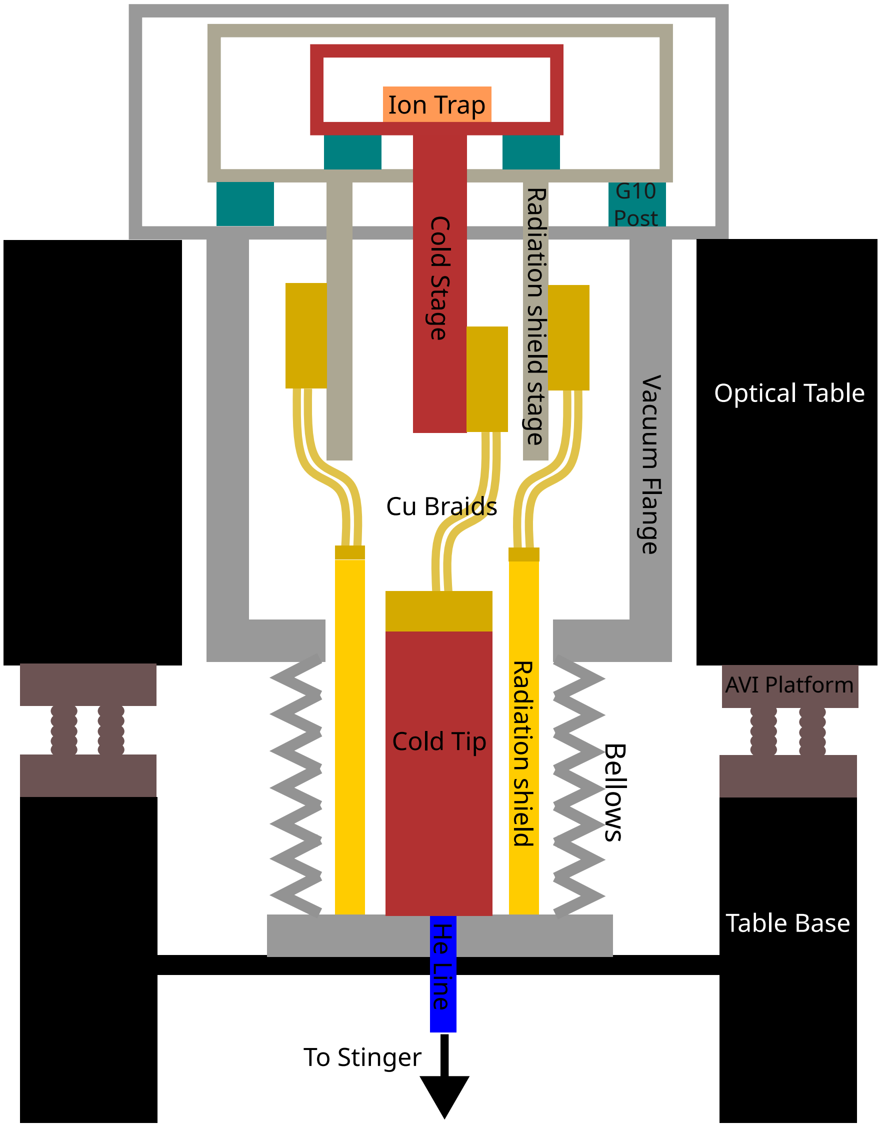

Figure 2.7: Illustrative cross-section of the apparatus, including thermal and mechanical connections to the Stinger cryocooling system. The experiment chamber is connected non-rigidly to the cryostat from below through a circular hole in the optical table; the cold stage containing the ion trap is thus cooled to cryogenic temperatures while experiencing minimal vibrations.

3.3 K/W for the cold tip braid and a cumulative 0.4 K/W for the radiation shield braids. In an attempt to reduce these resistances, we annealed the braids under vacuum at 300 C for 2 hours; the annealing temperature, and thus likely the performance improvement, was limited by the fact that the annealing occurred after the braid's gold coating had been applied.

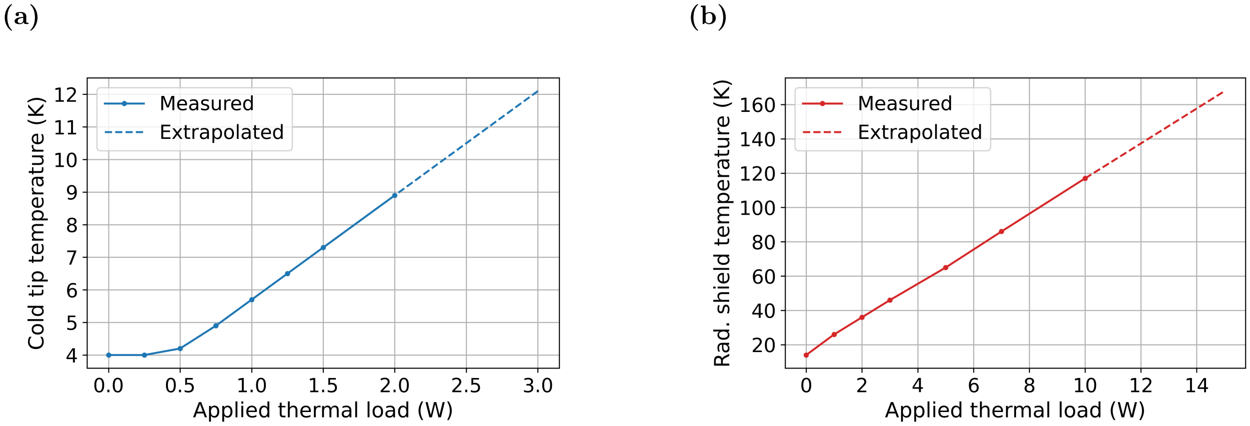

Figure 2.8: Measured cooling power at each stage of the cryostat. The thermal load is applied via a resistive heater directly to the stage under measurement, and the temperature is measured via a resistance temperature detector (RTD). (a) Cold tip cooling power. Extrapolation is a linear fit to last 4 measured points. (b) Radiation shield cooling power. Extrapolation is a linear fit to all points.

2.6 In-vacuum system

Much of the in-vacuum design is centered around minimizing the TR incident upon the ion while still providing necessary electrical connections, minimizing vibrations, maintaining UHV, and allowing for optical access. In this section, I will describe the various in-vacuum components, and in the next section I will quantify the thermal effects on the apparatus.

2.6.1 Cryogenic stages

The ion trap sits inside of the gold-coated copper cold stage, which in turn sits inside the aluminum radiation shield stage, which is housed inside the stainless steel vacuum chamber. The four mounting posts for each stage are G10 tubes, affixed by metal screws.[6] G10 is a composite material—made by stacking and epoxying sheets of fiberglass—which has low thermal conductivity while providing relatively high structural stiffness. To verify the mechanical stability of our mounting design, we used the normal mode analysis tool in Autodesk Inventor. Ultimately, the final design was

---

[6] Screw connections that are cooled to cryogenic temperatures can loosen if the spacer material contracts more than the screw material during cooldown. All such connections in our apparatus are engineered so that they tighten, rather than loosen, upon cooling.

chosen as a tradeoff between maximizing mechanical stability and minimizing thermal conductance (see Section 2.7.1). It was found, for example, that G10 imparts a lower thermal load for the same structural stability compared to stainless steel given practical constraints in our apparatus, and that thin-walled, large-diameter tubes are the optimal post form factor. For our final design, the lowest frequency modes as found by computational analysis are the pendulum modes (one of which is pictured in Fig. 2.9d) at 536 Hz.

2.6.2 Wiring

Six high-voltage wires lead from the exterior of the chamber to the ion trap. The high-voltage vacuum feedthrough pins are made of molybdenum. These are attached in vacuum to stainless steel pins with a 1-2 μm gold coating. Having a conductive outer coating thicker than the characteristic skin depth of the $2\pi\times67.6$ MHz trap frequency allows for low-loss transmission of the RF signal, while steel is a good thermal insulator. The wires are heat sunk at each cryogenic stage via sapphire clamp feedthroughs; sapphire is chosen because of its high thermal conductivity and low dielectric loss tangent, minimizing dissipative heating of the stages. An indium layer is used between the sapphire and the pins to ensure good thermal contact. Custom, gold-coated spring clamps are used to interface the wires to the trap chip.

Seventeen additional low-voltage wires also are passed into the cryogenic stages. They are primarily 34 AWG BeCu wires used for four-wire temperature sensor measurements, with some additional wires leading to an electron source and a heater on the cold stage. All of the wires use interconnects on custom alumina PCBs for modularity and heat sinking.

2.6.3 Windows and apertures

Four sets of windows, 1/2" diameter at the cold stage and 1" diameter at the radiation shield stage, allow for laser access along 4 orthogonal, horizontal ports; a fifth set, located vertically above the ion (1" and 1.5" diameter, respectively), allows for vertical laser access and imaging. Windows and apertures are possible leakage channels for TR from the outer, hotter surfaces. We primarily use

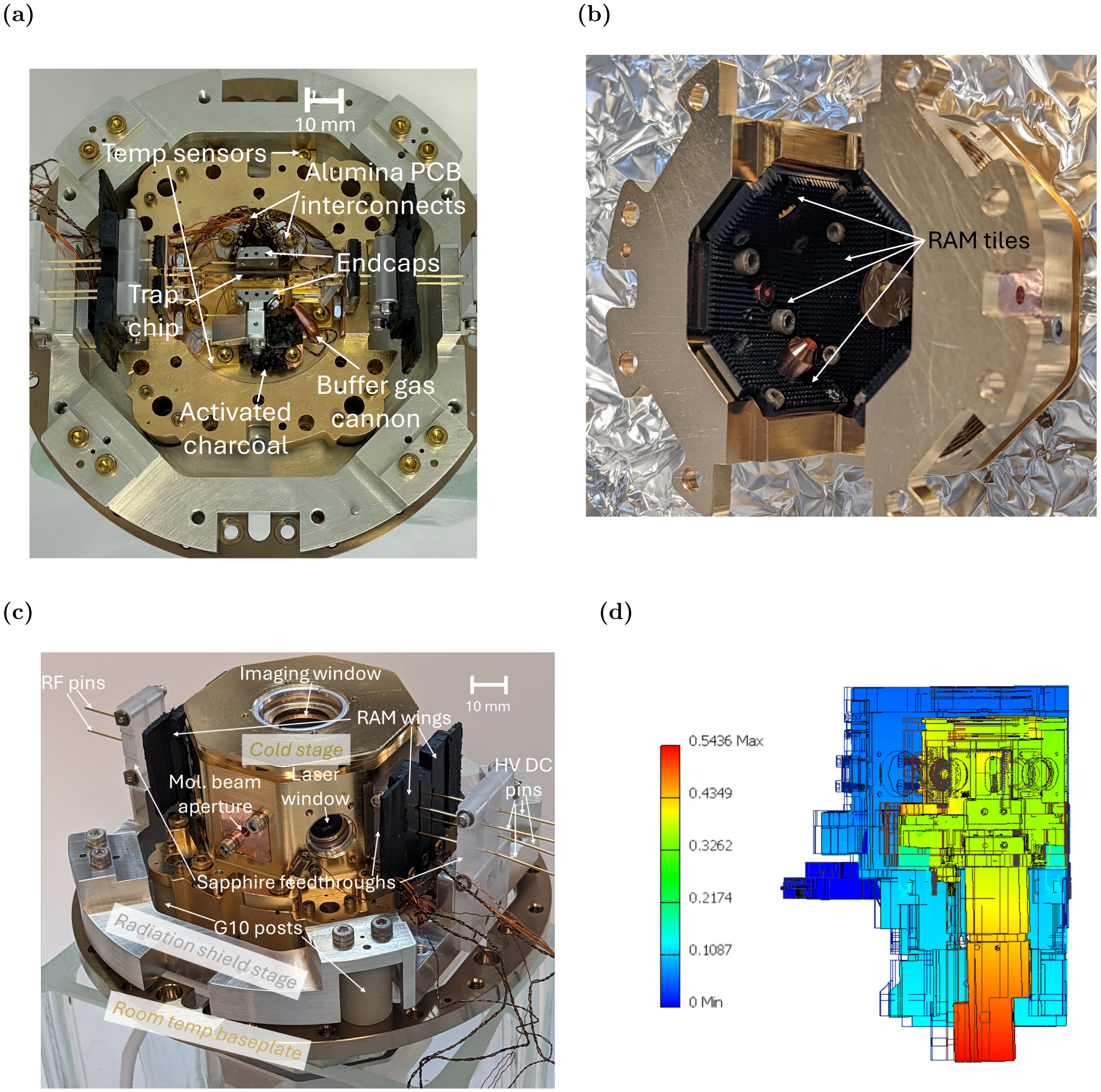

Figure 2.9: In-vacuum design. **(a) Partial vacuum assembly.** The "lids" of both the cold stage and radiation shield stage are removed. The buffer gas cannon (not mentioned elsewhere) allows for the possible introduction of buffer gas for collisional cooling. **(b) RAM tiles lining the inner surface of the cold stage** to absorb any leaked TR from high-temperature surfaces. Copper apertures can be seen jutting into the interior the the cold stage; this design serves to minimize possible TR leakage through apertures and windows. **(c) Vacuum assembly with cold stage lid in place. (d) Modal analysis in Autodesk Inventor.** The lowest-frequency (pendulum) mode is depicted; the color scale indicates displacement in arbitrary units. The system is considered fixed at the room-temperature stage, which is screwed directly to the optical table.

BK7 windows on the cold stage, because these are more opaque to TR in the frequency range relevant for molecular rovibrational transitions [59]. However, we leave one cold stage (horizontal port) window as fused silica for possible UV or microwave optical access; on this window, an additional copper cone is included within the cold stage for maximal TR rejection, as can be seen in Fig. 2.9b. All radiation shield stage windows and room-temperature viewports are fused silica with a custom anti-reflection coating.

Our molecular beam requires entrance and exit apertures in each stage (1 mm diameter in the cold stage), which afford some small but direct line of sight from the ion to room temperature surfaces. Finally, a gap is left between the sapphire feedthroughs and the main body of the cold stage to allow for some vacuum conductance between the interior of the stages and the vacuum pumps; direct line of sight from hotter surfaces to the inside of the cold stage is minimal.

2.7 Thermal load

The balance between the total thermal load on each stage and the respective stage's cooling power determines each stage's operating temperature. The cold stage temperature is a major factor in determining the TR experienced by the ion, while the radiation shield stage temperature directly affects the cold stage thermal load in several ways. Sources of heat can be conductive (through mounting structures or wires), dissipative (via trap RF dissipation), or radiative (from TR) [60]. In this section, I discuss the contributions from these sources to the thermal load.

Some of these heating mechanisms depend on temperature differentials between stages; thus, a full differential-equation solver is used to calculate the temperatures of the two stages as part of one system of equations. When quoting the heat load contribution in the following, I will assume the calculated operating temperatures, which are 8.6 K at the cold stage and 86.1 K at the radiation shield stage. In Section 2.7.4 I will address discrepancies between calculated and measured values.

2.7.1 Conductive heating

When two bodies at different temperatures are physically connected, heat flows from the hotter to the colder body. The amount of heat flow ($\frac{dQ}{dt}$) can be calculated according to the thermal conductivity integral:

$$\frac{dQ_{\text{conductive}}}{dt} = \frac{A}{L} \int_{T_c}^{T_h} K(T)\, dT, \tag{2.15}$$

where L and A are the length and cross-sectional area of the connection, respectively, and K(T) is the temperature-dependent thermal conductivity of the connection material. The primary contribution to the thermal load of both stages is due to the G10 mounting posts. The geometry of the mounting posts and final calculated thermal loads are shown in Table 2.2.

Table 2.2: Mounting post geometry and calculated contribution to thermal load

	OD (mm)	ID (mm)	L (mm)	$\frac{dQ_{\text{posts}}}{dt}$ (W)
Rad. shield stage	15.5	6.4	12.7	3.64
Cold stage	14.7	8.1	22.2	0.31

A secondary source of conductive heating is wiring. Of this, most comes from the 2 RF connections and 4 DC connections to the trap, consisting of 0.71 mm-diameter stainless steel pins with a 2 and 1 μm-thick gold coating, respectively. Each has a 73 mm length from room temperature to the radiation shield stage sapphire feedthrough (i.e., heat sink), and another 19 mm to the cold stage sapphire feedthrough. In total, they contribute 160 mW to the radiation shield stage thermal load and 110 mW to the cold stage. The contribution from the smaller DC wires is < 10 mW at each stage.

2.7.2 Dissipative heating

We send about 4 watts into the trap chip during normal operation and measure a loaded resonator Q of 120, meaning that there is about $4\sqrt{120} = 44$ watts of RF power delivered to the trap chip. Any resistance within the trap chip electrodes or capacitive coupling to lossy components will lead to ohmic heat dissipation. An RF simulation was performed including geometric capacitances and inductances at all feedthrough stages and losses commensurate with the observed Q values of the loaded and unloaded resonator. From the simulation, it was found that ∼700 mW of heat are dissipated somewhere within the vacuum apparatus, much of this likely due to capacitive coupling to lossy components. We conservatively assign $2/3 \pm 1/3$ of this loss to the cold stage and the remainder to the radiation shield stage.

2.7.3 Radiative heating

Every surface emits and absorbs photons according to its temperature and emissivity. When a colder surface (at temperature T_c) has line-of-sight to a warmer surface (at T_h), the total heat flow from the warmer to the colder surface will be:

$$\frac{dQ_{\text{radiative}}}{dt} = \sigma_{sb} A_c \frac{\epsilon_h \epsilon_c}{\epsilon_h + \epsilon_c - \epsilon_h \epsilon_c} (T_h^4 - T_c^4), \tag{2.16}$$

where σ_{sb} is the Stefann-Boltzmann constant, A_c is the area of the colder surface, and $\epsilon_h(\epsilon_c)$ are the surface emissivities. The T^4 dependence of Eq. 2.16 underscores the importance of using a cold radiation shield. Reducing the emissivities of the relevant surfaces (i.e., making them shiny) is also very helpful. Besides the radiative heat load from the radiation shield stage, another contribution to the cold stage radiative thermal load is residual radiative heating from room temperature that makes it through windows and apertures in the radiation shield stage; however, conservatively estimating 10% TR power transmission through the radiation shield stage windows, this contribution turns out to be < 10 mW.The total calculated radiative thermal load on each stage is indicated in Table 2.3.

Note the large uncertainty in this calculation, which primarily stems from the emissivities being roughly estimated from literature values. To make matters worse, the effective emissivities depend not only on the metal surfaces, but also other exposed surfaces such as windows, mounting posts, feedthroughs, etc. We do our best to use conservative, but reasonable, values for the effective

Table 2.3: Calculated radiative thermal load based on stage geometries, emissivities, and temperatures.

	A (m^2)	ϵ_h	ϵ_c	T_h (K)	T_c (K)	$\frac{dQ_{\text{radiative}}}{dt}$ (W)
Rad. shield stage	0.080	0.1	0.3	295	86.1	2.76 (1.10)
Cold stage	0.031	0.3	0.1	86.1	8.6	0.01(1)

emissivities.

In addition to being a leading contributor to thermal load, radiative processes are also the source of photons that drive undesired stimulated rotational state changes in the molecule. If the cold stage were perfectly isolated from the external environment, the photon density experienced by the trapped ion would simply be determined by the temperature of the cold stage. However, TR can leak to the ion from the outer stages through windows and apertures. If the inner surface of the cold stage is highly reflective, the leaked radiation could undergo many reflections before possibly interacting with the molecule; in the worst case, the photon density at the ion could equilibrate to that of the leaked radiation.

In order to dampen the internal reflection, we added radar-absorbing material (RAM) to the inner surface of the cold stage as shown in Fig. 2.9b. The RAM is polypropylene based, injected with metal particulates to maximize dissipation, and shaped into pyramids of ~1 mm height. It boasts near-unity absorption at frequencies $\gtrsim$100 GHz [61]. We also cover the cold stage sapphire feedthroughs—which are semi-transparent to mm-wave frequencies—with RAM wings, visible in Fig. 2.9c.

Following discussion in Ref. [62], we estimate that the effective temperature $T_{\text{eff}}(\nu)$ at the ion is an average of aperture areas and RAM tile coverage area, weighted by the respective temperatures. In particular, summed over each aperture (ap):

$$T_{\text{eff}}(\nu) \approx \frac{\sum_{\text{ap}} T_{\text{ap}} A'_{\text{ap}}(\nu) + T_{\text{cold}} A_{\text{RAM}}}{\sum_{\text{ap}} A'_{\text{ap}}(\nu) + A_{\text{RAM}}}, \tag{2.17}$$

where for a given aperture, T_{ap} is the temperature of the incident BBR and A'_{ap} is the effective area—the physical area scaled by transmission of incident BBR, which will be frequency-dependent for a window or for a clear aperture with diameter comparable to the radiation wavelength. T_{cold} is the temperature of the cold stage and A_{RAM} is the total area of RAM tiles within the cold stage.

Equation 2.17 is an idealization. For example, it does not account for the fact that radiation leaking through an aperture with direct line of sight to the ion will have a greater impact on effective ion temperature than one with line of sight only to RAM tiles. Nevertheless, it can guide our design decisions (e.g., make $A_{\mathrm{RAM}} \gg \sum A'_{\mathrm{ap}}$), suggests a frequency dependence in T_{eff}, and can be used to place reasonable bounds on the expected final $T_{\mathrm{eff}}(\nu)$. For our final construction, $A_{\mathrm{RAM}} \approx 24.7$ cm^2 and $\sum A'_{\mathrm{ap}} \lesssim 1.7$ cm^2; given the calculated stage temperatures, I estimate $T_{\mathrm{eff}} \lesssim 20$ K, with some inverse dependence on ν due to the absorption spectrum of BK7 [59]. For a discussion of observed ion effective temperature, see Section 4.2.3.

2.7.4 System thermal performance: calculated and observed

In Table 2.4, I summarize the calculated thermal load contribution from each component at each stage. Thermal load on the radiation shield stage is dominated by mounting posts and BBR, while on the cold stage it is dominated by mounting posts and trap RF dissipation.

Table 2.4: Calculated thermal load at each cryogenic stage. The largest uncertainty contributions come from imperfect characterization of trap RF dissipation location and the average emissivities of the stages.

	Cold stage thermal load (W)	Rad. shield stage thermal load (W)
Mounting posts (conductive)	0.34(5)	3.56(8)
Wiring (conductive)	0.12(1)	0.16(1)
BBR (radiative)	0.01(1)	2.76(1.10)
Trap RF (dissipative)	0.47(23)	0.23(23)
Total	0.94(31)	6.71(1.28)

Considering the thermal load contributions, cooling power curves, and copper braid conductivities, I performed a numerical calculation of the expected steady-state temperatures at various positions within the system. We also experimentally measure many of these values using diode or RTD temperature sensors. The results are compared in Table 2.5.

Table 2.5: Temperatures at each cryogenic stage. Uncertainties in calculated values correspond to uncertainties in thermal load as indicated in Table 2.4. Uncertainties in the measured values indicate the range over which a sensor may read over weeks of operation; fluctuations are likely due to changes of helium flow rate in the Stinger system.

	Calculated operating [RF off] temp (K)	Measured operating [RF off] temp (K)
Cold stage	8.6(2.0) [6.1(4)]	16.0(6) [11.5(5)]
Cold tip	5.4(1.0) [4.0(0)]	11.4(5) [7.3(4)]
Radiation shield stage	86.1(8.4) [84.0(10.9)]	189(6) [186(6)]
Radiation shield	83.6(7.8) [81.6(10.4)]	NO SENSOR

Examining Table 2.5, it is clear that the measured temperatures do not align with the calculated temperatures. The cause of this discrepancy is not verified; however, there are several pieces of evidence suggesting there is a failed thermal connection involving the radiation shield braids, perhaps occurring during transport (see discussion in Section 4.4.) Unfortunately, we have no sensor on the radiation shield to verify. If the thermal gradient across the radiation shield braids in calculation is tuned such that the calculated and measured radiation shield stage temperatures match, the subsequently calculated cold stage and cold tip temperatures agree within error bars with measured values. The thermal loads calculated after this update are displayed in Table 2.6. Note that the thermal load on the cold stage is ∼2x larger due to the increased radiation shield stage temperature, explaining the higher-than-expected measured temperature of 16 K under operating conditions. We can also use the observed temperatures to put an updated bound on the expected effective temperature: $T_{\text{eff}} \lesssim 30$ K.

Prospective system upgrades may address the thermal connection issue and lower the cold stage temperature. However, all experiments presented in this thesis are performed with the measured operating temperatures indicated in Table 2.5.

Table 2.6: Thermal loads back-calculated from observed temperatures. Specifically, the radiation shield braid conductance has been modified in order for the calculated and measured radiation shield stage temperatures to match. We suspect the conductance of this connection is lower than anticipated due to a compromised mechanical connection.

	Cold stage thermal load (W)	Rad. shield stage thermal load (W)
Mounting posts (conductive)	1.06	2.12
Wiring (conductive)	0.18	0.09
BBR (radiative)	0.19	2.31
Trap RF (dissipative)	0.47	0.23
Total	1.90	4.75

Chapter 3

Ion operations

Our apparatus is designed to utilize $^{40}Ca^+$ as the auxiliary ion for QLS operations. One primary benefit of Ca^+ is that it is technically simple to manipulate. The four lasers needed to address all transitions necessary for ground-state cooling and quantum-logic operations are all diode-based, in the visible or near-IR, and fiber compatible. Another consideration is that the auxiliary and molecular ions need to be of comparable charge-to-mass ratios α in order for both ions to have comparable participation in their shared motional modes to allow for efficient sympathetic cooling and quantum-logic operations. $^{40}Ca^+$ lies within an appropriate mass range to operate comfortably with molecules with masses ranging from approximately 15-100 atomic mass units.[1]

The first molecule we have investigated is CaH^+, which has served as a practical starting point. While this molecule is not especially remarkable with regards to, e.g., possible precision measurement applications, it is a convenient benchmark so as to compare to the work of Refs. [44, 46, 47]. CaH^+ has a relatively simple level structure because it is diatomic, has a nuclear spin of 1/2, and has zero electronic angular momentum and spin in its electronic ground state; it is also simple to form via reaction with H_2 from an already-trapped Ca^+ ion. We primarily manipulate the molecule's internal state with a pair of Raman beams, far-detuned from any internal transition.

In this chapter, I will discuss basic ion manipulations—including loading, cooling, and QLS operations—with a Ca^+-CaH^+ ion crystal. More technical details on the optical systems are provided in Appendix C.

---

[1] Other molecular experiments intent on studying molecules as light as ${H_2}^+$ [43] or as heavy as $RaOCH_3{}^+$ [63] operate with alternative auxiliary ions of a more suitable α.

3.1 Ion state manipulation via electromagnetic fields

The ions in our experiments have two sorts of degrees of freedom: internal and external. Internal degrees of freedom can involve a valence electron occupying different orbitals, vibration or rotation due to relative (lab-frame) motion of a molecule's constituent atoms, or smaller effects such as the orientation of electron or nuclear spin. External degrees of freedom describe the motion of the entire ion's center of mass, due either to secular motion or micromotion as described in Section 2.3.1. Coherent oscillating electromagnetic fields, typically in the form of laser light, allow for coherent control of these states. Discussion in this section will follow treatment from Refs. [51, 53, 64].

3.1.1 Internal degrees of freedom

An electromagnetic field oscillating at a frequency near that of a transition in a particle can induce population transfer between two states. Suppose the two states $|g\rangle$ and $|e\rangle$ have energy difference $\hbar\omega_0$ and the system has a non-zero dipole moment vector $\boldsymbol{\mu}$, which may be either permanent (in the molecule's reference frame) or induced by the coupling field. For a coupling electric field $\mathbf{E}(\mathbf{x}, t) = \mathbf{E}_0[e^{i(\vec{k}\cdot\vec{x}-\omega t)} + \text{c.c.}]$ at position $\vec{x}$ and time t (where the wave vector $\vec{k}$ is in the direction $\hat{k}$ of laser propagation, $|\vec{k}| \equiv k = \frac{2\pi}{\lambda}$, and λ is the wavelength of the field), the interaction Hamiltonian will take the form:

$$H_D = -\boldsymbol{\mu} \cdot \mathbf{E}(x, t). \tag{3.1}$$

In general, I will parametrize transition strengths by their *Rabi frequency* Ω; when the field is on resonance with the transition ($\omega = \omega_0$), population will completely transfer from one state to the other at time $\frac{\pi}{\Omega}$. The Rabi frequency for a transition that only changes internal degrees of freedom will be denoted Ω_0. For a dipole transition between $|g\rangle$ and $|e\rangle$:

$$\Omega_{0(D),g\leftrightarrow e} = \frac{\mathbf{E}_0 \cdot \langle g|\boldsymbol{\mu}|e\rangle}{\hbar}. \tag{3.2}$$

Not all of the transitions discussed in this thesis have a non-zero dipole moment vector. If instead the quadrupole moment is the leading-order interaction, the interaction Hamiltonian is given by:

$$H_Q = \frac{1}{6}\sum_{i,j} Q_{ij}\frac{\partial E_i}{\partial x_j}, \tag{3.3}$$

where Q_{ij} are the electric quadrupole moment tensor components. The additional gradient term leads to a relative decrease in Rabi frequency by a factor on the order of $a_0 k$ [51], where a_0 is the Bohr radius; that is, $\Omega_{0(Q)} \sim a_0 k \Omega_{0(D)} \approx \frac{\Omega_{0(D)}}{300}$ for wavelengths relevant to this thesis and assuming comparable electric field strengths.

Finally, most molecular transitions addressed in this work will be two-photon stimulated Raman transitions. Here, $|g\rangle$ and $|e\rangle$ are coupled via two light fields (with frequencies $\omega_{1(2)}$) through any short-lived excited state $|r\rangle$ that is (off-resonantly) dipole-coupled to both. The frequency difference $\omega_2 - \omega_1$ is tuned to match the frequency difference between $|g\rangle$ and $|e\rangle$. In this case, the resulting Rabi frequency will be $\Omega_{0(r)g\leftrightarrow e} = \sum_r \frac{2\Omega_{0(D),g\leftrightarrow r}\Omega_{0(D),e\leftrightarrow r}}{\Delta_r}$, where Δ_r is the detuning of one of the coupling fields from $|r\rangle$ and the sum is over all states $|r\rangle$ with the required couplings. The Raman transitions addressed in this work will be far-detuned, with $\Delta_r \approx 100$ THz $\ggg \Omega_{0(D)}$, and thus will have considerably lower Rabi frequencies than a directly-driven dipole transition assuming comparable electric field strengths. In practice, this means the intensity of the laser beams driving Raman transitions will typically be much higher than other lasers in the system.

3.1.2 External degrees of freedom

A laser field can coherently add or remove motional quanta from an atom or molecule because the particle's finite wavefunction extent samples a gradient across the wavelength of the field. The strength of this interaction is parametrized by the Lamb-Dicke parameter η:

$$\eta_{\text{mot}} = \vec{k}\cdot\hat{u}_{\text{mot}}\sqrt{\frac{\hbar}{2m\omega_{\text{mot}}}} = \vec{k}\cdot\hat{u}_{\text{mot}}a_0, \tag{3.4}$$

where mot indexes the addressed motional mode, $\hat{u}_{\text{mot}}$ is the unit vector along the direction of the mode, m is the ion mass, ω_{mot} is the mode's frequency, and a_0 is the extend of the ground-state wavefunction. For the wavelengths, motional modes, and ion masses considered here, η_{mot} will range from 0.05 to 0.1; we thus consider ourselves to be in the Lamb-Dicke regime, where $\eta\sqrt{n+1} \ll 1$. In this regime, the Rabi frequency $\Omega_{n\leftrightarrow n+1}$ of a transition that adds one quantum (along with changing the internal state) is given by:

$$\Omega_{n\leftrightarrow n+1} \approx \Omega_0 \eta \sqrt{n+1}, \tag{3.5}$$

where Ω_0 is the Rabi frequency of the same transition with no motional state change. Transitions that do not change the motional state are called *carriers*, transitions that are ω_{mot} lower in frequency than the carrier are *red sidebands* (RSBs), and those ω_{mot} higher are *blue sidebands* (BSBs). From Eq. 3.5, sideband transitions are slower by a factor of $\sim \eta$ compared to carriers.[2] Another notable feature is that the sideband Rabi frequency depends upon the motional state of the atom or molecule.

Micromotion sidebands, for which the sideband frequency $\omega_{\text{MM}} = \Omega_{RF}$, can be driven by a similar process [54, 65]. In this case, the Rabi frequency of the of the l^{th} micromotion sideband is given by:

$$\Omega_l = \Omega_0 J_l(\beta), \tag{3.6}$$

where β is the *micromotion modulation index*, which scales with the RF electric field amplitude projection on $\hat{k}$ at the ion position, and J_l is the l^{th}-order Bessel function. In experiments described in this thesis, we will be primarily interested in minimizing the observed $J_1(\beta)$ as a function of applied, compensating DC fields in order to minimize micromotion of the trapped ions.

---

[2] Higher-order sidebands ($\Delta n > 1$) can also be driven but will be slower by a factor of $\sim \eta^{|\Delta n|}$. Because of this prohibitive slowdown, we typically operate with $|\Delta n| \leq 1$.

3.2 Ca$^+$ operations

The internal level structure of ^{40}Ca$^+$ relevant for the operations in this experiment is shown in Fig. 3.1. The ion has a single valence electron and nuclear spin 0. We apply a magnetic quantization field of 0.40 mT to split each atomic state into Zeeman sublevels separated by O(MHz).

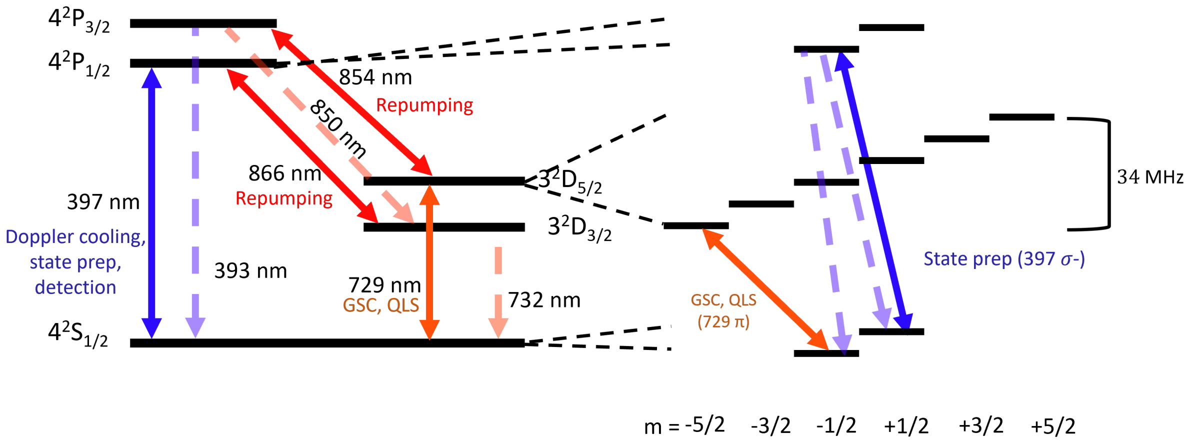

Figure 3.1: The relevant energy levels of Ca$^+$ accessed in our experiment. Solid lines represent laser fields we apply to the ion, while dashed lines indicate transitions accessed as possible decay channels. In a 0.40 mT magnetic field, the energy levels are separated into Zeeman sublevels with splittings of O(MHz), which are shown for select levels in the right portion of the figure. State preparation pumps population into the $|S_{1/2}, m = -1/2\rangle$ state with high probability, while ground-state cooling and coherent quantum-logic operations are performed on the $|S_{1/2}, m = -1/2\rangle \leftrightarrow |D_{5/2}, m = -5/2\rangle$ transition.

The $S_{1/2} \leftrightarrow P_{1/2}$ transition (397 nm) is a dipole transition with an excited state lifetime of just 8 ns [56], making it an ideal fast cycling transition for Doppler cooling and fluorescence detection. Meanwhile, the $S_{1/2} \leftrightarrow D_{5/2}$ transition (729 nm) is a narrow quadrupole transition with an excited state lifetime of 1 s [66]. It is primarily used to drive coherent, motional sideband-resolving transitions for ground-state cooling and quantum-logic operations. The long-lived D levels—which may be populated either purposefully via 729 nm operation or accidentally via a low-probability decay channel from the P levels—are depopulated (*repumped*) via dipole transitions (854 and 866 nm) to the P levels, from which decay back to the ground $S_{1/2}$ state occurs quickly with high probability. All of the laser systems used to address Ca$^+$ are frequency-locked to a spherical cavity.

The cavity axis to which the 729 nm laser is locked has a measured finesse of 3.2×10^5 [55].

All of the aforementioned laser light is sent through double-passed acousto-optic modulators (AOMs) for fast power and frequency control; we obtain ∼160 MHz frequency modulation range for each Ca^+ beam. After the AOMs, light is primarily sent to the ion though two paths: the π port, which propagates perpendicular to the quantization B field, and the σ port, propagating parallel to the B field. The direction and polarization of the beams affect which transitions can be driven and how strongly. A summary of all of the optical paths and associated applications is found in Table 3.1, and detailed diagrams are provided in Appendix C.

Another important aspect of the optical setup is the imaging system, which collects photons emitted from Ca^+ through a re-entrant viewport above the trap, achieving a numerical aperture (NA) of approximately 0.4. A motorized flip mirror either allows the light to pass to a single photon detector (quoted quantum efficiency 65% at 397 nm) or reflects it to a camera, which allows us to differentiate ion number up to a few ions and distinguish ion order when a dark ion is present. A vertical 729 nm beam can be sent to the ion through the imaging optics for micromotion minimization.

3.2.1 Loading

Ca^+ is loaded in our trap via ablation. A 90-10 Al-Ca alloy is used as the ablation target; it is installed within the endcap, recessed by 1.2 mm from the endcap face and 7.0 mm away from the trap center. A Q-switched microchip 1030 nm laser (pulse duration 500 ps, repetition rate 9 kHz, pulse energy 40 μJ) is used as the ablation laser. Ablation light is sent through an AOM to control the power and beam pointing in one dimension before being focused onto the ablation target. For typical loading conditions, pulse energies after the AOM are ∼10 μJ; the laser is focused by an $f = 150$ mm lens to a spot size of ~ 35 μm diameter. The ablation laser is turned on to the target for ∼10 ms intervals while high-intensity, 400 MHz red-detuned, 397 nm cooling light is applied to the trapping region. An RF drive is applied to the comp_H electrode at the frequency of a radial

---

[3] $\rightarrow$ and $\uparrow$ denote direction of linear polarization; note that $\uparrow$ has no projection along the quantization axis. ↻ denotes circular polarization with σ^- orientation.

Table 3.1: Laser systems summary

wavelength **transition**	**uses**	**typ. power (mW)/** **beam waist (μm)**	**port(s)[polarization[3]]**
397 nm $S_{1/2} \rightarrow P_{1/2}$	Doppler cooling detection state preparation	0.01/15	$\pi[\rightarrow]$, $\sigma[\circlearrowright]$, vert. (fluorescence detection)
729 nm $S_{1/2} \leftrightarrow D_{5/2}$	ground-state cooling quantum-logic operation micromotion drive	10/25	$\pi[\uparrow]$ $\sigma[\uparrow]$, vert.$[\rightarrow]$ (MM drive)
866 nm $D_{3/2} \rightarrow P_{1/2}$	repumping	0.03/30	$\pi[\uparrow]$
854 nm $D_{5/2} \rightarrow P_{3/2}$	repumping	0.03/30	$\pi[\uparrow]$
1064 nm mol. sublevels	pumping spectroscopy preparation/detection	200/15	$\pi[\rightarrow]$, $\sigma[\circlearrowright]$

secular motional mode for a single-Al^+ ion to suppress loading of unwanted Al^+. A standard ion detection sequence (see Section 3.2.2) is then applied to check for the presence of an ion. If no ion is detected, the process repeats with ~1 Hz duty cycle. If the loading process is repeatedly unsuccessful, the beam pointing is rastered to hit other spots on the target and the beam power is incrementally increased. A Ca^+ ion is typically loaded within 1-3 minutes. Photoionization light is not normally used.

Ablation loading in this system has come with some problems. Undesired loading of Al^+ ions, while manageable, has prompted us to attempt using other types of ablation targets. A pure Ca target was installed, but was exposed to air for too long and thus oxidized without being tested. A $CaTiO_3$ target was successfully used for several months, after which time a (presumed Ti) short formed on the trap wafer, prompting us to return to the Al-Ca target. An additional problem is that ablation loading in a cryogenic environment for months at a time caused a persistently increasing stray field. The stray field was reduced by going to room temperature for several days, and the effect has been mitigated by loading at the geometrical axial center of the trap rather than the (axially offset) axial micromotion minimum, attributed in part to the lower ablation powers required to load at this location.

3.2.2 Doppler cooling and detection

The first step to cooling a hot ion is Doppler cooling, in which many red-detuned 397 nm photons are repeatedly absorbed and then re-emitted on resonance by the ion (repump lasers are also applied during this sequence). Because (on average) the emitted photons are of higher energy than the absorbed photons, the ion loses energy during this process until it reaches an equilibrium *Doppler limit* temperature set by the recoil energy of the emission. We use the 397 nm π light, which has sufficient projection ($\hat{k} \cdot \hat{u}_{\mathrm{mot}}$) on all motional normal modes for simultaneous cooling. The theoretical Doppler limit temperature—determined by the photon energy, mode frequency, and beam geometry—is $\bar{n} \lesssim 10$ for all of our motional modes.

The first stage of our Doppler cooling sequence is *precooling*, in which the 397 nm light is detuned red of the first micromotion sideband; we typically operate with a precooling duration of 500 μs. In the second stage, we Doppler cool with the 397 nm light detuned to where the slope of the absorption spectrum is maximized—in our case, 17 MHz red of resonance. Pulse parameters (powers, frequencies, and durations) are optimized experimentally; we approach the Doppler limit after 200 μs of near-detuned cooling.

For detection, the 397 nm light is tuned onto resonance to maximize the total number of photons scattered; 866 nm repump light is used as well. Again, parameters are tuned experimentally for optimal performance. The purpose of detection is to most efficiently differentiate the ion fluorescing on $S_{1/2} \leftrightarrow P_{1/2}$ vs not fluorescing (e.g., because it occupies $D_{5/2}$). With this in mind, we set the 397 nm power slightly below saturation to minimize background scattering of 397 nm light to the single photon detector. We register 16 counts from the ion compared to 0.4 background counts in a 100 μs detection window.

3.2.3 Ground-state cooling and coherent operations

The $S_{1/2} \leftrightarrow D_{5/2}$ quadrupole transition, unlike the $S_{1/2} \leftrightarrow P_{1/2}$ transition used for Doppler cooling and fluorescence detection, is narrow enough to resolve both motional sidebands and Zeeman sublevels. We address the $|S_{1/2}, m = -1/2\rangle \leftrightarrow |D_{5/2}, m = -5/2\rangle$ transition with the vertically-polarized 729 nm π beam for both ground-state cooling and coherent operations. In this orientation, $|\Delta m| \neq 2$ transitions are forbidden; see, e.g., Ref. [67] for more details on other possible orientations.

We use continuous sideband (CSB) cooling [68] to bring certain motional modes from the Doppler limit temperature to the ground state. Conceptually, this requires the following steps:

(1) **State Preparation:** We prepare the state in $|S_{1/2}, m = -1/2\rangle$ using the 397 nm σ^--polarized beam. Since this polarization can only excite population out of $|S_{1/2}, m = +1/2\rangle$, but the excited state can decay to either $S_{1/2}$ sublevel, the ion is asymptotically prepared in $|S_{1/2}, m = -1/2\rangle$ after just 2 μs. The situation is illustrated in the right panel of Fig. 3.1.

(2) **Resolved Sideband Drive:** The 729 nm π beam drives the $|S_{1/2}, m = -1/2, n = n_i\rangle \rightarrow |D_{5/2}, m = -5/2, n = n_i - 1\rangle$ RSB, reducing the motional excitation by one quantum.

(3) **Repumping:** 854 nm light removes population from the naturally long-lived $D_{5/2}$ state.

For CSB cooling, all of these actions are performed simultaneously. Performance is particularly sensitive to repump power, which is tuned experimentally.

To quantify the efficacy of cooling, we can compare the population transfer $|S_{1/2}, m = -1/2, n = n_i\rangle \rightarrow |D_{5/2}, m = -5/2, n = n_i \pm 1\rangle$, using a BSB or RSB pulse to add or remove a quantum of motion. For an ion cooled near the ground state the RSB will exhibit lower population transfer because population already in the ground state has no lower motional state to occupy, and thus the transition is forbidden. If the motional population is assumed to be thermally distributed, the ground-state population fraction P_0 is simply [69]:

$$P_0 = 1 - \frac{P_{RSB}}{P_{BSB}} \approx 1 - \bar{n}, \tag{3.7}$$

where $P_{RSB(BSB)}$ is the population transferred after an RSB(BSB) pulse. For example, after CSB cooling our axial OOP mode (at 4.4 MHz, see Section 3.3.2) for 700 μs, we observe a final $P_0 \approx 0.90$ ($\bar{n} \approx 0.10$). The sideband contrast, BSB coherence, and cooling/heating rates of this mode are shown in Fig. 3.2.

The 729 nm π beam is used to perform coherent operations on the $S_{1/2} \leftrightarrow D_{5/2}$ transition. Coherent operations do not necessarily require cooling to the ground state; however, high-fidelity operations that change the ion's motion do require ground-state cooling because of the n-dependence of Eq. 3.5.

3.2.4 Micromotion minimization

To measure micromotion in 3 dimensions, we use our 729 nm π, σ, and vertical beams. We compare the π-time at a particular power level on a carrier transition to one of the first micromotion sidebands. For the π and vertical beams we address the $|S_{1/2}, m = -1/2\rangle \leftrightarrow |D_{5/2}, m = -5/2\rangle$ transition; for the σ beam condition this transition is forbidden, and we instead use the $|S_{1/2}, m = -1/2\rangle \leftrightarrow |D_{5/2}, m = -3/2\rangle$ transition. In either case, the stray RF electric field at the ion in the direction of probe laser's wave vector can be calculated as:

$$\vec{E} \cdot \hat{k} \equiv E_{\hat{k}} = \frac{\beta \Omega_{RF}^2}{\alpha k}. \tag{3.8}$$

Using Eq. 3.6 and the fact that $J_1(x) \approx \frac{x}{2}$ near $x = 0$, β is found experimentally from the ratio of the micromotion sideband Rabi frequency compared to that of the carrier as $\beta \approx 2\frac{\Omega_1}{\Omega_0}$. If the laser fields at the carrier and sideband are not equal in amplitude, the calculation must be scaled accordingly.

Radial micromotion, attributed primarily to stray charge, is minimized by biasing comp$_H$ and comp$_V$. Residual axial micromotion, attributed to imperfections in trap geometry, is minimized by moving the ion axially via the relative endcap voltages. The minumum axial micromotion is found

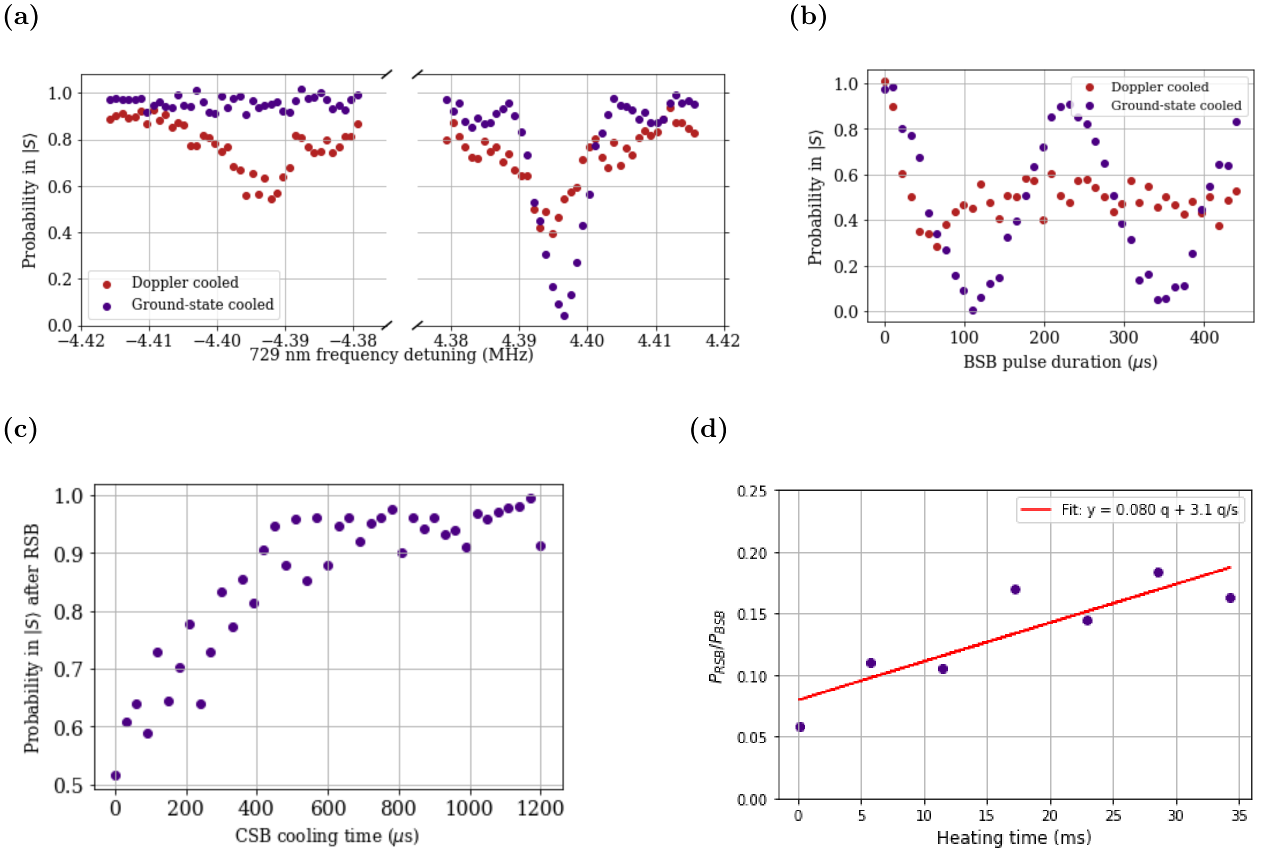

Figure 3.2: Cooling and heating of the axial OOP motional mode. For all experiments the ion is prepared in $|S_{1/2}, m = -1/2\rangle$, and then a sideband pulse attempts to drive the $|S_{1/2}, m = -1/2, n = n_i\rangle \rightarrow |D_{5/2}, m = -5/2, n = n_i \pm 1\rangle$ transition. **(a) Frequency scans across the RSB and BSB.** The strong asymmetry after ground-state cooling is characteristic of $P_0 \approx 1$. All scans are done at a 110 μs pulse duration. **(b) Time scans on the BSB.** When the ion is Doppler cooled and thus distributed over many n, it does not flop coherently because of the n-dependence of the Rabi frequency. **(c) RSB drive after a cooling pulse of variable length.** During experiments, we typically apply CSB cooling for 700 μs before experimental operations. **(d) Heating rate measurement.** The data is taken by ground-state cooling, waiting a variable delay (the "heating time") without applying any light, and then measuring either the RSB or BSB contrast. We can then take the ratio over many trials to estimate $\bar{n}$ according to Eq. 3.7. The linear fit indicates a base temperature of 0.08 quanta and a heating rate of 3.1 quanta/second for this mode.

at a location displaced 180 μm axially from the trap center. For final compensation, we minimize Ω_1 (vertical) with comp$_H$ and Ω_1 (π) with comp$_V$, ideally pushing residual micromotion into the σ axis. Under typical experimental conditions, the measured RF electric field at the compensated position is approximately $E_\pi = 310$ V/m, $E_{\text{vert.}} = 130$ V/m, and $E_\sigma = 190$ V/m; this corresponds to $J_1(\beta) \lesssim 0.05$ in each direction. The primary effect of this residual micromotion is a systematic shift in the molecular sublevel splittings; the observed fields lead to shifts of O(100 Hz) [46].

3.3 CaH$^+$ operations

3.3.1 Loading

To load a Ca$^+$-CaH$^+$ crystal, we begin by loading 2 Ca$^+$ via ablation as detailed in Section 3.2.1. Loading of a second Ca$^+$ ion is similar to loading of the first, though marginally lower ablation pulse energies and durations are required due to the beneficial sympathetic cooling effect of the already-trapped ion. Once two Ca$^+$ ions are loaded, we aim for CaH$^+$ formation via the reaction Ca$^+(4^2P_{1/2})$ + H$_2$ → CaH$^+$ + H; note that this reaction is only energetically allowed for Ca$^+$ initially in the excited $P_{1/2}$ state. To introduce H$_2$ in our system immediately after cooling to cryogenic temperatures, we send in a few dozen pulses of H$_2$ via the molecular beam, some of which becomes cryo-adsorbed onto the cold-stage components near the trap. Subsequently, when attempting to load CaH$^+$, we simply elevate the system temperature slightly (16 K → 19 K as read by a sensor near the trap). Because our system temperature sits near the H$_2$ adsorption/desorption threshold, this small temperature increase leads to a large, fast outgassing effect (we observe a pressure increase to 10^{-7} Pa at the room temperature stage, though the pressure at the ions is likely higher). We also run the 397 nm π beam above saturation of the $S_{1/2} \to P_{1/2}$ transition at high duty cycle to maximize the time spent in the $P_{1/2}$ state. Formation of CaH$^+$ is identified by observing a decrease in fluorescence counts, since these scale with the number of Ca$^+$ ions in the trap. With this process, we typically form CaH$^+$ within 1-3 minutes, at which point we immediately lower the 397 nm power and reduce the system temperature to prevent a second reaction from occurring.

In general, we plan to introduce molecules to our trap volume for loading purposes via the molecular beam; introducing gas via temperature elevation only makes sense in this special case. If we were to achieve a lower base temperature, loading CaH$^+$ from a beam of H$_2$ may well be desirable.

3.3.2 Motional mode structure

With a Ca^+-CaH^+ ion crystal, we typically operate with the motional mode structure shown in Table 3.2.

Table 3.2: Ca^+-CaH^+ motional normal modes

Mode geometry	**Frequency (MHz)/2π**
axial IP	2.6
axial OOP	4.4
radial IP	3.8, 4.0
radial OOP	2.8, 3.1

We use the axial OOP mode at 4.4 MHz as the *quantum-logic mode* that serves as an information bus between the two ions. Using a higher-frequency mode is advantageous because it has lower heating rates and less off-resonant drive of/from the carrier compared to a lower-frequency mode.[4] Additionally, OOP modes (compared to IP modes) are minimally sensitive to heating, since the relative effect of voltage fluctuations on each ion will be nearly in phase with little variation in magnitude across the two ions.

Motion in the radial OOP modes induces frequency shifts in the axial OOP mode due to a nonlinear, parametric coupling effect (explored in [70]; see Fig. 3.3). To mitigate this, we CSB cool the radial OOP modes to $\bar{n} < 1$ and place the mode frequencies as far as feasible from half the axial OOP mode frequency. We also CSB cool the axial IP mode to minimize possible Debye-Waller effects. Total CSB cooling time for all 4 of these modes is 3.1 ms.

---

[4] It would be nice to push the quantum-logic mode to an even higher frequency. Technical constraints include maintaining frequency separation ($\gtrsim$ 200 kHz) between all modes, achievable DC voltages (limited by amplifier max output and risk of breakdown between trap chip electrodes), and minimizing dissipative thermal load from the trap RF.

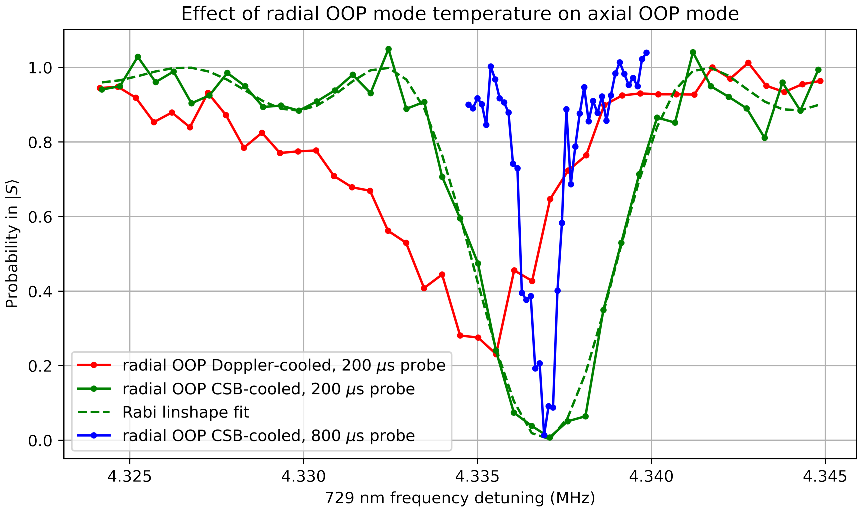

Figure 3.3: Excitation of the $|S_{1/2}, m = -1/2, n = 0\rangle \leftrightarrow |D_{5/2}, m = -5/2, n = 1\rangle$ BSB transition for the axial OOP mode. Motion in the radial OOP modes leads to a shift in the axial OOP mode frequency; the frequency offset, loss of contrast, and asymmetric lineshape of the BSB with Doppler (as opposed to CSB)-cooled radial OOP modes are all characteristic of a thermal temperature distribution near the Doppler limit. By ground state cooling the radial OOP modes, the axial OOP mode demonstrates a near-Fourier-limited lineshape with an 800 μs probe.

3.3.3 CaH$^+$ internal structure

Following the discussion from Section 2.1, CaH$^+$ has electronic, vibrational, rotational, and rotational Zeeman level splittings. Its electronic and vibrational structure is investigated in Ref. [71]. We will primarily be interested in its ground electronic and vibronic state, which the molecule will occupy more than 99% of the time in equilibrium.

CaH$^+$ has rotational energy levels at $E_J = B_R J(J+1)$ with $J = 0, 1, 2, \ldots$ and $2(2J+1)$ multiplicity of sublevels from the projection of rotational angular momentum ($\hat{\boldsymbol{J}} \rightarrow m_J = -J, -J+1\ldots, +J$) and nuclear spin ($\hat{\boldsymbol{I}} \rightarrow m_I = \pm 1/2$ from the H nucleus) onto the quantization axis. An applied quantization field ($\boldsymbol{B} \rightarrow |B| = 0.40$ mT for experiments presented) separates the sublevels. The situation is described by the following Hamiltonian:

$$\hat{H}_{rot,spin-rot} = \frac{1}{\hbar}(2\pi B_R \hat{\boldsymbol{J}}^2 - g\mu_N \hat{\boldsymbol{J}} \cdot \boldsymbol{B} - g_I \mu_N \hat{\boldsymbol{I}} \cdot \boldsymbol{B} - 2\pi c_{IJ} \hat{\boldsymbol{I}} \cdot \hat{\boldsymbol{J}}), \tag{3.9}$$

where μ_N is the nuclear magneton, g and g_I are the g-factors, and c_{IJ} is the spin-rotation coupling coefficient (see Table 3.3 for CaH$^+$-specific values). We operate at an intermediate magnetic field for which the last three terms in Eq. 3.9 all contribute similarly; sublevels are spaced by O(10 kHz).

Table 3.3: Theoretical CaH$^+$ molecular constants for $\nu = 0, J = 1$ [44]

B_R	g	c_{IJ}
142.5 GHz	-1.35	8.26 kHz

We define quantum numbers as J, $m = m_I + m_J$,[5] and $\xi = \pm$, where ξ differentiates states with the same J and m but opposite parity of the superposition of product states. A more complete description of the calculation of eigenstates is provided in the Methods section of Ref. [44].

In Fig. 3.4, the sublevel structure of $J = 0, 1$, and 2 is shown. Transitions between sublevels are addressed via far-detuned Raman beams. We use two paths of 1064 nm light for this purpose, though in the far-detuned regime the strength of the drive is not sensitive to the choice of wavelength. Each path includes an AOM double pass before continuing on to the ion with π or σ^- polarization. A frequency difference of O(kHz) or O(MHz) is used to drive Raman carrier or sideband transitions, respectively, between sublevels within a rotational manifold; selection rules stipulate that we can drive only $\Delta m = \pm 1$ transitions. We identify a *signature manifold* consisting of two sublevels within each rotational manifold with $J > 0$. We label the manifold as $|i_J\rangle \equiv |J, -J - 1/2, -\rangle$ and $|ii_J\rangle \equiv |J, -J + 1/2, -\rangle$. The *signature transition* $|i_J\rangle \leftrightarrow |ii_J\rangle$ has a unique frequency (differing by $\gtrsim$1 kHz at 0.40 mT) for each J within the vibronic ground state manifolds, so it can be used for unambiguous state differentiation. All cooling occurs sympathetically via Ca$^+$, and all read-out is done via QLS.

3.3.4 Quantum-logic spectroscopy for state readout

Like most molecules, CaH$^+$ does not have a closed cycling transition analogous to the $S_{1/2} \leftrightarrow P_{1/2}$ detection transition in Ca$^+$ because any excited electronic state can decay into many

---

[5] We unfortunately use m to denote both atomic and molecular Zeeman sublevels, following conventions of prior works. The intended meaning should be clear from context.

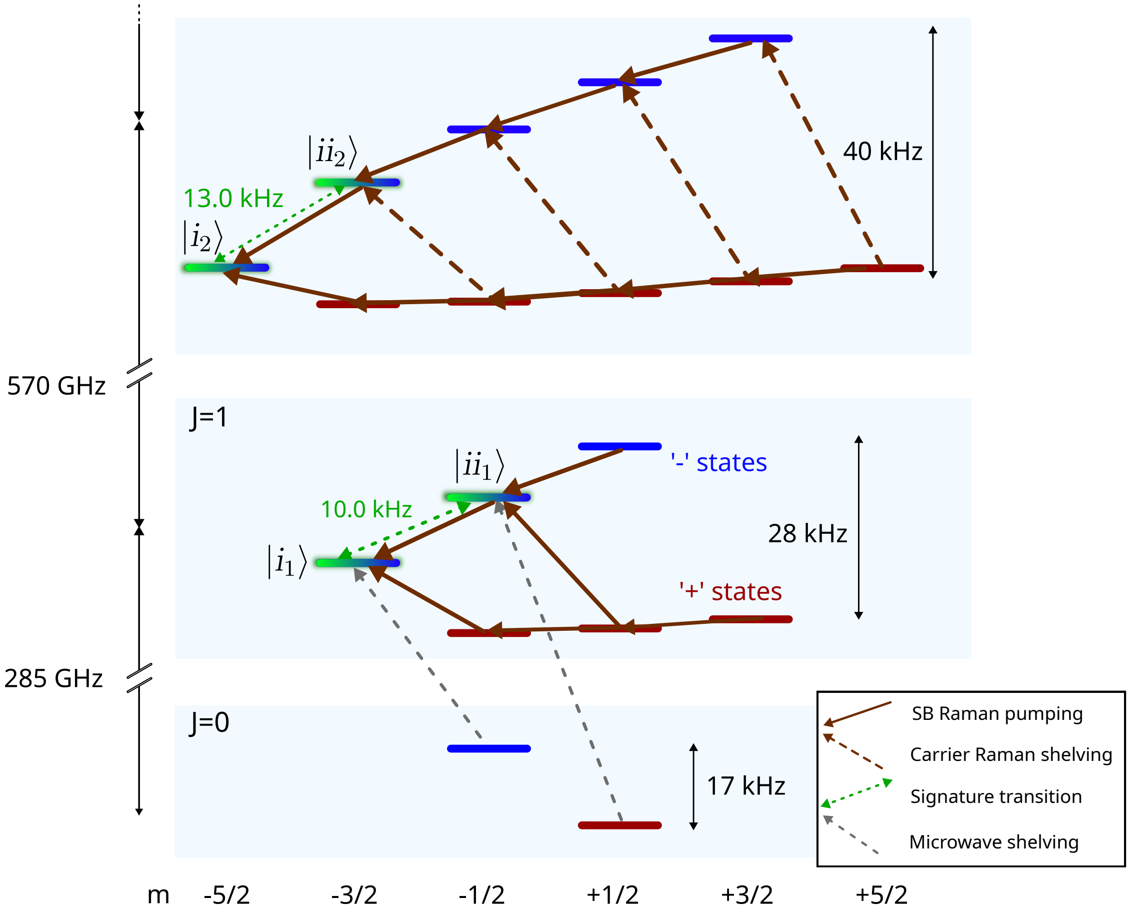

Figure 3.4: Levels structure for $J = 0, 1,$ and 2 in CaH$^+$; in thermal equilibrium in a 16 K BBR environment, the ion's population fraction in these levels will be $> 99\%$. To concentrate the molecular population from an unknown distribution across sublevels, a sequence of pumping pulses is applied, which should move the molecule to $|i_J\rangle$. To project and detect the molecule into the signature manifold (green highlights), successive signature transition probes are applied. Microwave shelving removes the population from the long-lived $J = 0$ manifold.

vibrational states, as depicted in Fig. 1.1. We therefore must utilize a different method to detect the molecular state; for this, we use QLS on the signature transition. The protocol is shown in Fig. 3.5. In brief, the quantum-logic mode is cooled to the ground state and the atom is prepared in $|D_{5/2}, m = -5/2, n = 0\rangle$. The Raman beams are then switched on, nominally tuned to a signature transition's motion-adding sideband. If the transition is successfully driven, the ion crystal's motional state is changed from $n = 0 \rightarrow 1$. A subsequent Ca$^+$ BSB pulse maps this change onto the atom's electronic state, where it can be efficiently read out with fluorescence detection. Detection in $|S\rangle$

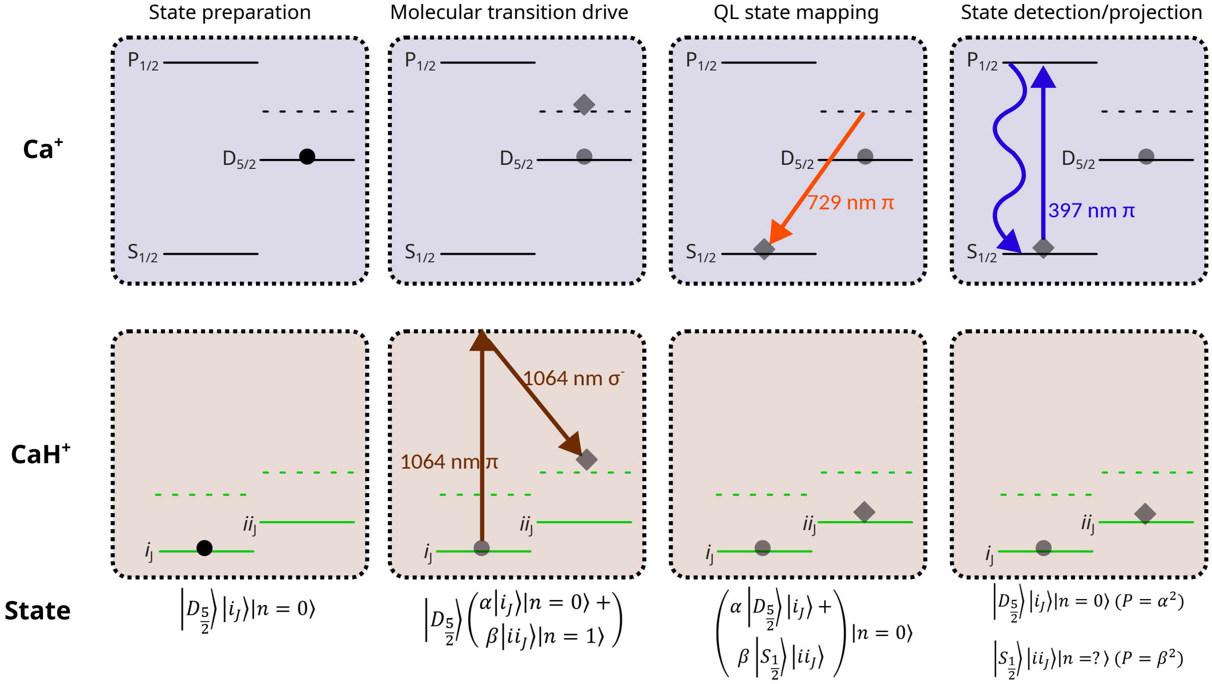

Figure 3.5: QLS protocol for driving and detecting a molecular signature transition. **State preparation:** The molecule is treated as occupying a signature manifold state (in this illustration i_J, e.g., after pumping), while the atom is prepared in $|D_{5/2}, m = -5/2\rangle$. The ions are cooled to their ground state of motion via CSB cooling and projective purification. **Molecular transition drive:** Raman beams address the molecule, detuned to the motion-adding sideband of the signature transition. If successful (probability β^2 in this illustration), the drive will change both the molecular state and the motional state of the ion crystal. **QL state mapping:** A BSB π pulse on the $|D_{5/2}, m = -5/2\rangle\, |n = 1\rangle \rightarrow |S_{1/2}, m = -1/2\rangle\, |n = 0\rangle$ Ca$^+$ transition, which will only change the atomic state if $n > 0$, maps the molecular state to the atomic electronic state. **State detection/projection:** Fluorescence detection reveals the result of the molecular drive. A bright result projects the molecule into the signature manifold with high probability, since the signature transition is at a unique frequency within the molecular level structure.

indicates a successful signature transition drive and projects the molecule into the interrogated signature manifold with high probability.

Since the fidelity of the QLS readout relies directly on proper state preparation of $|D_{5/2}, m = -5/2\rangle\, |n = 0\rangle$, we introduce additional projective purification steps[6] [44] to ensure high-fidelity Ca$^+$ state preparation by exploiting the high-fidelity single-shot fluorescence detection distinguishing $|S\rangle$ and $|D\rangle$. First, we perform CSB cooling on the axial IP, both radial OOP, and finally the quantum-logic mode.

---

[6] Otherwise, our false positive rate would be limited to our temperature after CSB cooling of $\bar{n} \approx 0.1$, as well as our 729 carrier π pulse fidelity.

Next, we drive a 729 carrier π pulse on $|S_{1/2}, m = -1/2\rangle \rightarrow |D_{5/2}, m = -5/2\rangle$. We then attempt a fluorescence detection; a dark result indicates we have successfully transferred population to the $D_{5/2}$ level. After that, we attempt a (nominally forbidden) BSB ($|D_{5/2}, m = -5/2\rangle |n = n_i\rangle \rightarrow |S_{1/2}, m = -1/2\rangle |n = n_i - 1\rangle$), which should only transfer population back to $S_{1/2}$ if the ion is not in $n_i = 0$. A final fluorescence detection determines the result. If either of these two detection attempts yields $|S\rangle$, the entire cooling process is restarted. With this projective purification step, $|D_{5/2}, m = -5/2\rangle |n = 0\rangle$ is prepared with $\gtrsim 99\%$ probability.

3.3.5 Molecular state preparation

To prepare the molecule in a particular sublevel, we perform the following steps:

(1) **Pumping to $|i_j\rangle$**: For a particular rotational manifold, we apply a sequence of Raman drives to move population from any initial sublevel to $|i_j\rangle$. We achieve directionality by first CSB cooling, then applying motion-adding sidebands (which also drive molecular transitions) that are followed by a brief (200 μs) CSB cooling pulse to reset to the ground motional state with high probability. Certain transitions with $\xi_{\text{initial}} \neq \xi_{\text{final}}$ couple so weakly as to make sideband pulses prohibitively weak; in this case, we pump the $\xi = -$ manifold to the extreme state with directional pulses, shelve $\xi = + \rightarrow \xi = -$ via carrier transitions as necessary, and finally pump the $\xi = -$ manifold again.

$J = 0$, the longest-lived rotational manifold, presents a special case. It has no allowed intra-manifold Raman transition and thus cannot be directly detected. We circumvent this problem by shelving $J = 0 \rightarrow 1$ with our 285 GHz source. The pumping scheme for $J = 0, 1$, and 2 is illustrated in Fig. 3.4.

Each pumping pulse takes ∼1 ms and the full pumping sequence takes ∼6 ms for $J = 1$ and ∼12 ms for $J = 2$. Furthermore, if the population is initially in a sublevel that requires many pumping pulses to move to $|i_j\rangle$, it may have pumping efficiency $\lesssim$50% due to imperfect calibration and population transfer, and thus the pumping sequence may need to be repeated.

However, once the molecular population is found, a full pumping sequence is typically only required after a TR interaction causes a rotational transition; this occurs on a timescale of O(10 seconds) for CaH^+ in our system.

(2) **Checking the signature transition:** If we can drive a signature transition sideband and detect a state change via QLS, we will have detected and projected the molecule into that signature manifold. We typically attempt multiple signature transition probes to build confidence and leave the molecule in the desired sublevel; this procedure is discussed further in Chapter 4. Normally, we begin an experiment by preparing the molecule in one of the two signature manifold sublevels. If another initial state is desired, additional pulse(s) can be used to reach that state.

When attempting to prepare the molecular state from an unknown initial state, we typically alternate between pumping+checking $J = 1 - 3$ (and shelving out of $J = 0$) until the state has been projected into one of the signature manifolds. Since this allows us to track the molecular state >95% of the time, and pumping rotational levels with $J > 3$ is more challenging, we are content to let TR stochastically bring the ion back into $J \leq 3$ as necessary.

3.3.6 The signature transition

Driving the signature transition is central to our molecular SPAM operations. To resolve sublevel splitting differences as small as 1 kHz, we must attempt commensurately narrow signature transition probes. To maintain maximum contrast on such a probe, we need to stabilize the frequency of the signature transition drive to within ∼100 Hz over the course of an experiment. Since the signature transition probes are motional sidebands, this requires stabilizing the quantum-logic mode frequency as well as the rotational Zeeman energy splittings.

3.3.6.1 Stabilizing the quantum-logic mode frequency

We measure the quantum-logic motional mode frequency by CSB cooling, applying a 2 ms-long RF tickle (oscillating voltage) drive on an endcap electrode near the mode frequency, and shelving via $|S_{1/2}, m = -1/2\rangle\,|n = n_i\rangle \rightarrow |D_{5/2}, m = -5/2\rangle\,|n = n_i - 1\rangle$ before detection; we obtain a lineshape that is close to Fourier limited. We find that the mode exhibits significant drifts when running our 729 and/or 1064 nm beams at relatively high power and duty cycle (such as when running a molecular spectroscopy experiment), likely due to thermal or charging effects. We therefore perform frequent ($\sim$1 per 15 seconds), interleaved feedback during experiments by measuring the relative excitation on the slope on either side of the desired mode frequency and feeding back on the endcap voltages accordingly. We estimate that we maintain mode frequency stability of $\lesssim 50$ Hz deviation over the course of an experiment. We are limited both by the speed of the drift and by the resolution of the 16-bit DACs that control our endcaps. We find that we can partially saturate the drift effect (and thus mitigate the subsequent drift speed) by "pre-charging[7]" the apparatus by leaving our 729 nm vertical beam on at maximum power for approximately 30 seconds before starting experiments at the beginning of the day or after an extended break.

3.3.6.2 Stabilizing the rotational Zeeman level structure

A number of factors can cause day-to-day, hour-to-hour, or even minute-to-minute shifts of O(100 Hz) in the rotational Zeeman energy splittings. Roughly in order of slowest to fastest, these include drifts in magnetic field, light shifts due to changes in Raman beam polarization, micromotion drift, and light shifts from changes in intensity or beam-pointing. We calibrate each of these factors at intervals appropriate to the drift rate they cause. During the calibration experiments, the ion order is swapped so the atomic ion can serve as an in-situ sensor of the parameter being calibrated at the normal molecular ion position.

We typically calibrate magnetic field and Raman beam polarization once per day. An illustration of these calibration operations is shown in Fig. 3.6. $|B|$ is found by dividing the measured

---

[7] Or perhaps pre-thermalizing

difference in frequency between the $|S_{1/2}, m = -1/2\rangle \leftrightarrow |D_{5/2}, m = -5/2\rangle$ and $|S_{1/2}, m = -1/2\rangle \leftrightarrow |D_{5/2}, m = +3/2\rangle$ transitions by $\frac{\mu_B}{2h} = 67.18$ MHz/mT, where μ_B is the Bohr magneton. A current source is adjusted as necessary to set the current flowing through the B-field-generating coils such that the field is 0.40 mT. Polarization is optimized by using the Raman beams to drive transitions between Zeeman levels within the $D_{5/2}$ manifold. Maximizing the Rabi frequency of the $|D_{5/2}, m = -5/2\rangle \leftrightarrow |D_{5/2}, m = -1/2\rangle$ transition (with 1064 π detuned blue of 1064 σ) by adjusting the waveplates setting the 1064 π beam polarization allows us to minimize the σ^+ component of the π beam, while doing so for the $|D_{5/2}, m = -5/2\rangle \leftrightarrow |D_{5/2}, m = -3/2\rangle$ transition (now with 1064 π detuned red of 1064 σ) by adjusting the waveplates setting the 1064 σ^- beam polarization allows us to minimize the σ^+ component of the σ^- beam. The protocol is illustrated in Fig. 3.6. To minimize the rate of polarization drifts, each Raman beam passes through a polarizer after coming out of a polarization-maintaining fiber and has only one reflection from a metallic mirror located before the waveplates; see Appendix C.

Micromotion is a symptom of RF field at the ion that shifts the levels. We measure and minimize micromotion in the radial directions between experiment runs, or via an interleaved tracking experiment called about once per minute during long, sensitive experiment runs.

With our high Raman beam intensities and low sublevel splittings, light shifts can be very problematic. To mitigate them, we set the relative intensities of the σ and π beams at the ion to a fixed ratio near the "magic" 2:1 ratio which to first order makes the AC Stark shift uniform across all sublevels within a given rotational manifold (more details are discussed in the Methods of [44]). Operating at the magic ratio is important so that turning on and off the beams does not affect the eigenstates of the system and the observed transition frequencies do not depend on beam intensity. Still, the intensity of each beam at the ion position must be actively calibrated during the experiment, typically once every 15-30 seconds, or else drifts in beam pointing or ion position will cause shifts in transition frequencies. With our Raman beams focused to a waist of $\sim$15 μm, we are sensitive to $\lesssim 1$ μm drifts. To perform the required calibration, we swap the ion order, measure the Stark shift imparted separately by each Raman beam on the Ca$^+$ $S_{1/2} \leftrightarrow D_{5/2}$ transition, and feedback to the

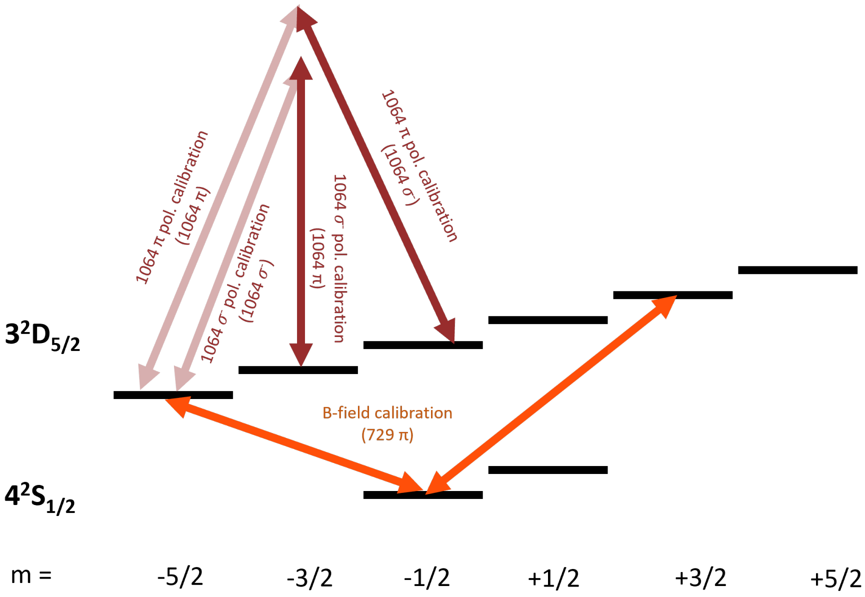

Figure 3.6: An illustration of calibration procedures performed daily for B field and Raman beam polarizations. B-field is determined by the difference in frequency between the $|S_{1/2}, m = -1/2\rangle \leftrightarrow |D_{5/2}, m = -5/2\rangle$ and $|S_{1/2}, m = -1/2\rangle \leftrightarrow |D_{5/2}, m = +3/2\rangle$ transitions. Polarization is optimized for each Raman beam by minimizing the observed Rabi frequency on a transition that requires (unwanted) σ^+ polarization of the beam to be optimized; the beam with unwanted polarization is shown as transparent in the figure.

beam power servo setpoint as needed. Operations that require different Rabi frequencies than would be achieved at the calibration intensities use a uniform scaling factor applied to both Raman beam intensities to maintain the magic intensity ratio.

Our ions are spaced by ~ 3 μm, so a change in ion order (attributed to collision with background gas) can lead to significant transition frequency shifts. Ion order is checked approximately once every 250-500 ms by checking the Stark shift on Ca$^+$ in much the same fashion as intensity stabilization. When the Raman beams are well-aligned to the molecule (in the desired ion order), the Stark shift imparted by the 1064 nm σ beam differs by $\sim$10 kHz depending on the actual ion order, allowing for efficient discrimination with a ~ 100 μs 729 nm carrier pulse.

3.3.6.3 Signature transition contrast

With all of these calibrations and servos deployed, we can measure the signature transition frequencies in various J's by preparing in one or the other signature manifold sublevel, attempting a single motion-adding signature transition sideband, and reading the result via QLS. Some results are shown in Fig. 3.7. We typically measure $85 - 90\%$ contrast for $J = 1$ and 2. The factors limiting contrast are not well-characterized but likely include residual drifts in the signature transition frequency, imperfect population transfer fidelity during quantum-logic readout, and other technical constraints. If only a single probe is used for preparation and/or measurement, SPAM fidelity will be limited to the contrast of a single signature transition probe.

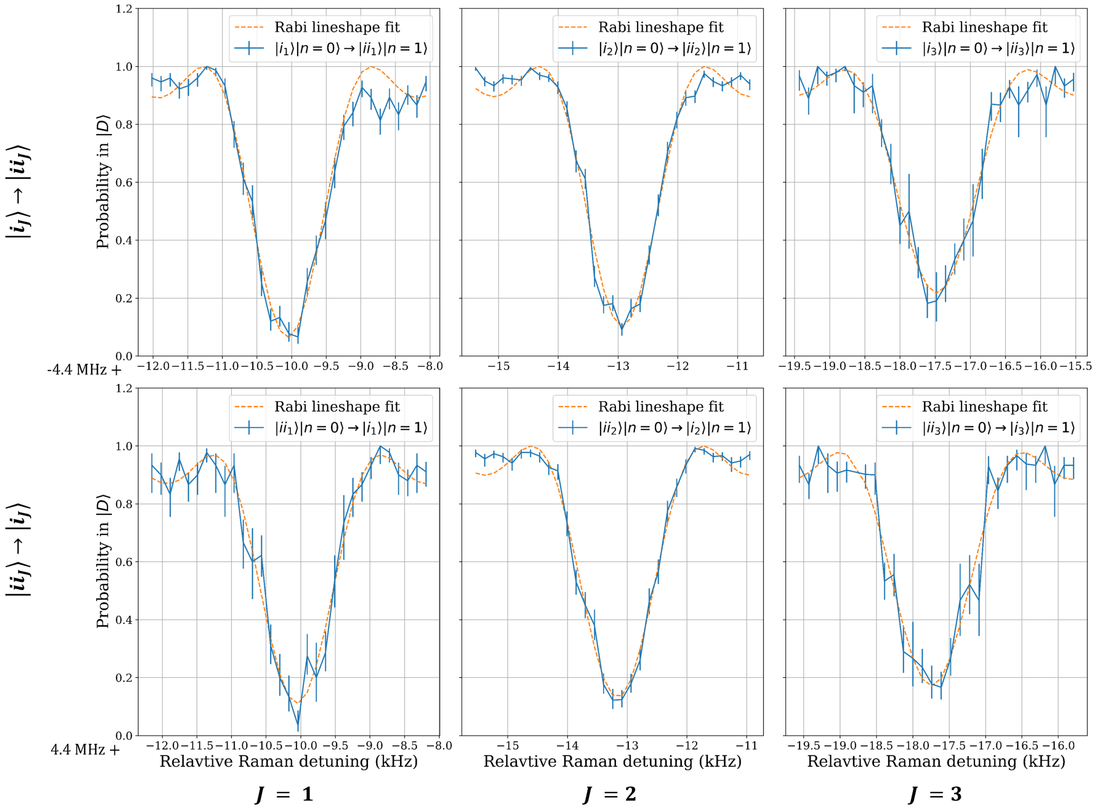

Figure 3.7: Typical frequency scans of the signature transitions for $J = 1 - 3$ for both $|i_J\rangle\,|n=0\rangle \rightarrow |ii_J\rangle\,|n=1\rangle$ and $|ii_J\rangle\,|n=0\rangle \rightarrow |i_J\rangle\,|n=1\rangle$. The molecule is prepared with high confidence using multiple signature transition probes, then the signature transition is driven and detected via QLS as illustrated in Fig. 3.5. The relative Raman detuning is the difference frequency between the two Raman beams $(\omega_\sigma - \omega_\pi)$. The discrepancy from the Rabi lineshape fit near -8.8 kHz in the $|i_1\rangle\,|n=0\rangle \rightarrow |ii_1\rangle\,|n=1\rangle$ scan is due to off-resonant two-step excitation to $|J=1, m=+1/2, \xi=-\rangle\,|n=2\rangle$.

Chapter 4

High-fidelity quantum-state control of CaH^+

Quantum control of molecules is a burgeoning field with applications including precision measurement [16–19], quantum information processing (QIP) [20–23], and fundamental chemistry studies [26, 28]. Techniques for achieving such control include direct laser cooling of molecules [33–36] and formation of molecules in a desired quantum state through association of ultracold atoms [37–39]. The fidelity of molecular state control is approaching a regime relevant for QIP applications [20, 72, 73], with demonstrated single-state preparation, manipulation, and measurement fidelities exceeding 90% [20, 21, 74, 75], and those for a manifold of states above 99% [42, 76, 77]. Expanding high-fidelity quantum control capabilities to a wider variety of molecular species such as molecular ions will unlock molecules' full utility across quantum science applications.

We can consider, for example, a quantum networking application using a molecular ion as a frequency transducer [32] between an atomic ion qubit (for high-fidelity gates) and a telecommunications-band (telecom) photonic qubit, which is well suited for long-distance information transfer in optical fiber. The atom's state information could be mapped to the molecule via quantum logic; the appropriate vibrational transition at a telecom wavelength could then be addressed. If the molecule is within an appropriate cavity, it will emit into the desired mode with high probability for collection [78]. Besides quantum networking, a number of proposals and experiments leverage molecular rotational states as qubits [20, 21, 73, 79], since they can be long-lived and (for polar molecules) possess strong electric dipole interactions between molecules. Precision measurement applications, particularly those attempting to measure weak or uncertain signals, can also benefit from high-fidelity operations.

Thus, demonstrating high-fidelity state preparation and measurement (SPAM) would validate the practicality of molecules in a variety of applications.

In the experiments described in this chapter, we use QLS to control a CaH^+ ion in a cryogenic environment and achieve high SPAM fidelity. We observe rotational state lifetimes of $18 \pm 2(10 \pm 1)$ s for states with $J = 1(2)$, reducing the dominant error mechanism in our system by an order of magnitude over a comparable room-temperature apparatus [44, 47]. Operating in a cryogenic environment dramatically reduces the size of the thermally populated molecular state space, with population found in $J \in \{1, 2, 3\}$ 97% of the time. By adaptively probing the molecule multiple times, detecting the outcome of each probe via a QLS detection protocol, and using a Bayesian probability inference scheme to quantify our confidence in the populated molecular state [80, 81], we demonstrate SPAM in a single quantum state with $< 6 \times 10^{-3}$ infidelity. Our protocol does not require any molecule-specific lasers and our detection scheme is non-destructive. To my knowledge, this result represents the highest such SPAM fidelity of a molecule demonstrated to date and further establishes molecules as a viable QIP platform.

4.1 Experiment protocol

In our experiment, a single signature transition sideband probe has $\sim 85\%$ population transfer efficiency. To achieve $\gtrsim 85\%$ detection fidelity, we attempt multiple signature transition probes. Based on the binary result $R \in \{S, D\}$ (detection of Ca^+ in $|S_{1/2}\rangle$ or $|D_{5/2}\rangle$ after the QLS sequence), the confidence $P(\text{in})$ that the molecules lies within the probed signature manifold is updated according to Bayes' rule [80]. Specifically, given an initial probability $P(\text{in})$ that the molecule occupies the signature manifold and an outcome R of a QLS sequence, the confidence is updated according to:

$$P(\text{in}|R) = \frac{P(R|\text{in})P(\text{in})}{P(\text{in})P(R|\text{in}) + (1 - P(\text{in}))P(R|\text{out})}. \tag{4.1}$$

We empirically estimate the conditional probability $P(S|\text{in}) = 0.85 = 1 - P(D|\text{in})$, corresponding to the observed single-molecular-probe success probability after high-fidelity state preparation; and

$P(S|\text{out}) = 0.009 = 1 - P(D|\text{out})$, corresponding to the purification level of $|D_{5/2}\rangle\,|n=0\rangle$ prior to the molecular probe. More specifically, $P(S|\text{in})$ is determined by the contrast of the fit of the signature transition probes (such as is shown in Fig. 3.7) and P(S|out) by the $|S\rangle$ probability when running a QLS sequence with no probe pulse.[1] A predetermined confidence threshold C_T is selected, and $P(\text{in})$ is initialized to 0.5.

For a detection sequence, probes are repeated until one of the following 3 conditions are met:

- $P(\text{in}) > C_T$ AND the final (successful) probe was on the $|ii_J\rangle\,|n=0\rangle \rightarrow |i_J\rangle\,|n=1\rangle$ transition (in-manifold detection)
- $1 - P(\text{in}) > C_T$ (out-of-manifold detection)
- 25 probes have been attempted

A flowchart representing the experimental sequence is presented in Fig. 4.1. In general, an experimental sequence is composed of "preparation", "experiment", and "measurement" stages. Preparation in $|i_J\rangle$ consists of making an in-manifold detection (possibly including pumping steps if the molecular state is initially unknown) while measurement consists of a detection attempt in the prepared manifold to determine whether or not the molecule still resides there. One or several experiment pulses may be applied between preparation and measurement.[2] A typical experimental run will involve many experimental sequences, with occasional breaks for ion order checks or tracking experiments for servo corrections to stabilize the signature transition frequency.

Preparation may involve many pumping pulses if the initial state is unknown. The "pump within J to $|i_J\rangle$" action consists of multiple rounds of cooling to the motional ground state and then driving directional, motion-adding sidebands on molecular transitions to move molecular population from any initial sublevel to $|i_J\rangle$. Due to molecular selection rules, the $J = 0$ transition cannot be driven

---

[1] Our control system also allows for these values to be updated in real time during an experiment based on certain probe results, though this capability is not implemented for the experiments described in this chapter.

[2] A molecular experiment could take many forms, depending on the application; in principle, this could include driving rotational Zeeman, rotational, vibrational, or even electronic transitions. Our experiment has been thus far confined to investigating rotational Zeeman transitions (via Raman drive) or rotational transitions (via microwave drive, or passively via TR interactions).

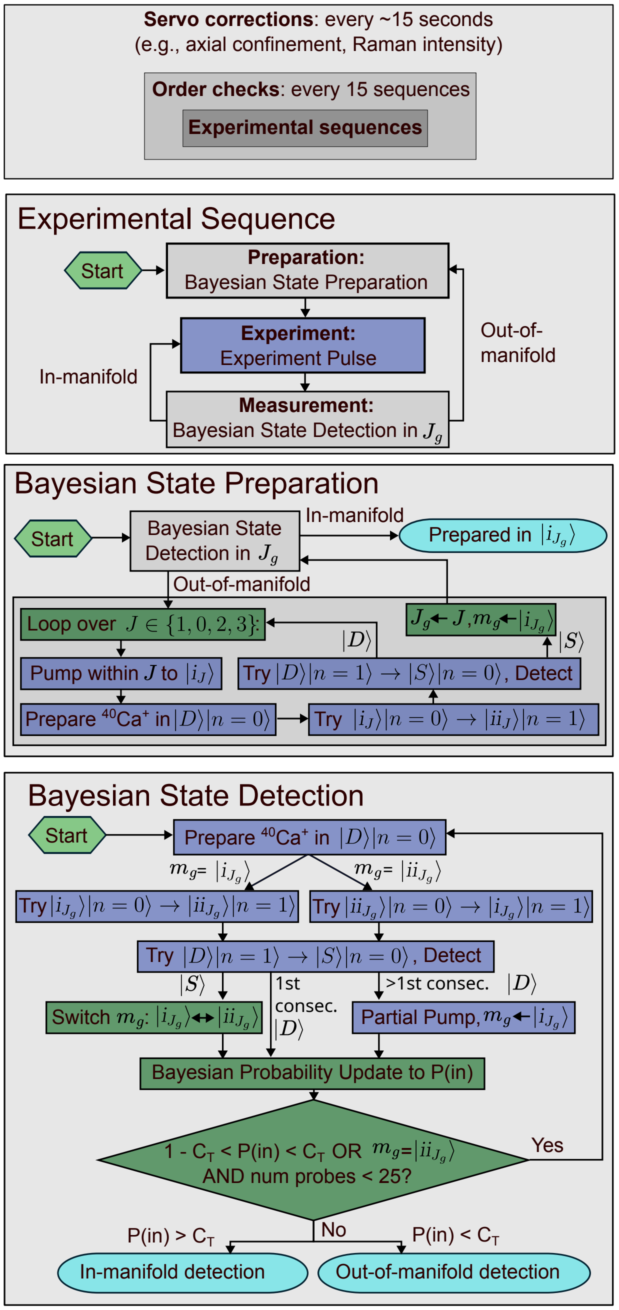

Figure 4.1: Full experimental protocol, including experimental sequence with Bayesian state preparation and detection subprotocols. Here, J_g and m_g are the system's "guess" of the molecular rotational and signature manifold state, respectively: they are initialized to $J_g = 1$ and $m_g = |i_J\rangle$. Grey boxes represent subprotocols expanded elsewhere in the flowchart, dark blue boxes indicate physical actions performed on the ions, green boxes indicate software logic updates, and light blue ovals indicate the endpoint of a subprotocol. The experimental sequence is performed (with occasional breaks for ion order check and servo experiments) until the desired amount of data has been collected.

by our 1064 nm Raman beams. To detect the molecule when it is initially in the $J = 0$ manifold, we deshelve population from $J = 0$ into $|i_1\rangle$ by executing $|J = 0, m = -1/2, \xi = -\rangle \leftrightarrow |i_1\rangle$ and $|J = 0, m = 1/2, \xi = +\rangle \leftrightarrow |ii_1\rangle$ deshelving pulses using a 285 GHz microwave source. A subsequent successful preparation in $J = 1$ will indicate that the molecule was originally in $J = 0$, but prepared in $|i_1\rangle$.

"Partial pump" refers to a pumping pulse on the $|ii_J\rangle \to |i_J\rangle$ transition (and in $J = 1$, a preceding $|iii_1\rangle \equiv |J = 1, m = +1/2, \xi = -\rangle \to |ii_1\rangle$ pumping pulse). This action is necessary due to a small probability to transfer the molecular state without an $|S\rangle$ detection (as well as the possibility of off-resonant excitation from $|ii_1\rangle \to |iii_1\rangle$). Because of partial pumping, the Bayesian detection sequence does not strictly detect one particular initial sublevel, but rather either sublevel in the signature manifold (and for $J = 1$, including $|iii_1\rangle$).

The recorded result of a measurement typically corresponds to the result ("in-manifold" or "out-of-manifold") of its Bayesian state detection sequence. However, in the rare cases where the detection sequence terminates due to hitting 25 probes (and thus with $1 - C_T < \mathrm{P(in)} < C_T$) we threshold measurement results as $\mathrm{P(in)} > 0.5$ and $\mathrm{P(in)} < 0.5$. Note that this "timeout" condition occurs for $\ll 0.1\%$ of measurements and can likely be attributed to ion reorder events and/or mid-measurement rotational manifold transitions.

At the conclusion of state preparation, we would like to ensure that the molecule resides in one particular sublevel ($|i_J\rangle$ for the experiments presented here). To do that, we require the final, successful probe to be in the $|ii_J\rangle \to |i_J\rangle$ before completing an in-manifold detection. This requirement has the added benefit that preparation can be bypassed after an in-manifold measurement, as indicated in the Experimental Sequence panel of Fig. 4.1.

Since we currently do not have a method to drive transitions between rotational manifolds (besides $J = 0 \leftrightarrow 1$), we may be waiting tens of seconds for thermal redistribution to bring the molecule into a particular manifold. To increase total data rate, we typically conduct experiments in multiple manifolds within a single experimental run. If preparation cannot be completed after pumping in one manifold, we cycle through different manifolds until a successful preparation is made.

Here I will present SPAM results for $J = 1$ and 2, which collectively are occupied for $> 80\%$ of the total experimental duty cycle (with shelving out of $J = 0$). Though the lifetime, pumping efficiency, and observed SPAM fidelity are lower for $J = 3$, we still attempt to prepare it if preparation cannot be completed for $J < 3$; information gained from this is included in the BBR environment data presented later in the chapter.

4.2 Results of high-fidelity state control investigations

4.2.1 SPAM

To characterize SPAM fidelity within a given signature manifold, we omit the experiment stage. We define SPAM infidelity as the probability that the molecule is measured to be out of the prepared manifold after preparation. Fig. 4.2 presents the measured SPAM infidelities for the $J = 1$ and 2 signature manifolds as a function of C_T.

Varying C_T is a tradeoff between confidence achieved and number of probes required per detection event. In the absence of other error mechanisms, the measured fidelity is expected to be at or above C_T (black dashed curve); this is true for our data for $C_T \leq 0.997$. For $C_T > 0.997$, other error mechanisms contribute significantly. For the C_T with the lowest infidelity, we observe an infidelity of $(1.39 \pm 0.23) \times 10^{-3}$ for $J = 1$ ($C_T = 0.9997$, with an average of 2.96 probes taking 22.5 ms per measurement) and $(1.81 \pm 0.30) \times 10^{-3}$ for $J = 2$ ($C_T = 0.997$, with an average of 2.37 probes taking 17.3 ms per measurement). Reported uncertainties are statistical and represent one standard deviation.

Despite the reduction in TR due to cryogenic operation, rotational level changes during measurement are the leading error mechanism at high C_T. To quantify the expected error due to rotational state change for a given data point, we compare the average duration of a measurement sequence to the observed rotational manifold lifetime. The average number of probes per measurement ranges from 2.3 to 4.9 across the range of C_T's considered here, the average probe duration is 7.6 (7.3) ms for $J = 1(2)$, and the observed rotational state lifetimes are 18±2 (10±1) s, as detailed

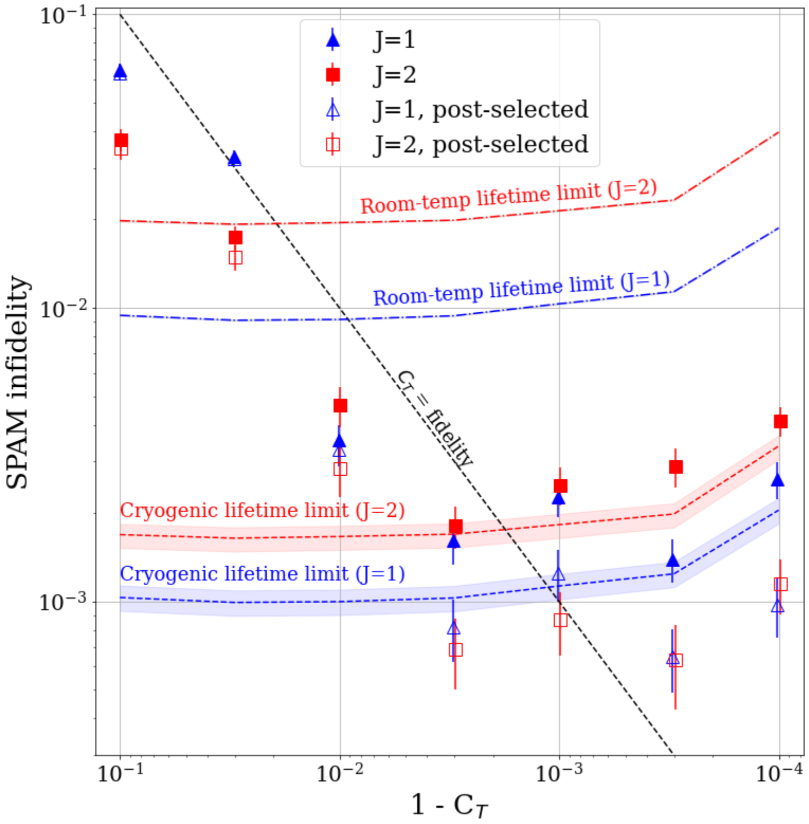

Figure 4.2: Results of SPAM infidelity characterization vs confidence threshold C_T for the $J = 1$ (blue triangles) and $J = 2$ (red squares) signature manifolds. Infidelities are calculated by observing the fraction of measurement sequences that determine the molecule to be out of the prepared manifold immediately after preparation. Post-selected infidelity omits measurements that are followed by preparation in a different rotational level. Error bars denote one Wilson interval. For $C_T \lesssim 0.997$, infidelity tracks $1 - C_T$ (black dashed line). Lifetime-limited infidelity (blue (red) dashed curves for $J = 1(2)$) is calculated by dividing the observed average measurement sequence duration by the observed average lifetime for each data point; the uncertainties, indicated by the shaded backgrounds, are chiefly due to uncertainties in the experimentally-determined lifetimes. As C_T approaches 1, more and more probes are needed for measurement, increasing the likelihood of population loss during measurement. For comparison, we also provide the expected limit in a room-temperature environment (dot-dashed lines) based on theoretical lifetimes.

below. The lifetime-limited fidelities plotted in Fig. 4.2 (colored, dashed curves) are calculated by dividing the average measurement duration by the observed lifetime, representing the fraction of measurements during which a rotational state change is expected to occur. These limits provide an explanation for the increasing infidelities at high C_T (since more probes, and thus more time, are required to achieve the required confidence) and the higher infidelities for the shorter-lived $J = 2$

manifold, compared to $J = 1$, at high C_T.

To quantify contribution from other error mechanisms, we can post-select away measurements that are immediately followed by preparation in a different rotational level. By doing so, we omit instances where a rotational transition has occurred during measurement. The post-selected infidelity is as low as $(6.5 \pm 1.6) \times 10^{-4}$ for $J = 1$ and $(6.3 \pm 2.0) \times 10^{-4}$ for $J = 2$, both for $C_T = 0.9997$. Sources for this residual infidelity may include collisional ion reordering events and fluctuations in the signature transition sideband frequency. Further discussion is provided in Section 4.3.

At 295 K, the theoretical rotational level lifetimes are 2.0512 ± 0.0008 (0.8825 ± 0.0015) s for $J = 1(2)$ where the uncertainty in the theoretical lifetimes originated from the uncertainty in the permanent dipole moment of the molecule [46]. Both theoretical and experimentally measured [47] lifetimes are about an order of magnitude shorter than what is observed in the cryogenic environment, corresponding to an elevated theoretical fidelity limit. These limits are shown by the dot-dashed curves in Fig. 4.2, which are calculated according to the theoretical rotational level lifetimes and observed average measurement durations. From these limits, we infer that a room-temperature system using the same SPAM scheme would be limited to infidelities $\gtrsim 0.01$. Thus, the reduced ambient TR enables improvement of SPAM infidelity by about an order of magnitude.

4.2.2 Shelving out of signature manifold

Since our measurement does not distinguish between states within the signature manifold, the SPAM fidelity results presented thus far cannot be considered to be of a single quantum state. Nevertheless, we expect that our preparation sequence concludes with the molecule in state $|i_J\rangle$ with near-unity probability due to the requirement that preparation ends with a $|ii_J\rangle \to |i_J\rangle$ probe. As proof of the purity of the prepared state and further demonstration of our molecular quantum state control capabilities, we introduce an experimental pulse with variable duration coherently transferring population from the prepared sublevel $|i_1\rangle$ to the out-of-manifold sublevel $|1, -1/2, +\rangle$ via a Raman carrier drive. The resulting Rabi flopping, measured with C_T set to 0.997, is shown in Fig. 4.3. Additional data was taken near the π-time for better statistics; after a π-pulse, population was measured to be in manifold with $(5.6 \pm 1.2) \times 10^{-3}$ probability. We take this number as an upper bound on our single-quantum-state SPAM infidelity, though it includes some contribution from imperfect state transfer.

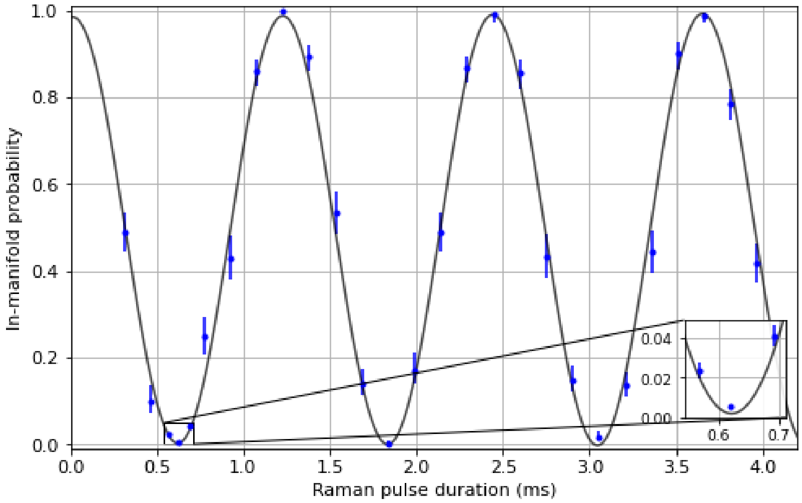

Figure 4.3: : Rabi flopping on $|i_1\rangle \leftrightarrow |1,-1/2,+\rangle$ by a pulse of variable duration that is resonant with the transition and applied between preparation and measurement. The fit is to an exponentially-decaying sinusoidal function.After a π-pulse (620 μs duration), the molecule is measured in manifold with probability $(5.6 \pm 1.2) \times 10^{-3}$. Error bars denote one Wilson interval.

After a π pulse, population was measured to be in manifold with probability $(5.6 \pm 1.2) \times 10^{-3}$. Achieving such high shelving efficiency demonstrates that (a) we can perform high-fidelity, coherent manipulation of the molecular state, (b) we prepare in a single sublevel with high probability, and (c) our measurement protocol reliably detects out-of-manifold as well as in-manifold states. Note that compared to the QLS sequence, which relies on sideband drives for both molecule and atom, the carrier shelving pulse achieves much higher contrast. Nevertheless, we believe the residual population measured in the prepared state after a π pulse is due primarily to imperfect state transfer, e.g., due to differential fiber noise between the Raman beams.

4.2.3 Observations of thermal environment

By continuously attempting to prepare and measure the molecular state for $J \in \{1, 2, 3\}$, we actively track the ion's rotational state occupation and infer rotational level lifetimes. Doing so, we can extract information about the TR environment interacting with the ion, assuming rotational transitions are driven solely by TR [47]. The population fractions, ion lifetimes, and inferred blackbody temperature for each rotational state $J \in \{1, 2, 3\}$ are shown in Table 4.1. These data were obtained by tracking the molecular rotational level for about 1 hour by running SPAM experiments with C_T set to 0.997. Note that the ion was actively deshelved out of $J = 0$ if suspected to reside there. The blackbody radiation (BBR) temperature is inferred from the lifetime assuming an ideal blackbody environment. The inferred blackbody temperatures are significantly hotter than the measured cold stage temperature of 15.8 K. Both the lifetimes and occupation fractions suggest a photon density more consistent with ∼35 K.

Table 4.1: Rotational level tracking over 64 minutes of repeated preparation and measurement attempts with active deshelving out of $J = 0$ states. The lifetime is found by dividing the total time spent within a level by the number of times the molecule was observed to leave the state, and the effective BBR temperature is found by comparing the observed lifetime to theory [47, 82]. Uncertainties in measured lifetimes are statistical, while uncertainties in inferred BBR temperature include both statistical contributions and uncertainty in the molecule's permanent dipole moment [46]. We cannot directly measure population in $J = 0$, but we assume the molecule has transitioned there if it is detected in $J = 1$ only after a $J = 0 \to 1$ deshelving pulse. The unaccounted-for 0.03 population fraction is attributed primarily to occupation of $J > 3$, which we do not attempt to detect.

J	Occupation fraction	Lifetime (s)	BBR temp. (K)
1	0.48	18.1 ± 1.8	$42.3^{+4.3}_{-3.7}$
2	0.36	10.2 ± 0.9	$33.6^{+3.2}_{-2.9}$
3	0.13	5.5 ± 0.6	$30.9^{+4.1}_{-3.6}$

We can also cast state tracking experiments presented in Table 4.1 in terms of a transition rate matrix as shown in Fig. 4.4. Each entry is found by dividing the number of instances the molecule was observed to change states (from initial to final) between consecutive experimental sequences by the total amount of time spent measuring the molecule in the initial state. The molecule is determined to be in an "unknown" final manifold if 14 consecutive preparation attempts (pumping $J = 0 - 3$ and detecting $J = 1 - 3$) do not result in a successful preparation; these are attributed largely to the molecule occupying a manifold of $J > 3$. More than 96% of observed transitions obey

$\Delta J = \pm 1$, suggesting that transitions are dominated by TR-induced transitions (which must obey this selection rule), rather than other transition mechanisms such as collisions or excitation to an excited vibrational or electronic level. The most prominent entry not obeying the selection rule is $J = 2 \rightarrow$ unknown, which is likely due to inefficient pumping of the $J = 3$ manifold such that the molecule makes a second transition before preparation can occur in $J = 3$.

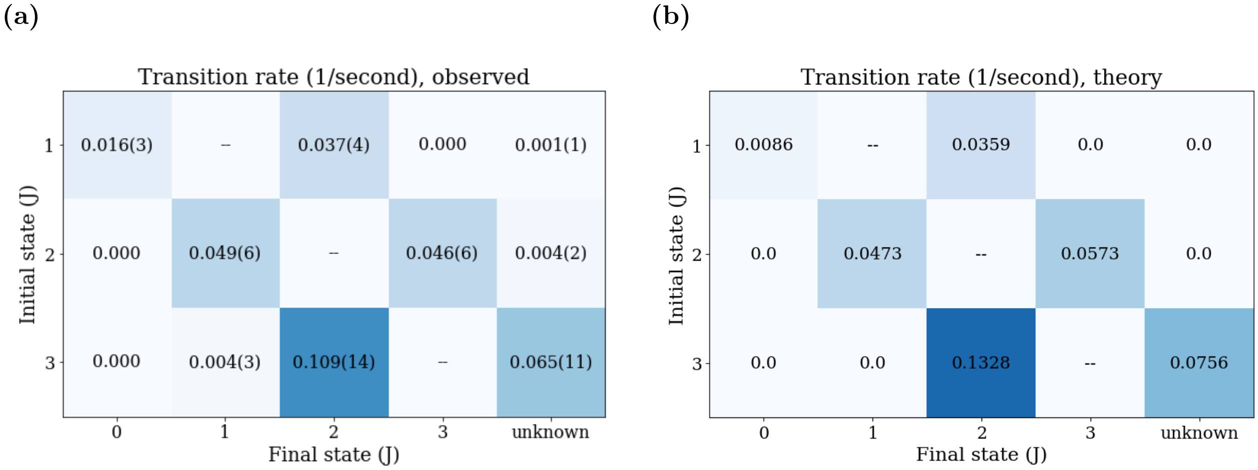

Transition rate (1/second), observed

Initial state (J) \ Final state (J)	0	1	2	3	unknown
1	0.016(3)	–	0.037(4)	0.000	0.001(1)
2	0.000	0.049(6)	–	0.046(6)	0.004(2)
3	0.000	0.004(3)	0.109(14)	–	0.065(11)

Transition rate (1/second), theory

Initial state (J) \ Final state (J)	0	1	2	3	unknown
1	0.0086	--	0.0359	0.0	0.0
2	0.0	0.0473	--	0.0573	0.0
3	0.0	0.0	0.1328	--	0.0756

Figure 4.4: (a) The observed transition rates over 65 minutes of state tracking. Uncertainties are statistical. Changes of $|\Delta J| > 1$ may be attributable to multiple transitions occurring before preparation could be completed, or to transition mechanisms such as collisions that do not obey this selection rule. (b) Theoretical transition rates assuming a 35 K BBR environment.

We also present the calculated transition rate matrix assuming an ideal blackbody environment at 35 K and using the stimulated and spontaneous transition rates calculated from the Einstein coefficients as detailed in Section 2.2. When comparing to the observed values, a general trend emerges in that the lowest frequency transition ($J = 1 \rightarrow 0$) is observed to occur faster than the predicted rate, while transitions at higher frequencies ($J = 2 \leftrightarrow 3$ and $J = 3 \rightarrow$ unknown) are observed to occur slower than the predicted rate; this is also borne out by the J-dependent effective temperature trend seen in Table 4.1. These trends suggest that the environment deviates from ideal blackbody behavior, exhibiting excess or suppressed photon density at certain frequencies.

4.3 SPAM error budget

By post-processing the data accrued for the high-fidelity SPAM results presented in Section 4.2.1, we can extract information about various error mechanisms affecting our SPAM fidelity. Errors due to TR-induced loss are inferred by counting the number of instances in which an out-of-manifold measurement was followed by preparation in a different manifold (i.e., the difference between the raw and post-selected infidelities plotted in Fig. 4.2). Another leading error mechanism arises from the sub-unity confidence threshold. This error occurs when a sufficiently large number of false-negative outcomes leads to an inaccurate out-of-manifold detection. Assuming that the false negative and false positive probabilities used in the Bayesian update are accurate, this error will always be $\leq 1 - C_T$. To quantify more precisely, we estimate sub-unity C_T error as the average confidence $P(\text{in})$ obtained at the conclusion of Bayesian state detection for out-of-manifold measurements. If this estimate exceeds the post-selected infidelity, the contribution from sub-unity C_T is capped at the post-selected infidelity.[3] Any remaining discrepancy between total observed infidelity and the sum of the TR-induced loss and sub-unity C_T contributions is attributed to other mechanisms.

The results of this analysis are displayed in Fig. 4.5. As expected, contribution from sub-unity C_T falls off with increasing C_T. Meanwhile, TR-induced loss errors increase with increasing C_T due to the increased average measurement duration. A plot of the average measurement duration for each experiment condition is shown in Fig. 4.6.

Another possible error mechanism is changes in ion order due to collisions with background gas, which will cause a decrease in detection fidelity due to the change in light shift magnitude for the molecular levels induced by the tightly-focused Raman beams. During SPAM experiments, the ion order is checked and reset as necessary every 15 experimental sequences. We can estimate the infidelity contribution by calculating the fidelity increase when post-selecting away all sets of 15 measurements that are followed by detection of an ion reorder; from this we infer a contribution of $< 2.6 \times 10^{-4}$ for all experiment conditions. This is also consistent with our observed reorder rate

---

[3] Otherwise, total estimated contributions would exceed the total observed infidelity.

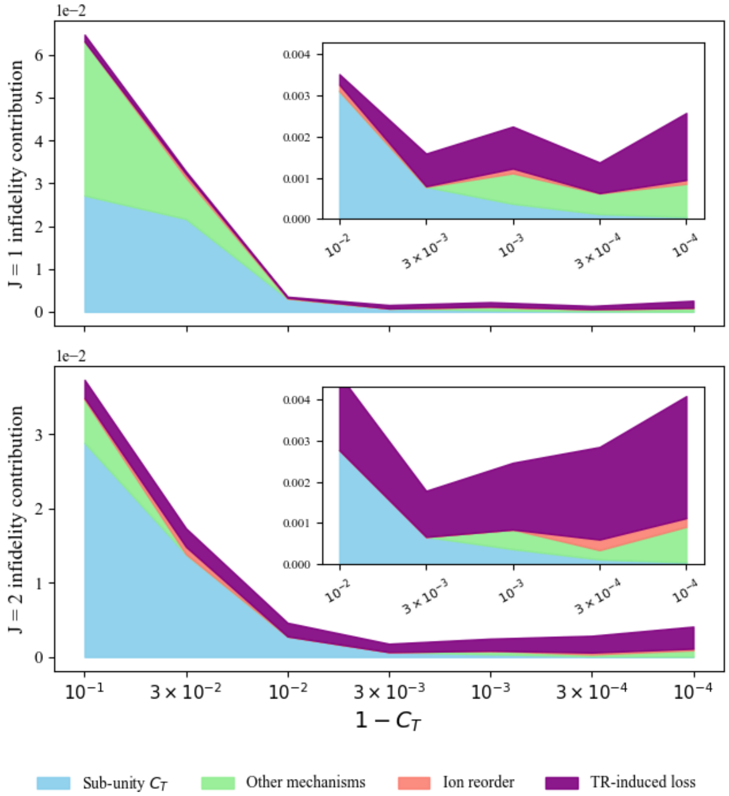

Figure 4.5: Comparison of infidelity mechanism contributions vs C_T. At low C_T, most errors are attributable to the sub-unity threshold, while at high C_T, TR-induced loss dominates.

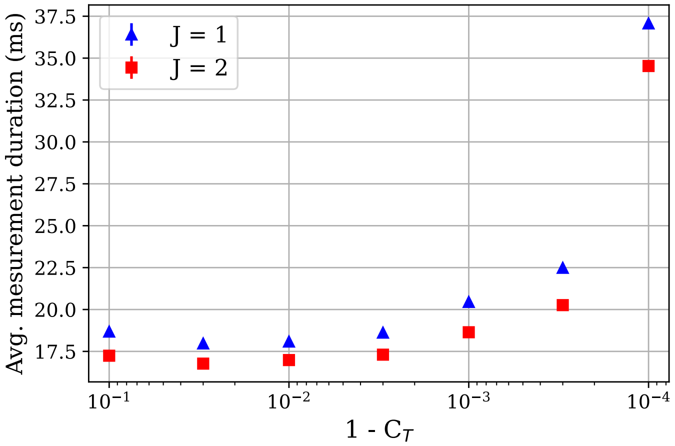

Figure 4.6: Average measurement duration vs C_T. As C_T increases above 0.97, more probes are required to cross threshold, increasing the average measurement duration. Statistical error bars are smaller than the plotted markers.

(∼1 reorder/3 minutes from an independent measurement) and the decrease in detection fidelity we observe when purposefully operating in the "wrong" order.

Finally, we attribute remaining errors to signature transition frequency fluctuations, which can increase the false negative probability $P(D|\text{in})$. In this case, $P(\text{in})$ will not be faithfully estimated by application of Eq. 4.1. Though we interleave servos of several parameters whose drifts can cause shifts in the signature transition sideband frequency—such as axial OOP motional mode frequency, Raman beam intensities, and micromotion—some drift still occurs. Figure 4.7 shows the post-selected infidelity of each SPAM experiment run with $C_T \geq 0.997$ as a function of the (post-processed) $P(\text{S}|\text{in})$ during measurement throughout the run; the outlier is one (of four) runs at $J = 1, C_T = 0.999$ and helps to explain the relatively high contribution from "other mechanisms" for this data point as shown in Fig. 4.5. Such errors could be mitigated by more frequent calibration of the signature transition sideband pulse parameters, empirically updating the value of $P(S|\text{in})$ used in the Bayesian calculation in real time, and technical improvements to reduce drifts.

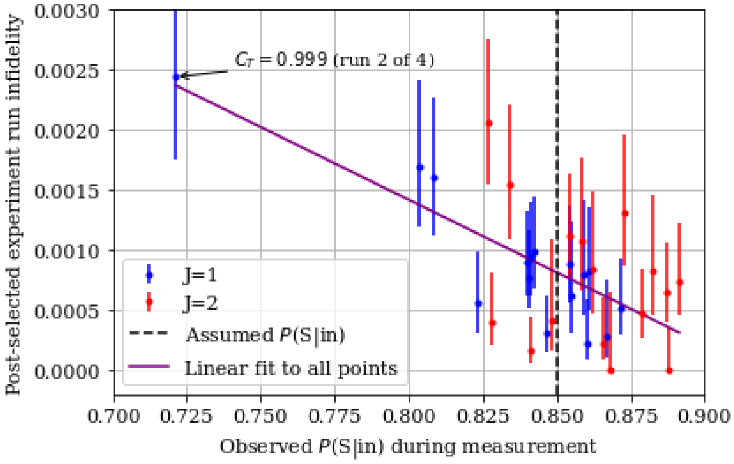

Figure 4.7: Effect of signature transition drift on infidelity. Each point represents a measurement run with $C_T \geq 0.997$. The four runs per C_T (per J) are all of the data used for determining the SPAM infidelity plotted in Fig. 4.2. Observed $P(\text{S}|\text{in})$ considers every signature transition probe during every measurement within the run. The linear fit considers all points regardless of J or C_T. The annotated outlier represents one (out of four) runs with $J = 1$, $C_T = 0.999$. Calibration experiments, e.g., of the signature transition frequency, were sometimes performed between runs.

4.4 State lifetime limitations

We would like to know why the temperatures inferred from lifetimes (as shown in Table 4.1) are significantly higher than the measured inner shield temperature of 15.8 K. We investigated several possible causes:

- **Trap electrode temperature**: Under normal operating conditions, about 0.5-1 W of RF power is dissipated on the cold stage. Though expected thermal gradients across the diamond trap chip are minimal, localized defects or poor thermal contact could raise electrode temperatures, thus increasing the TR experienced by the ion. However, no significant change in lifetime was observed when operating with an RF power increased by a factor of 1.6 compared to normal operating conditions, ruling out electrode heating as a dominant factor.

- **Background gas collisions**: Collisions with background gas can cause transitions between rotational levels. Prior experiments (in a different, room-temperature apparatus [47]) set bounds on the contribution of background pressure to transition rates. Scaling to our experimental conditions [58] by accounting for differences in reorder barrier (inferred from motional mode structure) and collision energy (due to the decreased ambient temperature), we expect a contribution of $< 1/200$ s, ruling out background gas collisions as a dominant factor.

- **Thermal radiation leakage**: TR from warm surfaces can reach the ion via windows and apertures. The vast majority of potential leakage by physical area is the BK7 windows. Using an uncoated BK7 window and the ion or a thermal power head, we measured an absorption coefficient of ~ 5.8 cm^{-1} at 285 GHz, meaning that our 3 mm-thick BK7 windows attenuate by $\sim 80\%$. Though we do not have the technical ability to measure at higher frequencies ($J = 1, 2,$ and 3 lifetimes are primarily affected by 570-1140 GHz radiation), attenuation at these frequencies is expected to be significantly greater [59]. Using Eq. 2.17 and assuming unity, room-temperature transmission through the fused silica window and apertures, we conclude that leaked radiation may contribute to, but does not explain the majority of, the observed lifetime discrepancy. The only caveat would be if the RAM tiles are not having the expected attenuation effect.

- **Geometrical effects**: Trap electrode separation (0.5 mm) is on the order of the wavelength of relevant radiation (0.4-1.1 mm for transitions affecting the lifetimes of $J = 1$ and 2), implying that near-field effects may shape the local TR spectrum. Similar observed discrepancies in other systems have been attributed to this effect [47, 83]; it may be a contributor to the observed reduced lifetimes.

4.5 Data rate

The data rate in our experiments is influenced by many factors. These include:

- **Time spent in J.** We currently do not have the ability to drive rotational state-changing pulses (besides $J = 0 \leftrightarrow 1$), so our duty cycle for performing an experiment within a given rotational manifold is limited by the fraction of time spent in that manifold due to stochastic, TR-induced transitions—see Table 4.1.

- **Pumping efficiency.** Even if molecular population is in the correct J, we cannot perform experiments if we have not moved the population to the signature manifold. For $J = 1$ and 2, which have long lifetimes and low sublevel multiplicity (therefore requiring less pumping pulses), this effect is small. However, at higher J, this can be a significant factor.

- **Time spent in servos.** For the experiments described here, approximately 40% of the duty cycle is spent performing servo corrections. The majority of that time is spent servoing the quantum-logic motional mode frequency.

- **Detection duration.** This depends on both the number of probes required to cross threshold and the duration of a single probe. The number of probes required depends on the false positive and negative probabilities, $P(S|\mathrm{out})$ and $P(D|\mathrm{in})$, as well as C_T (see Fig. 4.6).

The duration of a single probe (currently ~ 7.5 ms) is dominated by cooling—only about 10% of the time per probe is spent on the probe pulse itself.

- **Experiment pulse duration and subsequent population recovery.** This contribution to sequence duration always includes the duration of the experiment pulse itself. If the experiment pulse did in fact transfer the population out of the signature manifold, this will also include the operation required to undo the experiment pulse and the preparation sequence(s) applied to verify that the molecule has been returned to the signature manifold. This factor is not at play during the SPAM experiments since there is no experiment pulse, but it is, e.g., in the carrier Rabi flop experiments.

The data rates achieved for various experimental conditions are provided in Table 4.2. As expected, data rate is decreased for $J = 3$ compared to $J = 1$ and 2 (because of the thermal distribution of population), higher C_T (because of the increase in required number of probes per detection), and an experiment that includes an experiment stage (since time is spent applying the experiment pulse and recovering the population after it has been successfully driven out of the signature manifold). Straightforward strategies to increase data rate for future experiments include introducing additional tools for deterministic rotational state preparation, increasing the efficiency of cooling throughout the experiment, and reducing parameter drifts such that less time needs to be spent running servo experiments.

Table 4.2: Data rate (experimental sequences/second) for various experimental conditions. The uncertainties are estimated from the spread of values obtained during separate experimental runs. "SPAM" indicates a SPAM infidelity experiment (that is, no experimental pulse), while "carrier Rabi flop" experiments involve an on-resonance time scan (e.g., an experimental run collecting data for Fig. 4.3).

J	SPAM, $C_T = 0.997$	SPAM, $C_T = 0.9999$	Carrier Rabi flop, $C_T = 0.997$
1	12.1(2.9)	6.5(1.0)	2.4(0.6)
2	11.1(2.7)	6.5(1.1)	2.6(0.6)
3	3.8(1.0)	1.5(0.5)	–

Chapter 5

A molecular beam source for molecular ion loading

The experiments described so far in this thesis are performed with CaH^+. In this case, the "base" ion (Ca^+) is loaded by ablation, and CaH^+ is subsequently formed via reaction with background H_2, which is desorbed from cryogenic surfaces when the system temperature is increased. However, CaH^+ is a special case. Ablation is not a generalizable loading technique (though we can load Al^+ from our ablation target alloy.[1]) Introduction of H_2 background gas via heating is also a unique scenario, since almost all other particles will not be gaseous near cryogenic temperatures. Thus, in order to trap and study a broader class of molecules, a different procedure is needed.

To achieve a general loading protocol, we use a supersonic molecular beam, which can deliver intense, directed bursts of gas to our ion trap. This in turn can be used to form trapped molecular ions, for example by photoionization and/or reaction. The remainder of this chapter describes the design, testing, and integration of such a molecular beam machine for the cryogenic molecular ion trapping experiment.

5.1 Molecular beam fundamentals

Generally speaking, a molecular (or atomic) beam consists of a directional flow of gas within an experimental vacuum apparatus. It is typically produced by allowing gas to expand from a high-pressure *reservoir* into vacuum through a small aperture (the *nozzle*). In vacuum, at least one additional aperture is included to define the propagation direction, and a pumping system removes

---

[1] We could in principle install several different metal-based ablation targets if we desired to load a variety of metal-based ions.

excess gas[2] from the region of vacuum between the apertures (the *differential pumping* volume). Molecular beams may be continuous or, if there is means to rapidly open and close the nozzle, pulsed. Continuous beams are typically effusive (gas particles exit the nozzle due to random thermal motion), but a pulsed beam may operate in the supersonic regime.

The kinematics of molecular flow are determined by collisions, either between the individual gas molecules or between molecules and surrounding surfaces. A molecular beam enters the supersonic regime when the mean free path λ_0 (the average distance traveled by a molecule before colliding with another molecule) in the reservoir is much less than the nozzle diameter d_0. A couple of unique properties of a supersonic beam emerge [85, 86]:

- **Cold translational and internal temperature**: Isentropic expansion from a high to a low pressure environment results in a decrease in the molecular beam's translational and internal temperatures [87]. The reduction factor depends on details such as gas species and reservoir pressure (P_{res}), but final temperatures will often lie between 1 - 10 K. This corresponds to a fractional longitudinal velocity spread $\frac{\Delta v}{v}$ of $\lesssim 0.1$ [85], where v is the average longitudinal velocity and Δv is the absolute velocity spread.

- **High average speed**: Just because it's cold, doesn't make it slow: because molecules that exit the valve have preferentially undergone collisions from behind, v will be higher than for a Maxwell-Boltzmann speed distribution at the reservoir temperature (T_{res}). The average speed of a molecule in a supersonic beam is $v_{\text{supersonic}} \approx \sqrt{\frac{\gamma k_B T_{\text{res}}}{(\gamma-1)m}}$ [88], where γ is the ratio of specific heats (C_P/C_V) and m is the molecular mass. For a diatomic molecule ($\gamma = 7/5$), this is ~1.7x faster than the average of a Maxwell-Boltzmann distribution.

When the valve is pulsed, gas exits within a spherical wave; aperture(s) allow for differential pumping and define the beam axis. However, using simple holes as apertures for a high-density supersonic molecular beam is problematic. If even a small percentage of molecules in the beam is reflected from the inner diameter of the hole, thus causing increased internal collisions with the

---

[2] About 10^{16} particles/pulse are released from our valve [84].

remainder of the beam, the characteristic features of the beam such as low temperature and high density will be lost. To avoid this phenomenon, sometimes referred to as beam interference, a specially-shaped aperture known as a skimmer must be used to minimize the number of collisions between redirected molecules and the central portion of the beam. The main features of a skimmer are thin walls ($\lesssim 10\ \mu$m at the orifice) and a curved shape, as shown in Fig. 5.1b. For some computational models of beam transmission through a skimmer, see Ref. [89].

Sufficient vacuum pumping speed in the differential pumping volume is required to (a) reduce the background pressure below $\lesssim 10^{-3}$ torr before each subsequent pulse of the molecular beam to avoid deleterious collisions with residual background gas [85] and (b) pump molecules much faster than they can effusively leak through the skimmer to the experimental chamber, keeping the gas load tolerably small. A second skimmer plus differential pumping stage is often employed to better meet this second requirement.

Our experiment employs a piezoelectric (PZT) valve, commercially available from MassSpecpecD and pictured in Fig. 5.1a, to generate a supersonic molecular beam. A conical nozzle ($d_0 = 150\ \mu$m) is sealed via a control voltage (∼200 V) applied to a piezo-controlled cantilever. By manipulation of the control voltage, the valve can generate gas pulses as short as $\sim 10\ \mu$s with variable repetition rates up to 5 kHz. We find an optimal P_{res} for, e.g., a pure N_2 beam to be ∼3 bar (in this regime, the condition for supersonic expansion is easily satisfied: $\lambda_0 = \frac{k_B T_{\text{res}}}{\sqrt{2}\pi r_{\mathrm{N}_2}^2 P_{\text{res}}} \approx 22$ nm $\ll d_0$, where r_{N_2} is the bond length of N_2). We employ 2 skimmers, commercially available from Molecular Beam Dynamics, and pump each differential pumping region with a dedicated turbomolecular (turbo) pump.

In our experiment, the ultimate figure of merit for the molecular beam is the density of molecules in the trapping region. The Amsterdam valve has measured beam densities of $\sim 5 \times 10^{21}$ particles/s/steradian [84, 90] when measured before any apertures. Meanwhile, we conservatively estimate loss in density from each skimmer as 50-90% (though it can heavily depend upon factors such as beam density and skimmer diameter, see [89]). Under these assumptions, considering the valve-to-trap distance in our system of 50 cm, $v_{\text{supersonic},N_2} \approx 780$ m/s, and a measured fractional

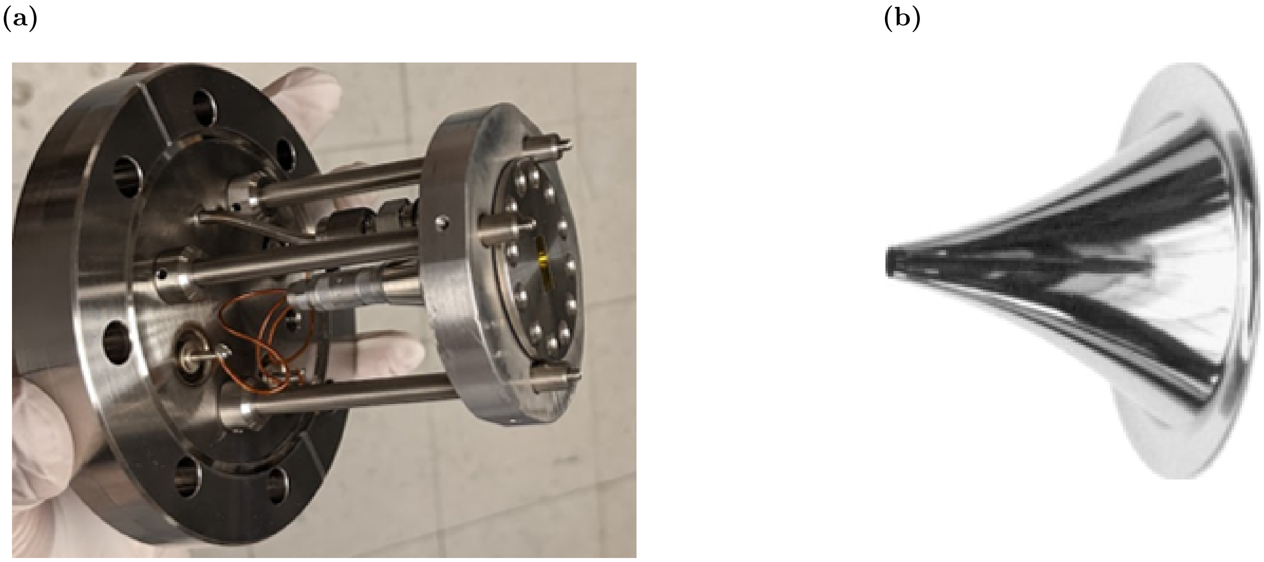

Figure 5.1: Images of two specialized hardware components of our molecular beam machine. (a) The PZT valve as employed in our experiment, with mechanical, electrical, and gas connections to a vacuum flange. (b) A skimmer; two such skimmers, albeit with different diameters, are employed in our experiment. The valve and skimmers are both commercially available.

velocity spread of $\sim$0.1, we can make an order-of-magnitude estimate of the expected peak molecule density at the trap: 2×10^{11} particles/cm^3. This is an equivalent density to a pressure of 8×10^{-4} Pa of thermal gas at room temperature.

5.2 Molecular beam testing

We initially added our molecular beam directly to our ion trap chamber with no prior testing and attempted to observe CaH$^+$ formation. However, this proved to be an ineffective way to confirm the molecular beam alignment to the trap. We had not yet gone cryogenic at that time, and the rate of CaH$^+$ formation from background gas overwhelmed any signal we may have seen directly. Besides, our group had little technical experience with molecular beams, so we were not confident in our beam design or in estimating the expected particle density in the trapping region.

We therefore performed a series of tests with our molecular beam in a separate, test assembly to optimize the valve parameters (P_{res}, valve control pulse duration) and orifice parameters (valve-to-skimmer distance, skimmer alignment, additional apertures). For preliminary testing, we ionized either H_2 or N_2 via EII with an electron source near the ionization region; in later testing, we ionized N_2 with a resonant multi-photon ionization (REMPI) scheme, described further in Section 5.3. In all cases, we ionized between two plates held at a differential voltage, which accelerated ions perpendicularly from the beam's longitudinal direction towards a charged-particle detector. A schematic of the molecular beam testing apparatus can be seen in Fig. 5.2a.

We reached a number of useful conclusions during these tests, which I will summarize here:

- **Valve parameters.** For both H_2 and N_2, the optimal valve parameters needed to achieve high maximum density are $P_{\mathrm{res}} \approx 3$ bar and a control pulse duration of 12 μs. We attribute the reduction in signal at higher P_{res} or pulse duration to beam interference. See Fig. 5.3a for illustration.

- **First (fixed) skimmer.** We found that including this skimmer, as opposed to only having the one (translatable) skimmer, improved total transmission through the system, likely reducing beam interference effects due to reflections from chamber walls at the second skimmer. It also helped with differential vacuum pumping to reduce the gas load to the ionization (or ion trap) chamber. Increasing the valve-to-first skimmer distance yielded an increase in transmission, though with diminishing returns (see Figure 5.3b); the final distance of 6.5 cm was a compromise between beam density and system compactness. All tests were run with a fixed skimmer diameter of 3.0 mm. For more thorough investigations of beam density as a function of valve-to-skimmer distance, see, e.g., Ref. [86].

- **Second (translatable) skimmer.** For this skimmer, we tried skimmer diameters of 0.6, 1.0 and 1.5 mm. We found that reducing the skimmer diameter to 0.6 mm had little impact on the final beam density and minimized the gas load to the ionization (or ion trap) chamber. Figure 5.3c shows how the signal varies with translational (mis)alignment of the skimmer. The results suggest that alignment to within approximately one skimmer diameter is sufficient to maximize the count rate.

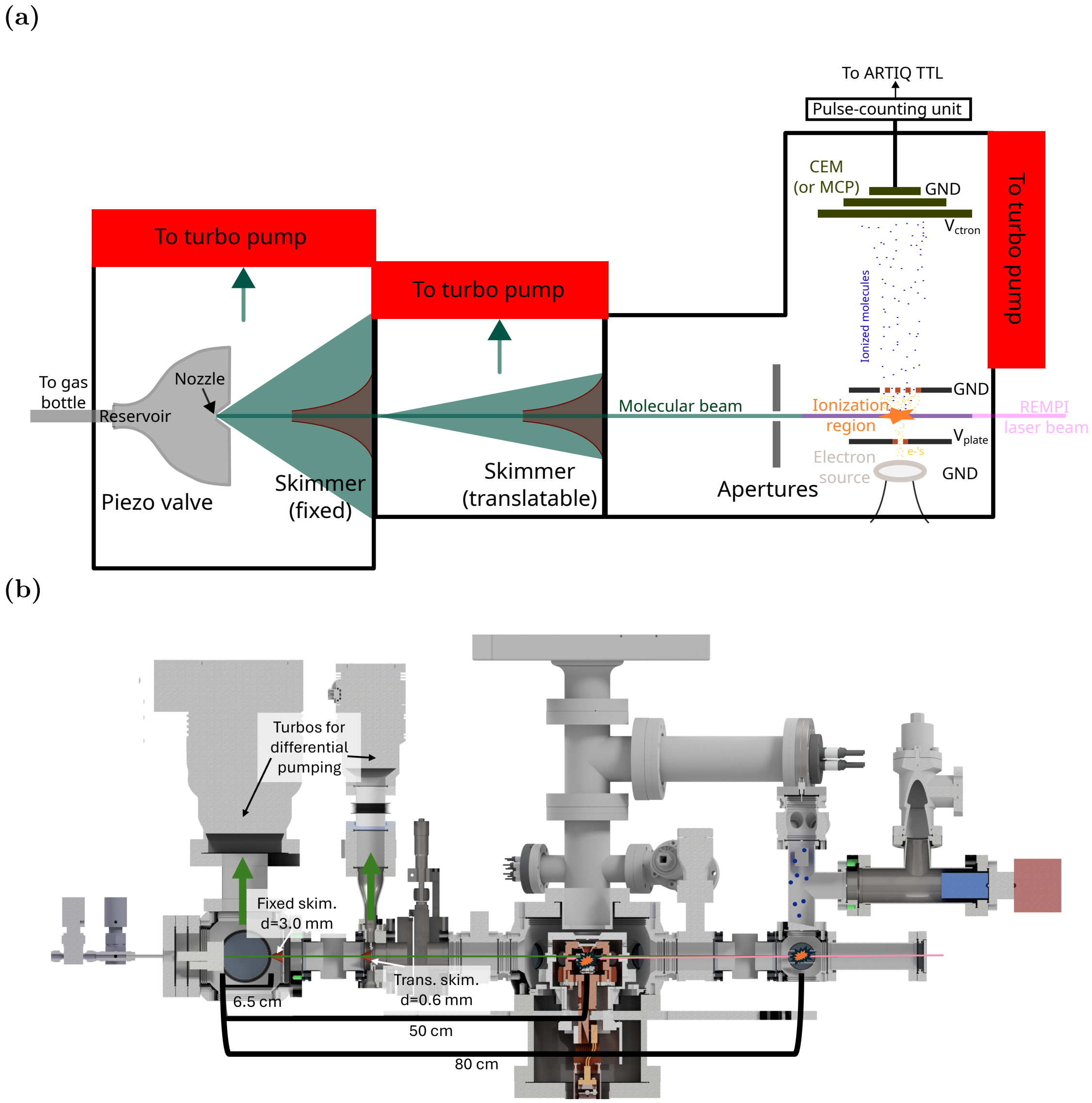

Figure 5.2: **(a) A schematic detailing the basic operation of our molecular beam test assembly.** A piezo valve is pulsed for ∼12 μs. The resultant gas pulse passes through 2 skimmers, the second of which can be independently translated for alignment. Apertures after the skimmers were used to mimic the apertures in the cryo stages and endcap. The molecules are ionized between two parallel plates, either via an electron source or a REMPI laser (see Section **??** for more details). The lower plate is held at a positive voltage to accelerate ions upward towards the charged particle detector and electrons upward into the ionization region. Apertures in both plates are covered with a conductive mesh. The front of the detector is negatively biased to pull in ions (and to provide the differential voltage necessary for signal amplification within the detector). The output of the detector is sent to a pulse-counting unit; ideally, one TTL pulse is sent to the ARTIQ control system for each ion entering the detector. **(b) A CAD model of the final molecular beam configuration integrated with the ion trap chamber.** The detection portion of the beam test assembly is installed after the ion trap chamber to verify molecular beam alignment. Axial optical access allows for an alignment laser to be sent through the entire system to the valve nozzle; it is also used to deliver REMPI light to the trapping region.

- **Apertures after skimmers.** We placed apertures after the skimmers to simulate the various cryo shield and trap features, the smallest of which is a 300 μm-aperture in the endcap. The situations are not identical, since in the actual apparatus the smallest apertures are cryogenically sticky, thus limiting internal reflections; also, the 300-μm aperture in the endcap is roughly skimmer shaped. Nevertheless, we saw no significant reduction in inferred transmission density through test apertures as small as 400 μm in diameter.

- **Charged particle detector.** We initially used a multi-channel plate (MCP) for measuring the signal in our detection chamber.[3] However, we eventually switched to a Channeltron single-channel electron multiplier (CEM) because it is cheaper and more compact. The CEM provides a sufficient signal for our purposes with only a small (∼2x) hit in signal-to-noise ratio compared to the MCP. All of the measurements shown in Section 5.3 are taken via the CEM. The signal amplitude is sensitive to CEM bias voltage (V_{ctron}) and to the threshold of the discriminator to which the CEM signal is sent; these are experimentally optimized for collection efficiency. The acceleration voltage V_{plate} in the ionization region is also experimentally optimized. Typical values are $V_{\text{ctron}} = -1900$ V and $V_{\text{plate}} = 35$ V.

5.3 Ionizing from a molecular beam

Ionization of the neutral molecules within the supersonic beam is required for ion formation and trapping (except in the case of reaction with an already-trapped base ion). Two techniques for doing this are electron impact ionization (EII), whereby collision with an energetic electron removes a previously-bound electron; and photoionization (PI), whereby the molecule absorbs photons until it gains enough energy to lose an electron.

EII is an appealing option because it is broadly applicable to nearly any molecule, with typical cross-section peaks near 70 eV [91].[4] In our test assembly, a commercial electron source is positioned

---

[3] Thank you to the Lewandowski group at JILA for allowing us to borrow your MCP and for sharing your molecular beam expertise!

[4] Implementing an EII electron source is also a cheap and simple option compared to a PI laser system.

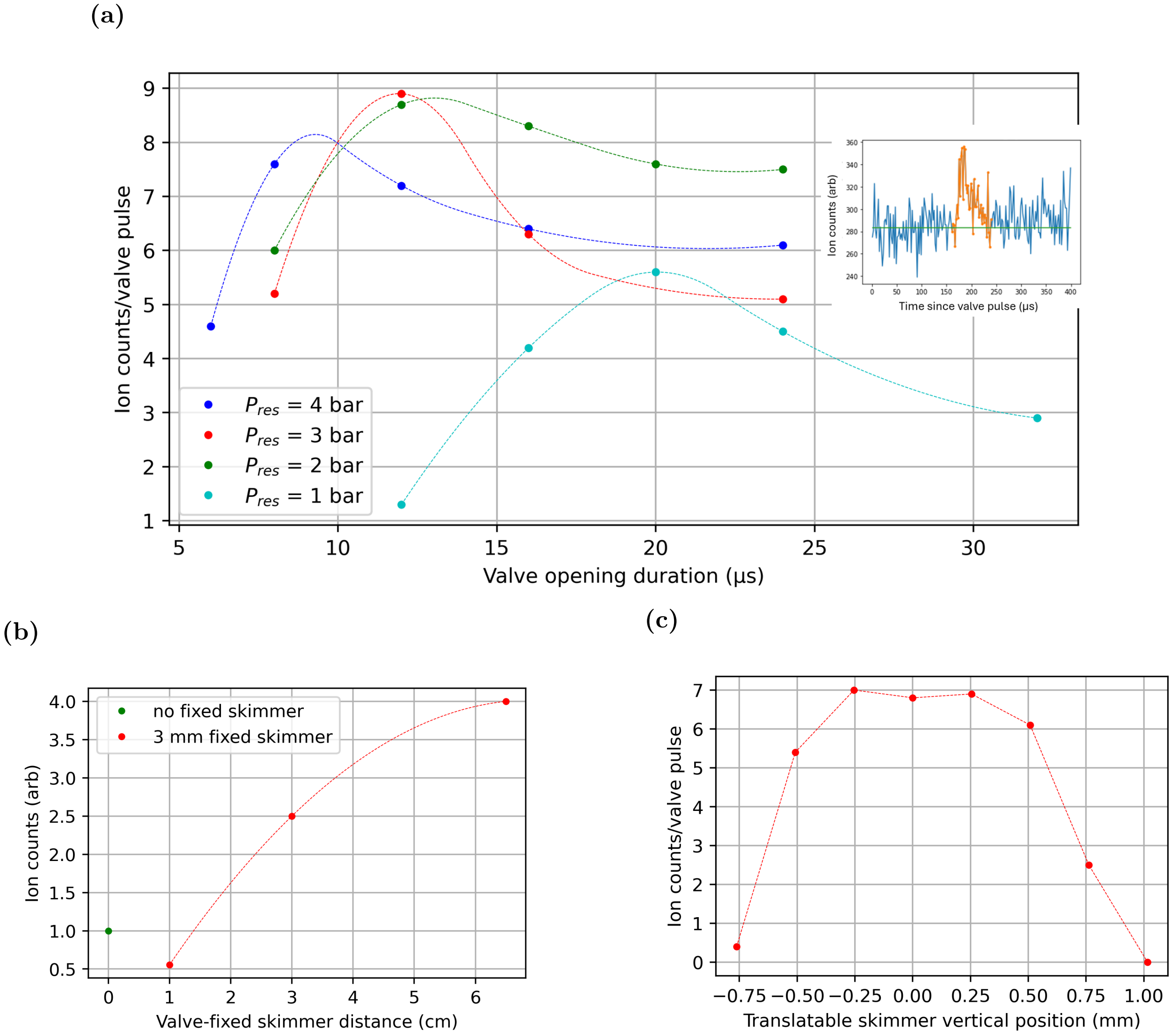

Figure 5.3: Select examples of molecular beam optimization. Data is background-subtracted and integrated over the observed duration of the molecular beam at the detection region (50-200 μs, depending on the gas species and valve-to-detection chamber distance). For each case, the configuration chosen for operation corresponds to the highest plotted point. All curves are included only as guides to the eye. **(a) Piezo valve opening time and backing pressure.** Legend entry indicates pressure of H_2 gas in the reservoir; data were qualitatively similar for N_2. Valve opening duration refers to applied voltage pulse. Curves were taken in the test assembly with the final skimmer configuration and after a 400 μm aperture; ionization was EII. Inset shows an example of the detection signal. Signal above the average background before the pulse (green line) is integrated over the molecular beam duration (orange points). The high background is characteristic of EII in our test assembly. **(b) Valve-fixed skimmer distance.** Data were taken with a beam of H_2 in the test assembly after a 3 mm aperture; ionization was EII. Vacuum was broken between each measurement; the configurations were normalized by comparing to the count rate with a controlled leaked background pressure. **(c) Translatable skimmer alignment.** Data were taken with a beam of N_2 passing through the ion trap chamber; ionization was REMPI. The horizontal skimmer position was set near its optimal value, and the REMPI beam was aligned for each skimmer position.

underneath the ionization region and the electrons are accelerated upwards to cross the molecular beam (see Fig. 5.2a). At our actual ion trap, we have installed an electron source inside of a metal housing attached to the endcap (the one which the beam passes through before reaching the trap, pictured in Fig. 2.5) with the goal of ionizing from the molecular beam while minimizing stray electrons reaching the trap surfaces and causing detrimental charging. This source was successfully used to form ${N_2}^+$ molecules from leaked N_2 during early testing at room temperature.

There are several potential drawbacks to using EII. One is that the large number of generated electrons creates a substantial risk for charging of surfaces—of particular concern in a cryogenic environment, where charges tend to get "stuck" on dielectric surfaces and linger for minutes or hours. A second is that EII is fairly indiscriminate to what particles it will ionize. In the future, we will likely want to send in a seeded beam (see Section 5.4) but selectively load the the molecule of interest rather than the seed. An electron source also requires a high current draw and generates substantial thermal load during operation. Finally, the electron source installed near the trap failed for unknown reasons while attempting to operate cryogenically, so we have been unable to test it in such an environment. For all of these reasons, we have turned to PI loading in our chamber.

Efficient PI of a molecule typically requires tuning a laser or lasers to a specific resonance frequency, exciting a molecule's electron in steps until it finally is excited to the continuum—this is known as resonant multi-photon ionization (REMPI). Virtually any molecule has one or more efficient REMPI paths. Typically, the biggest technical overhead associated with REMPI is generating the appropriate wavelength(s) for the molecular species in question at sufficiently high intensity. We have chosen a tunable dye laser for this purpose—a LiopTec LiopStar, pumped with a Quantel 450 Nd:YAG. The YAG has a pulse repetition rate of up to 20 Hz, outputs up to 450 mJ, 10 ns pulses at 1064 nm, and comes with frequency conversion modules to easily switch between desired harmonics. Coarse wavelength tunability of the dye laser system comes from the freedom of the choice of dye, pump harmonic, and frequency-conversion crystal, while fine tuning comes from adjusting the angle of a diffraction grating within the dye laser cavity. With this system, we can achieve $\gtrsim 1$ mJ pulse energies at 20 Hz across a nearly continuous spectrum from 200-5,000 nm. This will allow us to switch to loading different molecular species without needing a new laser. Note that, in lieu of obtaining multiple dye laser systems, we will select REMPI schemes that do not require multiple colors.

We have demonstrated REMPI of N_2. To do this, we use 237 nm light for a 2+1 REMPI scheme [92, 93]. This drives a 2-photon resonant transition from the electronic and vibrational ground state to an electronically and vibrationally excited state ($X^1\Sigma_g^+(v=0) \rightarrow a^1\Pi_g(v=10)$), with a third photon providing just enough energy for ionization; see [94] for the complete N_2 level structure. While resonant excitation to a lower vibrational level would have a higher FCF and correspondingly higher Rabi frequency, $X^1\Sigma_g^+(v=0) \rightarrow a^1\Pi_g(v=10)$ is the lowest-energy resonant excitation that allows the final ionization step to be of a single, same-color photon, i.e. 2+1 REMPI. Note that the laser source is sufficiently narrow to distinguish different initial and final rotational states of the resonant transition. In our molecular beam test assembly, we can use the piezo valve either as a leak valve (by sending in high-frequency, low-dose pulses) or to generate a supersonic beam (in which case it must be timed with the dye laser pulse).

When introducing N_2 and firing the REMPI laser into the test assembly, we observe a time-of-flight (TOF) spectrum of ions on the CEM (shown in Fig. 5.4a). Even with the REMPI laser far from resonance, some counts can be observed, which are attributed to photoelectrons produced by stray UV photons hitting surfaces such as windows. In fact, we retracted the windows away from the ionization region (from 3.5 cm to 16.0 cm) to reduce this effect. The REMPI'd ions arrive in a narrow TOF region at the CEM. Laser alignment, extraction voltage, and CEM bias are all optimized on this signal.

To observe the REMPI spectrum (displayed in Fig. 5.4b), the wavelength is scanned with the internal dye laser grating; excess counts within the REMPI TOF window are averaged over 50-100 attempts at each point. Laser power is reduced as necessary such that the CEM detector is not saturated at any wavelength in the scan. Peaks in the spectrum are assigned to particular initial and final rotational transitions by comparing to published experimental and theoretical data [92, 93], with which our data is consistent. Transition labels P, Q, R, and S correspond to transitions of $\Delta J=$

-1, 0, 1, and 2, respectively; the subscript indicates the initial rotational state. The concentration of the signal into a few peaks (of low initial rotation) is characteristic of a rotationally cold supersonic beam. Note that for these data the REMPI occurred in a modified configuration with no translatable skimmer and a valve-to-ionization region distance reduced to 25 cm. This was done to maximize signal; no qualitative difference in behavior was observed when adding the translatable skimmer and increasing the valve-to-ionization region distance.

After demonstrating our ability to send a molecular beam through the requisite skimmers and apertures and perform REMPI, we moved the molecular beam machine to the ion trap chamber (as pictured in Fig. 5.2b). The piezo valve and skimmers are placed on one side of the chamber, while the detection apparatus is placed on the other side. Both differential pumping stages utilize turbo pumps. To avoid introducing vibrations, the first turbo pump is a magnetically-levitated model, while the second is connected non-rigidly via a bellows (it is mechanically fixed to the overhead support structure). Both chambers reach a base pressure near 10^{-6} Pa when the beam is not being pulsed. The detection chamber includes a getter-ion combo pump and reaches a similar pressure; it is also closed off from the ion trap chamber via a gate valve when not in use.

We can roughly align the entire apparatus by sending an alignment laser beam along the molecular beam axis and seeing it (via a camera) reflecting off the PZT valve nozzle. At this stage, some amount of the molecular beam passing all the way through the ion trap chamber into the detection region can be ionized and detected. Final alignment of the translatable skimmer is done by optimizing molecular beam signal; with 2.4 mJ pulses, we can detect up to 8 ions per pulse on the CEM. The measured pulse shape and REMPI spectrum can be seen in Fig. 5.5. Now, confident that we can ionize several molecules per molecular beam pulse, we are ready to attempt loading molecular ions into our trap via REMPI.

Loading $N_2{}^+$ via REMPI is an ongoing project. The REMPI beam must be aligned carefully to avoid high charging rates (or worse, ablation of trap electrodes). To improve beam quality and thus mitigate these risks, we use a high-energy diamond pinhole as a spatial filter at an out-of-vacuum focal point. The ionization process is limited by the 2-photon $X^1\Sigma_g^+(v = 0) \rightarrow a^1\Pi_g(v = 10)$

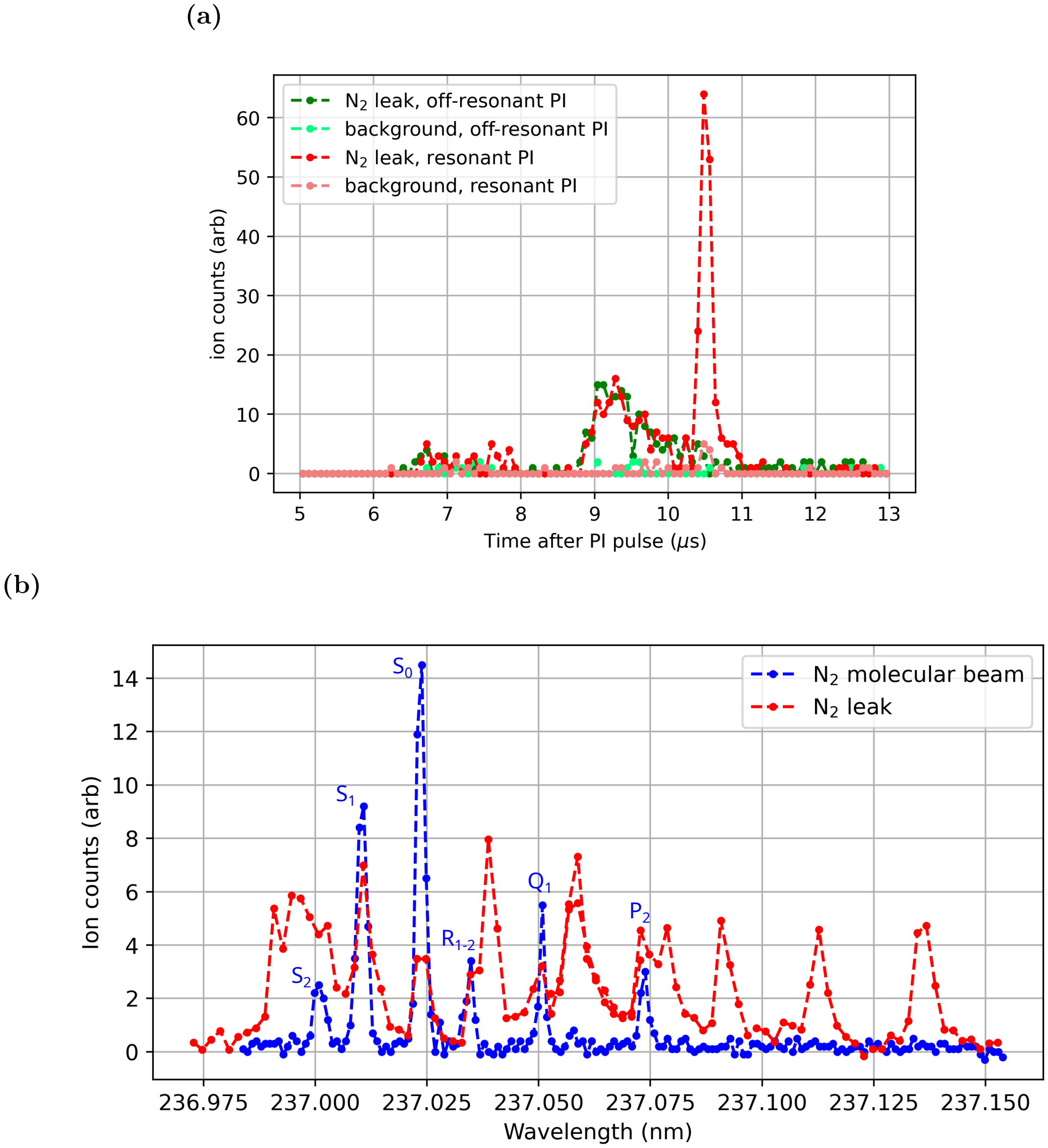

Figure 5.4: **(a) Sample TOF spectra.** The N_2 leak is introduced by sending low-density, frequent pulses of gas (not timed with the REMPI pulse) to increase the background pressure to $\sim 10^{-5}$ Pa, compared to the steady-state background of $\lesssim 10^{-7}$ Pa; the PI beam is set to 237.059 nm for resonant spectra and 236.953 nm for off-resonant spectra. Data is taken with 1.95 mJ PI pulses. The broad hump at ~9.2 μs, sensitive to N_2 pressure but insensitive to PI wavelength, is attributed to EII via photoemission. The narrow peak near 10.5 μs is attributed to REMPI of N_2. Subsequent REMPI data such as that shown in (b) is taken by considering only the integrated counts within this peak. **(b) The REMPI spectrum of $\mathbf{N_2}$.** The molecular beam data is taken in the test setup with only the fixed skimmer in place. The leak data is taken over two runs on different days and have been scaled to match in the overlap region. The relative peak heights of beam vs leak should not be directly compared. The wavelength is scanned via a grating forming the dye laser cavity and is measure on a wavemeter. The peaks in the spectrum are identified by comparing to literature; the lack of peaks originating in $J > 2$ indicates a rotational temperature of O(10 K) (see Eq. 2.8). The additional peaks in the leaked spectrum generally correspond to multiple transitions from different branches (see Ref. [93] for a simulated spectrum).

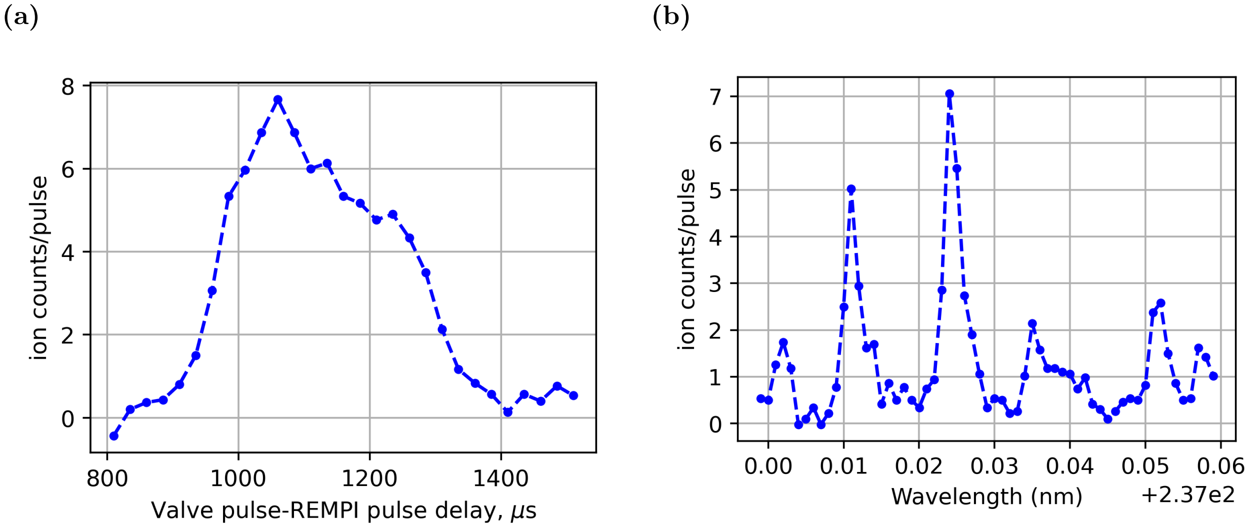

Figure 5.5: Molecular beam of N_2 passing through ion trap. Data taken with 2.4 mJ dye laser pulses. (a) REMPI signal at optimal wavelength as a function of delay between opening the piezo valve and triggering the dye laser. The flight time of 1.05 ms over a distance of 800 mm is consistent with the expected supersonic velocity of N_2. (b) REMPI spectrum of N_2. The spectrum is qualitatively similar to the spectrum observed after a single skimmer, see Fig. 5.4b.

resonant step and thus scales quadratically with pulse energy. We cannot directly calculate the required pulse energy without knowing the difference between ion loading efficiency and the detection chamber's collection efficiency; if we assume the two efficiencies are comparable, loading one ion per minute with a 20 Hz beam pulse repetition rate would require pulse energies of approximately 25 μJ. This is likely an underestimate of the required energy, since the actual trapping efficiency is expected to be relatively low.

5.4 Prospects of loading a broader class of molecular ions

A long-term goal of our experimental apparatus is to be able to study many different molecular ion species. One prerequisite to accomplish this is to be able to load the desired species.

So far, we have discussed (at least the prospect of) loading two different molecular species within our ion trap. One of these is ${N_2}^+$ via REMPI. Molecular beam loading efficiency is determined by (a) beam density and (b) ionization and capture efficiency. Regarding (a), N_2 has an advantage compared to an arbitrary molecule because it is possible to generate a pure beam of N_2. In contrast, most molecules suffer from the formation of weakly bound Van der Waals clusters within the low-temperature, high-density environment of a supersonic beam; the formation of such clusters causes heating and other unwanted effects, ultimately prohibiting pure beams [86]. However, virtually any gaseous molecule can be *seeded* at the ∼1-5% level in a non-interacting *carrier gas*, typically an inert gas such as helium, neon, argon, krypton, or xenon. The average velocity, velocity spread, and internal temperature of the resulting beam will be defined primarily by that of the carrier gas.[5] While seeding dilutes the density of the gas of interest, this can be partially compensated by using a light carrier gas with low velocity spread.

On the other hand, regarding (b), N_2 is one of the most challenging molecules to ionize via REMPI due to its high PI threshold (∼16 eV). We use a 2+1 REMPI scheme, which requires three 237 nm photons and a resonant $v = 0 \rightarrow 10$ transition with a relatively low FCF. A "typical" molecule will generally require less and/or lower-energy photons, making its ionization efficiency comparatively higher. Combining the considerations regarding beam density and ionization efficiency, we conclude that loading an arbitrary molecular ion will generally not be significantly more difficult than ${N_2}^+$; exact achievable loading efficiency will depend on available REMPI pathways.

Other technical limitations exist. A molecule ionized in the trapping region will not necessarily be permanently trapped; efficient sympathetic cooling is required. Cooling will be most efficient for $\alpha_{\mathrm{Ca}^+} \approx \alpha_{\mathrm{mol}}$. In Ref. [95], it was found that operating with multiple cooling ions during the REMPI loading process is beneficial for loading efficiency, a strategy we also plan to try. For molecules with many constituent atoms ($\gtrsim 5$, e.g. as discussed in Ref. [96]), fragmentation during the REMPI process can become a limiting factor. Introducing metals into a molecular beam is a technical challenge but has been demonstrated by ablating a target near the valve nozzle to seed a beam of carrier gas [97].

The other molecule we have discussed is CaH^+, which is formed via reaction with H_2 from an already-trapped Ca^+. As we consider broadening the range of molecules we would like to study in

---

[5] That is, molecules of both species that make up the beam will have the same average velocity, etc.—the expected value of the parameters can be found by the expected values of the constituents, weighted by their concentration in the beam [85].

our ion trap, we find that utilizing reactions is a widely valid strategy. For example, during some preliminary room-temperature tests, we consistently observed polyatomic molecule formation via the following reactions within our ion trap:

$$Ca^{+} + H_2O \rightarrow CaOH^{+} + H$$

$$N_2{}^{+} + H_2 \rightarrow N_2H^{+} + H$$

with $N_2{}^{+}$ loaded via EII and the (inferred) reactants likely due to residual contamination from pulsing the PZT valve. Here, the masses—and thus the likely identity—of the products, were inferred by observing the change in motional mode structure due to the change in α_{mol} (via probing a co-trapped Ca^{+} ion). More generally, reactions between ions and neutral molecules are typically fast because of long-range interaction between the charged particle and the molecule's induced (or, for polar species, permanent) dipole moment.[6]

With a molecular beam, much more complicated reactants can be introduced. For example, the Lewandowski group at JILA has observed and analyzed reactions between trapped ions and neutral molecular beams involving complex, organic compounds such as:

$$DC_3D_3 \text{ (propyne) (or } H_2C_3H_2 \text{ (allene))} + C_2D_2{}^{+} \text{ (acetylene)} \rightarrow \ldots \text{ [100]}$$

$$CH_3CN \text{ (acetonitrile)} + CCl^{+} \rightarrow \ldots \text{ [101]}$$

It should be noted that in these experiments (meant in fact to study the behavior of various reaction pathways), multiple reactions products are possible, a limitation if one's goal is to consistently form a particular molecular ion.

When loading CaH^{+} via reaction, we do not typically introduce H_2 from the molecular beam but instead rely on background gas by increasing the cold stage temperature above the H_2 desorption threshold, which is not possible for an arbitrary molecule. However, since other species will stick very efficiently to cryogenic surfaces, we can introduce molecular beam pulses at a high repetition rate without worrying about vacuum degradation. Under typical conditions, we estimate that we

---

[6] In fact, any ion trapper with less-than-ideal vacuum conditions (or a trap with many ions) will complain about undesired reactions with H_2, which is typically the most abundant background gas in a UHV system. BeH^{+} [98], CaH^{+}, AlH^{+}[55], and BaH^{+}[99] are just some examples of observed accidental molecular ion formation in ion traps via reaction.

will be able to generate a molecular reaction between a trapped ion and a molecule from the beam on a timescale of O(minutes).

As proof that REMPI loading is a general loading technique for a broad class of interesting molecules, I describe available REMPI pathways for a handful of molecules pertinent for possible precision measurement applications in Table 5.1. Note that all of these molecules have many demonstrated or calculated REMPI pathways; I have simply chosen one convenient, single-color scheme for each. Some future plans for the apparatus, including investigation of some of the molecules referenced in Table 5.1, will be discussed in Chapter 6.

Table 5.1: Available single-color REMPI schemes for select molecular species with proposed precision measurement applications.

Species	Scheme	λ (nm)	YAG harmonic/dye	Proposed application
N_2	2 + 1 [92]	237	3rd/Coumarin 480	Base for N_2H^+, interstellar chemistry [31, 102]
CO	2 + 1 [103]	230	3rd/Coumarin 480	Base for COH^+/HCO^+, resolvable isomers
O_2	2 + 1 [104]	301	2nd/Rhodamine 610	Sensitive m_p/m_e variation measurement [29]
CHDBrI	1 + 1 [96]	250	3rd/Coumarin 503	Parity violation measurement [30, 96]

Chapter 6

Conclusions and outlook

In this thesis I have described the design and construction of an experimental apparatus for achieving quantum state control of a broad range of molecular ion species. I have also demonstrated high-fidelity SPAM and coherent manipulation of CaH^+. This demonstration, however, only scratches the surface of the possibilities afforded by such a device. In this chapter, I will recapitulate key takeaways from our experiments, outline several system upgrades that will allow us to achieve an even greater level of control, and propose future experiments involving new molecular species that could be pursued in this apparatus.

6.1 Experimental findings and contextualization

We have demonstrated a molecule-ambivalent protocol for high-fidelity molecular quantum state control, achieving record single quantum state SPAM and transfer fidelities above 99.4% in CaH^+. These results were enabled by rotational state lifetimes enhanced by an order of magnitude due to cryogenic operation. Our techniques are generalizable to a variety of molecular species, enabling a new regime of precision measurement, QIP, and chemistry applications with molecules.

The approach presented here can be compared to that demonstrated in Ref. [42], which uses multiple QLS probes to identify the rovibrational manifold of an N_2^+ ion with $\gtrsim 99\%$ fidelity. However, our approach stands out by affording sublevel-specific state preparation, allowing for high-fidelity, single-quantum-state, coherent operations. In Ref. [43], QLS with ${H_2}^+$ is used to achieve single quantum state-resolving, coherent manipulation; however, fidelities in that work are limited to

$\lesssim 90\%$. Additionally, our results are achieved with a polar molecule susceptible to TR-induced transitions by reducing the ambient temperature and using adaptive Bayesian detection to minimize measurement duration. Similar experiments with CaH^+ in the room-temperature apparatus in the Ion Storage Group have only achieved $\lesssim$97% fidelity, limited primarily by TR.

Loading of an ion trap via REMPI from a molecular beam has previously been demonstrated [42, 95]. Alternative, less technically demanding methods for loading molecular ions for QLS are also possible. For example, EII loading of ${H_2}^+$ from ambient background gas has also been realized [43]; however, this scheme suffers from long loading times and significant charging effects. Moreover, loading any other molecular species with this strategy would likely be impractical. Another possibility is introducing molecules effusively through a room-temperature orifice, though gas and heat loads are both concerns with this design. Yet another alternative is loading in a room-temperature trap and then using ion optics and fast-ramping trap voltages to shuttle ions into a separate, cryogenic trap; this alleviates some problems associated with charging and neutral gas delivery but introduces an alternative set of technical challenges.

Demonstrating reliable REMPI-based molecular beam loading in our cryogenic wheel trap—unlike the room-temperature, larger-volume, 4-rod trap used in Ref. [42]—has posed a significant challenge due to smaller apertures, charging, and reduced trapping volume. Nevertheless, I believe that REMPI loading from a beam is the most promising method for loading a cryogenic apparatus with a general molecular species for precision experiments.

6.2 Potential system upgrades

Only about 8 months have elapsed between the first attempts at molecular spectroscopy in the cryogenic experiment and the submission of this thesis. Most of this time has been focused on developing and debugging the control software, finding optimal loading and calibration procedures, and pushing the limits of system performance with CaH^+. Along the way, we have identified several deficiencies in the system that we would like to eventually address.

6.2.1 Improving rotational state lifetimes

We calculate an expected cold stage temperature of 8.6 K but measure a cold stage temperature of 16 K. We attribute much of this discrepancy to the higher-than-expected temperature of the radiation shield stage, which reaches a measured base temperature of 189 K, compared to an expected 86 K; we suspect this difference is due to a loose mechanical (i.e., thermal) connection between the copper braids and the Stinger's radiation shield. One piece of evidence for this is that cool down of the radiation shield stage occurs on a longer time scale than that of the cold stage, as shown by the temperature log in Fig. 6.1. This is despite the fact that radiation shield copper braids have a significantly larger cross-sectional area, and thus expected thermal conductivity, than those for the cold stage. Other reasons to suspect this connection is compromised are that the radiation shield braids connect with a lower total surface area and that flat-head rather than hex-head[1] screws were used for these connections due to part availability. Finally, significant stress may have accidentally been placed on the braid connections during vacuum assembly due to the fact that the vacuum sections on either side of the braids are not rigidly connected. Some pictures from the vacuum assembly are shown in Fig. 6.2.

The apparatus was not designed for modular iterations. As shown in Fig. 6.2c, accessing the lower portion of the vacuum chamber requires pulling the entire vacuum system out of the optical table. Making the system more modular, for example by allowing the copper braid connections to be accessed from above, would allow for easier future modifications to the system. If/when the copper braid connection problem is addressed, such an upgrade could perhaps be incorporated.

Reducing the radiation shield stage temperature would reduce the temperature of the cold stage (due to reduced thermal load),[2] thus reducing the total TR incident on the ion. Still, the observed differential between the ion's effective temperature (∼35 K as inferred from rotational state lifetime) and the measured cold stage temperature suggests that at least one other factor

---

[1] Hex-head screws were used for all other thermal connections in the assembly and can be tightened significantly more than the flat-head variety.

[2] It may also reduce the leaked TR, since much of that will originate from the radiation shield stage, though some will also come from room-temperature surfaces.

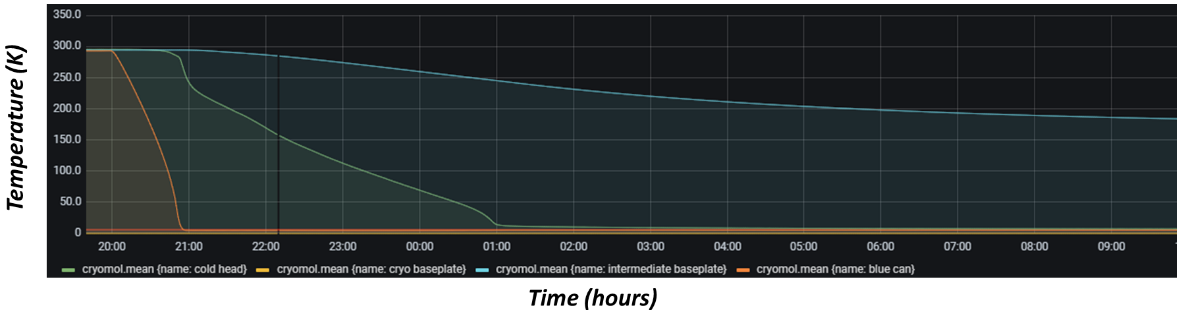

Figure 6.1: A typical log of the apparatus cooling down from room temperature. The Stinger itself ("blue can") cools down in about one hour; the temperature at the cold tip ("cold head") approaches base temperature after 5 hours; after that it is limited by the radiation shield stage temperature ("intermediate baseplate"), which takes about 16 hours to reach equilibrium. The longer thermalization time of the radiation shield stage suggests that it may suffer from a compromised thermal connection.

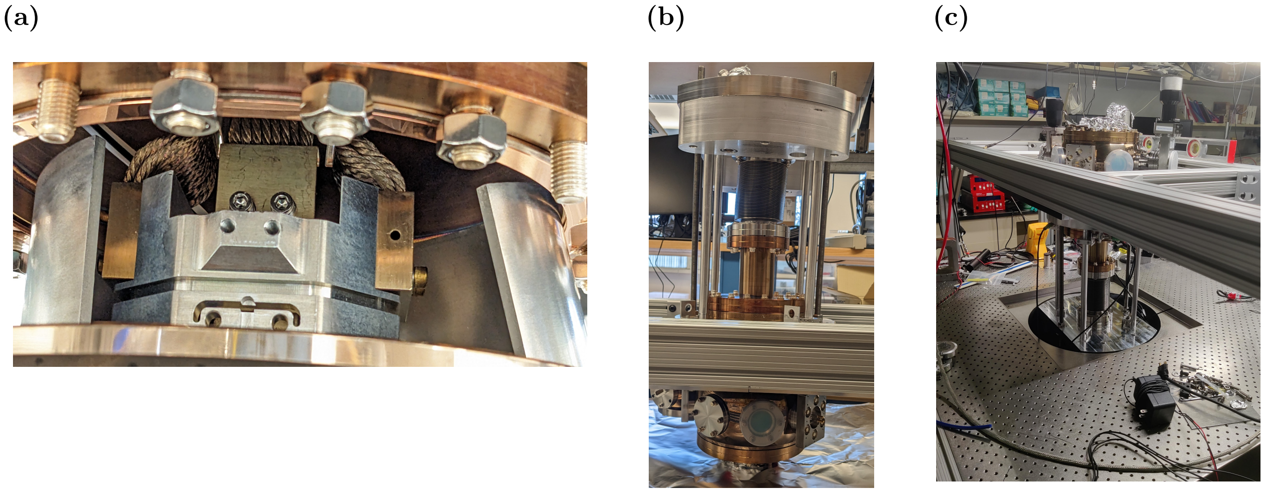

Figure 6.2: **(a) The copper braids during vacuum assembly.** The connections to the cold stage (center braid) and radiation shield stage (left and right braids) can be seen. **(b) Vacuum chamber during assembly.** A homemade 80/20 cart was used to maneuver the vacuum chamber. Two threaded rods were temporarily installed during assembly and transport to constrain movement of the components above and below the non-rigid connections (i.e., the copper braids and the bellows visible in this picture). The crookedness of the bellows suggests that some relative movement still occurred, perhaps causing the mechanical connection between the copper braids and the radiation shield to fail. **(c) Lowering the vacuum chamber into the optical table.** Accessing the copper braids for modification would be an invasive process requiring this step to be reversed.

contributes significantly to reduction of state lifetimes. As addressed in Section 4.4, possible reasons include contribution from leaked TR and trap geometry effects. To further isolate the root cause, we would need to iterate through different in-vacuum designs. For example, we could switch in different windows (a thicker substrate, an ITO coating, or a fine metal mesh may reject certain frequencies more effectively than our current design), change the RAM tile configuration, or introduce a different ion trap with different geometry. Such investigations would be interesting in their own right but are unlikely to be the subject of near-term investigations in our apparatus.

The extent to which the ion's effective temperature matters for a particular experiment is dependent on both the molecular species under study and the application. For example, most molecular species have $B_{R,\mathrm{mol}} < B_{R,\mathrm{CaH}^+}$, meaning that (from Eqs. 2.4 and 2.5) their lowest-lying rotational levels will have longer lifetimes than those found in CaH$^+$. However, such molecules may also have smaller vibrational level splittings; if $\Delta E_v \lesssim k_B T$, excited vibrational states will contain appreciable equilibrium population fractions, keeping TR reduction relevant.

Applications in molecular QIP have the strictest fidelity requirements and thus will be most sensitive to TR-induced transition rates. The focus for this apparatus moving forward will likely be in precision measurement applications, which may not require such high fidelity. Nevertheless, minimizing TR remains valuable in this context when searching for weak or unknown signals and for maximizing duty cycle.

6.2.2 Reducing motional mode drift

A technical issue that currently plagues day-to-day operations in our experiment is motional mode frequency drift. This drift always occurs monotonically whenever we turn on our highest-power (729 nm or 1064 nm) beams. The fastest drifts are observed due to the 729 nm vertical beam,[3] which does not cleanly exit the chamber but rather scatters off various electrodes and other surfaces near the trap. Without servoing, and with typical beam powers and duty cycles used in molecular spectroscopy experiments, the drift rate of the axial OOP mode frequency is ~ 5 Hz/s. This sets the timescale at which we must pause experiments to servo the axial confinement. It also limits the beam power we are able to use in some cases, e.g., during CSB cooling, slowing down our operations

---

[3] Fortunately, this beam is not used during typical experimental operation except for occasional micromotion checks.

and ultimately limiting the fidelity of our experiment.

The mechanism for this drift is hypothesized to be due either to charging or temperature effects (note that either could be exacerbated by operating in a cryogenic system). Whatever the underlying mechanism, the drift is clearly caused by photons scattering within the cold stage, and indeed we have measured, e.g., $\gtrsim 20\%$ loss of the 1064 σ beam between entrance and exit of the vacuum chamber. When vacuum is next opened, it will be instructive to determine exactly where this loss is occurring and address it accordingly.

6.2.3 Incorporating a general rotational transition drive

The only control we have over rotational levels is via a 285 GHz microwave source driving the $J = 0 \leftrightarrow 1$ transition; otherwise, the molecule's rotational level is determined stochastically due to spontaneous and TR-induced transitions. Given our TR environment and the rotational level splittings of CaH$^+$, this is sufficient to perform experiments with the molecule in $J = 1(2)$ 48(36)% of the time, a reasonable experimental duty cycle. However, if we wanted to perform an experiment in a higher J level, we would be saddled with much lower duty cycle. Another concerning consideration is that when operating with a molecule with a lower rotational constant such as COH$^+$ ($B_R = 89$ GHz), the rotational level lifetimes will be O(minutes), and in equilibrium the molecule will be spread over $J \approx 0 - 8$. Thus, to make a measurement in a particular J, we could easily be waiting 10 minutes or longer. Having the ability to drive rotational transitions could allow for deterministic rotational level preparation, drastically improving the duty cycle for many conceivable experiments.

Our current Raman beams' available relative frequency span is limited by the double-pass AOM bandwidth, which is ∼100 MHz; this is far too small to drive rotational transitions that are typically 10s or 100s of GHz. Introducing two paths of a frequency comb as a Raman drive provides an attractive and versatile option for driving transitions between rotational levels [45]. Frequency combs can cover a spectral range of 10s of THz. If a Raman beam path is sent through an AOM with bandwidth greater than the comb tooth spacing f_{rep}, any frequency difference within the comb's spectral range can be accessed by scanning the relative detuning of the paths. Since all of the comb teeth are equally spaced, once the frequency difference of any two pairs of comb teeth matches that of the transition to drive, all comb teeth will be part of a pair that will contribute to coherently driving the transition, as illustrated in Fig. 6.3. This strategy for driving rotational transitions has previously been demonstrated on CaH$^+$ [45].

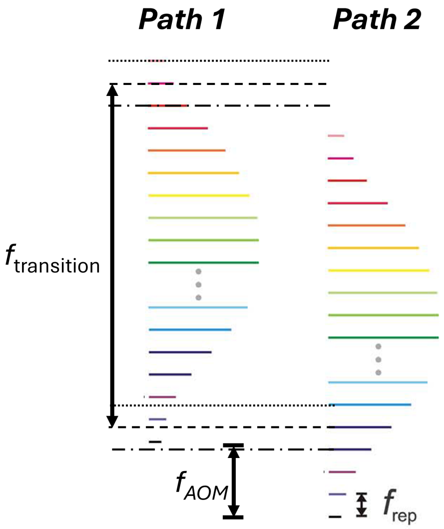

Figure 6.3: Using a frequency comb to drive rotational Raman transitions. The comb light is split into two paths, which are both ultimately sent to the ion to form a Raman drive; an AOM is used to shift the frequency of one of the paths. An AOM frequency can be found such that pairs of comb teeth line up to drive the transition ($f_{\text{transition}} = n \times f_{\text{rep}} + f_{\text{AOM}}$, where n is an integer). Pairs of lines with the same dash style indicate different pairs of comb teeth (one from each path) that contribute to driving the transition. Figure adapted from [45].

For a linear molecule, selection rules require that a two-photon Raman transition satisfies $\Delta J = 0, \pm 2$. For fully deterministic state preparation, a method for driving $\Delta J = \pm 1$, such as the microwave source we currently use, would still be required. In addition to deterministic state preparation, using a frequency comb to coherently drive rotational transitions would enable exciting scientific applications in precision measurement and quantum information.

6.3 Prospects for future experiments

While the experiments performed so far with this apparatus have been confined to CaH$^+$, we are actively working towards loading and spectroscopy of other molecular ion species, chiefly for precision measurement applications. Any change in species will bring unique experimental challenges, but the ability to work with increasingly complex molecules brings expanded scientific opportunities.

6.3.1 Limitations on usable species

A major premise of our experimental design is that it is generalizable to many molecular species. Before discussing what species with which we may wish to operate for future experiments, I will first mention some restrictions to the species we can choose.

- **Charge-to-mass ratio**: We must work with molecules whose charge-to-mass ratio α_{mol} is within a factor of a few of our chosen auxiliary ion, $^{40}\mathrm{Ca}^+$, for two reasons. One is that ions with $\alpha_{\mathrm{mol}} \ll \alpha_{\mathrm{Ca}^+}$ will not be included in the trap stability region for typical operating parameters. A second is that for large α mismatches, participation in the shared motional normal modes is significantly imbalanced, hindering sympathetic cooling and quantum logic transfer (QLS experiments with imbalances as large as $\frac{1}{4.5}$ [43]$\leq \frac{\alpha_{\mathrm{mol}}}{\alpha_{\mathrm{aux}}} \leq 3$ [80][4] have been realized). However, this is not a fundamental problem; quantum logic-style operation with molecules has been demonstrated with auxiliary ions ranging from $^{9}\mathrm{Be}^+$ [43] to $^{226}\mathrm{Ra}^+$ [63], allowing for α_{mol}'s spanning more than two orders of magnitude.
- **Molecular beam loading**: In our apparatus, loading a particular molecule requires that it can be included in a molecular beam and ionized with REMPI (or formed by successive reactions beginning with such a molecule). This applies to a broad class of gaseous molecules and could even be expanded to some metallic species [97]. Recently, the organic molecule aminostyrene (C_8H_9N) was loaded in this manner [105]; the Lewandowski group has demonstrated loading a variety of large molecules [28, 100, 101], including using reactions. A more detailed discussion of molecular beam loading considerations is provided in Section 5.4.
- **Internal level structure complexity:** Molecules with more complicated internal level structures will become increasingly difficult to prepare in a particular sublevel using the

---

[4] Strictly speaking, Ref. [80] probes an atom rather than a molecule, but the α-mismatch challenge is analogous.

methods described in this thesis. Higher nuclear spin leads to denser sublevel structure, while polyatomic molecules will have additional vibrational and (if non-linear) rotational degrees of freedom. We expect that our molecular quantum state control toolbox will expand by necessity as we work with progressively more complicated molecules, but it is still unlikely that we will ever boast the same level of control of, say, an organic molecule as we currently do with CaH^+.

With these limitations in mind, I list some experiments that could feasibly be pursued in our system.

6.3.2 Isomer detection and state-resolved chemistry

Isomers—molecules with different arrangements of the same constituent atoms—have similar energy level structures and are thus difficult to distinguish using standard molecular spectroscopy techniques (and impossible using techniques that rely on differences in α such as direct mass spectrometry). Current methods typically rely on bulk behavior (chromatography [106], nuclear magnetic resonance [107]) or destructive techniques (fragmentation patterns [108], reaction tendencies [109]). The QLS protocol described in this thesis could provide a non-destructive, single molecule-resolving method for differentiating isomers, since isomeric differences in rotational (and perhaps rotational Zeeman sublevel) energy splittings are readily resolvable.

As a demonstration of this capability, we consider the isomers $\mathrm{COH}^+/\mathrm{HCO}^+$. As a linear molecule with $B_{R,\mathrm{COH}^+} = 89$ GHz [48] and nuclear spin 1/2, COH^+ has a similar rotational and sublevel structure as CaH^+. CO^+ can be readily formed from single-color REMPI [103],[5] and reaction with H_2 can probabilistically form either isomer. For proper choice of magnetic field amplitude, the $J = 1$ signature transitions in the two isomers differ by $\sim$1 kHz; differences in rotational splittings are much greater. Thus, we could load either isomer in our trap and differentiate the two with near-unity efficiency.

Perhaps the most exciting prospect of the isomer differentiation capability is that we have

---

[5] NIST protocols make working with CO gas prohibitively difficult; we currently plan 3+1 REMP(dissociative)I from CO_2 [110].

control of the quantum state which the molecule occupies. One could imagine, for example, preparing CO^+ in various quantum states before the reaction with H_2 occurs and observing differences in the relative likelihood of the two isomers to form. State-resolved chemistry is an exciting and active area of research [27].

6.3.3 Spectroscopy for interstellar chemistry

Our apparatus allows us to measure transitions in molecular ions with a precision orders of magnitude better than current standards [45, 46]. Astrophysics is a field in which knowing spectral lines with high precision is crucial [31]. N_2H^+ and COH^+ are two molecular ions prevalent in the interstellar medium [102, 111], and identification of their (rotational transition) lines within dense spectra can be crucial, e.g., for determining H_2 density in a particular region of interstellar space [112]. With the introduction of a suitable frequency comb, we could measure such lines with unprecedented precision, allowing astrophysicists to identify them unambiguously.

6.3.4 Larger molecules towards parity violation observation

As we continue to build our molecular control toolbox, we expect to begin performing experiments with larger molecules with a more complex internal structure. One exciting potential application is observation of parity violation. Predicted spectroscopic shifts between enantiomers (opposite-handed chiral molecules) are small but, for the appropriate choice of molecule, are predicted to be of O(1 Hz) [96], a level which is feasibly resolvable in our system. Note that chiral molecules must consist of a minimum of 4 constituent atoms in a fully asymmetric configuration, meaning that they will have three distinct rotational modes with which to contend. Besides internal state complexity, dissociation during ionization can also be a significant challenge for such large molecules; Ref. [96] suggests several candidate molecules suitable for both REMPI ion production and spectroscopic parity violation measurements.

6.4 Conclusion

As the field of quantum state control progresses further into the molecular frontier, quantum logic will be a powerful tool. After many years of focusing on CaH^+ within the molecular branch of the Ion Storage Group, it is exciting and rewarding to begin experiments with new species. Recent work has been directed towards demonstration of loading ${N_2}^+$ into the trap, with CO^+ loading coming close behind. I look forward to seeing the results that emerge from the cryogenic molecular ion trapping apparatus in the years to come.

References

[1] M. H. Anderson, J. R. Ensher, M. R. Matthews, C. E. Wieman, and E. A. Cornell, “Observation of Bose-Einstein Condensation in a Dilute Atomic Vapor”, Science **269**, 198 (1995) (Cited on p. 2).

[2] K. B. Davis, M. O. Mewes, M. R. Andrews, N. J. van Druten, D. S. Durfee, D. M. Kurn, and W. Ketterle, “Bose-Einstein Condensation in a Gas of Sodium Atoms”, Phys. Rev. Lett. **75**, 3969 (1995) (Cited on p. 2).

[3] P. Jessen, C. Gerz, P. Lett, W. Phillips, S. Rolston, R.J.C, Spreeuw, and C. Westbrook, “Observation of quantized motion of Rb atoms in an optical field”, Phys. Rev. Lett. **69**, 49 (1992) (Cited on p. 2).

[4] N. Schlosser, G. Reymond, I. Protsenko, and P. Grangier, “Sub-poissonian loading of single atoms in a microscopic dipole trap”, Nature **411**, 1024 (2001) (Cited on p. 2).

[5] W. S. Bakr, A. Peng, M. E. Tai, R. Ma, J. Simon, J. I. Gillen, S. Fölling, L. Pollet, and M. Greiner, “Probing the Superfluid–to–Mott Insulator Transition at the Single-Atom Level”, Science **329**, 547 (2010) (Cited on p. 2).

[6] R. A. Hart, P. M. Duarte, T.-L. Yang, X. Liu, T. Paiva, E. Khatami, R. T. Scalettar, N. Trivedi, D. A. Huse, and R. G. Hulet, “Compressibility of a Fermionic Mott Insulator of Ultracold Atoms”, Nature **519**, 211 (2015) (Cited on p. 2).

[7] S. M. Brewer, J.-S. Chen, A. M. Hankin, E. R. Clements, C. W. Chou, D. J. Wineland, D. B. Hume, and D. R. Leibrandt, “$^{27}\mathrm{Al}^{+}$ Quantum-Logic Clock with a Systematic Uncertainty below 10^{-18}”, Phys. Rev. Lett. **123**, 033201 (2019) (Cited on pp. 2, 3, 19).

[8] A. Aeppli, K. Kim, W. Warfield, M. S. Safronova, and J. Ye, “Clock with 8×10^{-19} Systematic Uncertainty”, Phys. Rev. Lett. **133**, 023401 (2024) (Cited on p. 2).

[9] A. Beyer, L. Maisenbacher, A. Matveev, R. Pohl, K. Khabarova, A. Grinin, T. Lamour, D. C. Yost, T. W. Hänsch, N. Kolachevsky, and T. Udem, “The Rydberg constant and proton size from atomic hydrogen”, Science **358**, 79 (2017) (Cited on p. 2).

[10] L. Morel, Z. Yao, P. Clad’e, and S. Guellati-Kh’elifa, “Determination of the fine-structure constant with an accuracy of 81 parts per trillion”, Nature **588**, 61 (2020) (Cited on p. 2).

[11] F. A. An, A. Ransford, A. Schaffer, L. R. Sletten, J. Gaebler, J. Hostetter, and G. Vittorini, “High Fidelity State Preparation and Measurement of Ion Hyperfine Qubits with $I > \frac{1}{2}$”, Phys. Rev. Lett. **129**, 130501 (2022) (Cited on p. 2).

[12] A. Ransford, C. Roman, T. Dellaert, P. McMillin, and W. C. Campbell, “Weak dissipation for high-fidelity qubit-state preparation and measurement”, Phys. Rev. A **104**, L060402 (2021) (Cited on p. 2).

[13] C. Ryan-Anderson, J. G. Bohnet, K. Lee, D. Gresh, A. Hankin, J. P. Gaebler, D. Francois, A. Chernoguzov, D. Lucchetti, N. C. Brown, T. M. Gatterman, S. K. Halit, K. Gilmore, J. A. Gerber, B. Neyenhuis, D. Hayes, and R. P. Stutz, "Realization of Real-Time Fault-Tolerant Quantum Error Correction", Phys. Rev. X **11**, 041058 (2021) (Cited on p. 2).

[14] H. Bernien, S. Schwartz, A. Keesling, H. Levine, A. Omran, H. Pichler, S. Choi, A. S. Zibrov, M. Endres, M. Greiner, V. Vuletić, and M. D. Lukin, "Probing many-body dynamics on a 51-atom quantum simulator", Nature **551**, 579 (2017) (Cited on p. 3).

[15] M. S. Safronova, V. A. Dzuba, V. V. Flambaum, U. I. Safronova, S. G. Porsev, and M. G. Kozlov, "Highly Charged Ions for Atomic Clocks, Quantum Information, and Search for α variation", Phys. Rev. Lett. **113**, 030801 (2014) (Cited on p. 3).

[16] W. B. Cairncross, D. N. Gresh, M. Grau, K. C. Cossel, T. S. Roussy, T. Ni, Y. Zhou, J. Ye, and E. A. Cornell, "Precision Measurement of the Electron's Electric Dipole Moment Using Trapped Molecular Ions", Phys. Rev. Lett. **119**, 153001 (2017) (Cited on pp. 3, 59).

[17] O. Grasdijk, O. Timgren, J. Kastelic, T. Wright, S. Lamoreaux, D. DeMille, K. Wenz, M. Aitken, T. Zelevinsky, T. Winick, and D. Kawall, "CeNTREX: a new search for time-reversal symmetry violation in the ^{205}Tl nucleus", Quantum Sci. Technol. **6**, 044007 (2021) (Cited on pp. 3, 59).

[18] J. J. Hudson, D. M. Kara, I. Smallman, B. E. Sauer, M. R. Tarbutt, and E. A. Hinds, "Improved measurement of the shape of the electron", Nature **473**, 493 (2011) (Cited on pp. 3, 59).

[19] A. collaboration, J. Baron, W. Campbell, D. DeMille, J. Doyle, G. Gabrielse, Y. Gurevich, P. Hess, N. Hutzler, E. Kirilov, et al., "Order of magnitude smaller limit on the electric dipole moment of the electron", Science **343**, 269 (2014) (Cited on pp. 3, 59).

[20] L. R. B. Picard, A. J. Park, G. E. Patenotte, S. Gebretsadkan, D. Wellnitz, A. M. Rey, and K.-K. Ni, "Entanglement and iSWAP Gate between Molecular Qubits", Nature **637**, 60 (2024) (Cited on pp. 3, 59).

[21] Y. Bao, S. S. Yu, L. Anderegg, E. Cahe, W. Ketterle, K.-K. Ni, and J. Doyle, "Dipolar spin-exchange and entanglement between molecules in an optical tweezer array", Science **382**, 1138 (2023) (Cited on pp. 3, 59).

[22] V. V. Albert, J. P. Covey, and J. Preskill, "Robust encoding of a qubit in a molecule", Physical Review X **10**, 031050 (2020) (Cited on pp. 3, 59).

[23] C. M. Holland, Y. Lu, and L. W. Cheuk, "On-demand entanglement of molecules in a reconfigurable optical tweezer array", Science **382**, 1143 (2023) (Cited on pp. 3, 59).

[24] K. H. Leung, B. Iritani, E. Tiberi, I. Majewska, M. Borkowski, R. Moszynski, and T. Zelevinsky, "Terahertz Vibrational Molecular Clock with Systematic Uncertainty at the 10^{-14} Level", Phys. Rev. X **13**, 011047 (2023) (Cited on p. 3).

[25] N. Bigagli, W. Yuan, S. Zhang, B. Bulatovic, T. Karman, I. Stevenson, and S. Will, "Observation of Bose-Einstein condensation of dipolar molecules", Nature **631**, 289 (2024) (Cited on pp. 3, 4).

[26] H. Son, J. J. Park, Y.-K. Lu, A. O. Jamison, T. Karman, and W. Ketterle, "Control of reactive collisions by quantum interference", Science **375**, 1006 (2022) (Cited on pp. 3, 59).

[27] Y. Liu, D. D. Grimes, M.-G. Hu, and K.-K. Ni, "Probing ultracold chemistry using ion spectrometry", Phys. Chem. Chem. Phys. **22**, 4861 (2020) (Cited on pp. 3, 101).

[28] O. A. Krohn, K. J. Catani, J. Greenberg, S. P. Sundar, G. da Silva, and H. J. Lewandowski, “Isotope-specific reactions of acetonitrile (CH_3CN) with trapped, translationally cold CCl^+”, J. Chem. Phys. **154**, 074305 (2021) (Cited on pp. 3, 59, 99).

[29] D. Hanneke, R. A. Carollo, and D. A. Lane, “High sensitivity to variation in the proton-to-electron mass ratio in ${O_2}^+$”, Phys. Rev. A **94**, 050101 (2016) (Cited on pp. 3, 91).

[30] E. B. Norrgard, D. S. Barker, S. Eckel, J. A. Fedchak, N. N. Klimov, and J. Scherschligt, Communications Physics **2**, 77 (2019) (Cited on pp. 3, 91).

[31] S. L. W. Weaver, “Millimeterwave and Submillimeterwave Laboratory Spectroscopy in Support of Observational Astronomy”, Annuv. Rev. Astron. Astrophys **57**, 79 (2019) (Cited on pp. 3, 91, 101).

[32] Y. Lin, D. R. Leibrandt, D. Leibfried, and C.-w. Chou, “Quantum entanglement between an atom and a molecule”, Nature **581**, 273 (2020) (Cited on pp. 3, 6, 13, 59).

[33] E. S. Shuman, J. F. Barry, and D. DeMille, “Laser cooling of a diatomic molecule”, Nature **467**, 820 (2010) (Cited on pp. 4, 59).

[34] D. Mitra, N. B. Vilas, C. Halla, L. Anderegg, B. L. Augebraum, L. Baum, C. Miller, S. Raval, and J. M. Doyle, “Direct laser cooling of a symmetric top molecule”, Science **369**, 1366 (2020) (Cited on pp. 4, 59).

[35] G.-Z. Zhu, D. Mitra, B. L. Augenbraun, C. E. Dickerson, M. J. Frim, G. Lao, Z. D. Lasner, A. N. Alexandrova, W. C. Campbell, J. R. Caram, et al., “Functionalizing aromatic compounds with optical cycling centres”, Nature chemistry **14**, 995 (2022) (Cited on pp. 4, 59).

[36] S. Truppe, H. Williams, M. Hambach, L. Caldwell, N. Fitch, E. Hinds, B. Sauer, and M. Tarbutt, “Molecules cooled below the Doppler limit”, Nature Physics **13**, 1173 (2017) (Cited on pp. 4, 59).

[37] W. B. Cairncross, J. T. Zhang, L. R. B. Picard, Y. Yu, K. Wang, and K.-K. Ni, “Assembly of a Rovibrational Ground State Molecule in an Optical Tweezer”, Phys. Rev. Lett. **126**, 123402 (2021) (Cited on pp. 4, 59).

[38] D. K. Ruttley, A. Guttridge, S. Spence, R. C. Bird, C. R. L. Sueer, J. M. Hutson, and S. L. Cornish, “Formation of Ultracold Molecules by Merging Optical Tweezers”, Phys. Rev. Lett. **130**, 223401 (2023) (Cited on pp. 4, 59).

[39] C. He, X. Nie, V. Avalos, S. Botsi, S. Kumar, A. Yang, and K. Dieckmann, “Efficient Creation of Ultracold Ground State $^6Li^{40}K$ Polar Molecules”, Phys. Rev. Lett. **132**, 243401 (2024) (Cited on pp. 4, 59).

[40] P. O. Schmidt, T. Rosenband, C. Langer, W. M. Itano, J. C. Bergquist, and D. J. Wineland, “Spectroscopy Using Quantum Logic”, Science **309**, 749 (2005) (Cited on p. 5).

[41] F. Wolf, Y. Wan, J. C. Heip, F. Gerbert, C. Shi, and P. O. Schmidt, “Non-destructive state detection for quantum logic spectroscopy of molecular ions”, Nature **530**, 457 (2016) (Cited on p. 5).

[42] M. Sinhal, Z. Meir, K. Najafian, G. Hegi, and S. Willitsch, “Quantum-nondemolition state detection and spectroscopy of single trapped molecules”, Science **367**, 6483 (2020) (Cited on pp. 5, 59, 92, 93).

[43] D. Holzapfel, F. Schmid, N. Schwegler, O. Stadler, M. Stadler, A. Ferk, J. P. Home, and D. Kienzler, “Quantum Control of a Single H_2^+ Molecular Ion”, Phys. Rev. X **15**, 031009 (2025) (Cited on pp. 5, 35, 92, 93, 99).

[44] C.-w. Chou, C. Kurz, D. B. Hume, P. N. Plesso, D. R. Leibrandt, and D. Leibfried, "Preparation and coherent manipulation of pure quantum states of a single molecular ion", Nature **545**, 203 (2017) (Cited on pp. 5, 6, 13, 35, 49, 51, 55, 60).

[45] C. W. Chou, A. L. Collopy, C. Kurz, Y. Lin, M. E. Harding, P. N. Plessow, T. Fortier, S. Diddams, D. Leibried, and D. R. Leibrandt, "Frequency-comb spectroscopy on pure quantum states of a single molecular ion", Science **367**, 1458 (2020) (Cited on pp. 6, 13, 97, 98, 101).

[46] A. L. Collopy, J. Schmidt, D. Leibfried, D. R. Leibrandt, and C.-W. Chou, "Effects of an Oscillating Electric Field on and Dipole Moment Measurement of a Single Molecular Ion", Phys. Rev. Lett. **130**, 223201 (2023) (Cited on pp. 6, 13, 14, 35, 46, 66, 68, 101).

[47] Y. Liu, J. Schmidt, Z. Liu, D. R. Leibrandt, D. Leibfried, and C.-w. Chou, "Quantum state tracking and control of a single molecular ion in a thermal environment", Science **385**, 790 (2024) (Cited on pp. 6, 13, 35, 60, 66, 68, 73, 74).

[48] R. C. Woods, R. J. Saykally, T. G. Anderson, T. A. Dixon, and P. G. Szanto, "Electromagnetic traps for charged and neutral particles", J. Chem. Phys. **79**, 4256 (1981) (Cited on pp. 14, 100).

[49] W. Paul and H. Steinwedel, "Ein neues Massenspektrometer ohne Magnetfeld", Zeitschrift für Naturforschung A **8**, 448 (1953) (Cited on p. 16).

[50] W. Paul, "Electromagnetic traps for charged and neutral particles", Rev. Mod. Phys. **62**, 531 (1990) (Cited on p. 16).

[51] D. Leibfried, R. Blatt, C. Monroe, and D. Wineland, "Quantum dynamics of single trapped ions", Review of Modern Physics **75**, 281 (2003) (Cited on pp. 16, 36, 37).

[52] E. Mathieu, "Mémoire sur le mouvement vibratoire d'une membrane de forme elliptique.", Journal de Mathématiques Pures et Appliquées **13**, 137 (1868) (Cited on p. 17).

[53] D. J. Wineland, C. Monroe, W. M. Itano, D. Leibfried, B. E. King, and D. M. Meekhof, "Experimental issues in coherent quantum-state manipulation of trapped atomic ions", Journal of research of the National Institute of Standards and Technology **103**, 259 (1998) (Cited on pp. 17, 36).

[54] J. J. Wu, "Quantum control of motional states in mixed-species trapped-ion crystals", Ph.D. thesis (University of Colorado at Boulder, 2024) (Cited on pp. 17, 38).

[55] E. R. Clements, "High-stability differential frequency comparisons of optical atomic clocks with correlated laser noise", Ph.D. thesis (University of Colorado at Boulder, 2022) (Cited on pp. 17, 19, 21, 40, 90, 114, 117).

[56] D. F. V. James, "Quantum dynamics of cold trapped ions with application to quantum computation.", Appl. Phs. B **66**, 181 (1998) (Cited on pp. 18, 39).

[57] J.-S. Chen, "Ticking near the zero-point energy: Towards 1 x 10^{-18} accuracy in Al^+ optical clocks", Ph.D. thesis (University of Colorado at Boulder, 2017) (Cited on p. 19).

[58] A. M. Hankin, E. R. Clements, Y. Huang, S. M. Brewer, J.-S. Chen, C. W. Chou, D. B. Hume, and D. R. Leibrandt, "Systematic uncertainty due to background-gas collisions in trapped-ion optical clocks", Phys. Rev. A **100**, 033419 (2019) (Cited on pp. 22, 73).

[59] M. Naftaly and R. Miles, "Terahertz time-domain spectroscopy: A new tool for the study of glasses in the far infrared", Journal of Non-Crystalline Solids **351**, 3341 (2005) (Cited on pp. 28, 32, 73).

[60] J. W. Ekin, *Experimental Techniques for Low-Temperature Measurements* (Oxford University Press, 2006) (Cited on p. 28).

[61] J. Säily and A. V. Räisänen, *Studies on Specular and Non-Specular Reflectivities of Radar Absorbing Materials (RAM) at Submillimetre Wavelengths*, tech. rep. S 258 (Helsinki University of Technology, Department of Electrical and Comuunications Engineering, Radio Laboratory, 2003) (Cited on p. 31).

[62] R. G. Cortiñas, “Laser trapping of cold circular Rydberg atoms for quantum simulation”, Ph.D. thesis (École Normale Supérieure (Paris), 2020) (Cited on p. 31).

[63] M. Fan, C. A. Holliman, X. Shi, H. Zhang, M. W. Straus, X. Li, S. W. Buechele, and A. M. Jayich, “Optical Mass Spectrometry of Cold RaOH$^+$ and RaOCH3$^+$”, Phys. Rev. Lett. **126**, 023002 (2021) (Cited on pp. 35, 99).

[64] D. J. Wineland and W. M. Itano, “Laser cooling of atoms”, Phys. Rev. A **20**, 1521 (1979) (Cited on p. 36).

[65] D. J. Berkeland, J. D. Miller, J. C. Bergquist, W. M. Itano, and D. J. Wineland, “Minimization of ion micromotion in a paul trap”, J. Appl. Phys **83**, 5025 (1998) (Cited on p. 38).

[66] M. Block, P. Seibert, O. Rehm, and G. Erth, “3D5=2 lifetime in laser cooled Ca+: Influence of cooling laser power.”, Eur. Phys. J. D **7**, 461 (1999) (Cited on p. 39).

[67] C. F. Roos, “Controlling the quantum state of trapped ions”, Ph.D. thesis (University of Innsbruck, 2000) (Cited on p. 43).

[68] C. Roos, T. Zeiger, H. Rohde, H. C. Nägerl, J. Eschner, D. Leibfried, F. Schmidt-Kaler, and R. Blatt, “Quantum State Engineering on an Optical Transition and Decoherence in a Paul Trap”, Phys. Rev. Lett. **83**, 4713 (1999) (Cited on p. 43).

[69] F. Diedrich, J. C. Bergquist, W. M. Itano, and D. J. Wineland, “Laser cooling to the zero-point energy of motion”, Phys. Rev. Lett. **62**, 403 (1989) (Cited on p. 43).

[70] C. F. Roos, T. Monz, K. Kim, M. Riebe, H. Häffner, D. F. V. James, and R. Blatt, “Nonlinear coupling of continuous variables at the single quantum level”, Phys. Rev. A **77**, 040302 (2008) (Cited on p. 47).

[71] M. Abe, Y. Moriwaki, M. Hada, and M. Kajita, “Ab initio study on potential energy curves of electronic ground and excited states of 40CaH+ molecule”, Chemical Physics Letters **521**, 31 (2012) (Cited on p. 48).

[72] V. V. Albert, J. P. Covey, and J. Preskill, “Robust Encoding of a Qubit in a Molecule”, Phys. Rev. X **10**, 031050 (2020) (Cited on p. 59).

[73] K.-K. Ni, T. Rosenband, and D. D. Grimes, “Dipolar exchange quantum logic gate with polar molecules”, Chem. Sci. **9**, 6830 (2018) (Cited on p. 59).

[74] L. Christakis, J. S. Rosenberg, R. Raj, S. Chi, A. Morningstar, D. A. Huse, Z. Z. Yan, and W. S. Bakr, “Probing site-resolved correlations in a spin system of ultracold molecules”, Nature **614**, 64 (2023) (Cited on p. 59).

[75] D. K. Ruttley, A. Guttridge, T. R. Hepworth, and S. L. Cornish, “Enhanced Quantum Control of Individual Ultracold Molecules Using Optical Tweezer Arrays”, PRX Quantum **5**, 020333 (2024) (Cited on p. 59).

[76] M. Roguski, A. Shlykov, Z. Meir, and S. Willitsch, “The role of spectator modes in the quantum-logic spectroscopy of single trapped molecular ions”, arXiv:2504.02642 (2025) (Cited on p. 59).

[77] C. M. Holland, Y. Lu, S. J. Li, C. L. Welsh, and L. W. Cheuk, "Demonstration of Measurement-Enhanced State Preparation and Erasure Conversion in a Molecular Tweezer Array", Phys. Rev. X **15**, 031018 (2025) (Cited on p. 59).

[78] M. Teller, V. Messerer, K. Schüppert, Y. Zou, D. A. Fioretto, M. Galli, P. C. Holz, J. Reichel, and T. E. Northup, "Integrating a fiber cavity into a wheel trap for strong ion–cavity coupling", AVS Quantum Science **5**, 012001 (2023) (Cited on p. 59).

[79] E. R. Hudson and W. C. Campbell, "Dipolar quantum logic for freely rotating trapped molecular ions", Phys. Rev. A **98**, 040302 (2018) (Cited on p. 59).

[80] D. Hume, T. Rosenband, and D. J. Wineland, "High-Fidelity Adaptive Qubit Detection through Repetitive Quantum Nondemolition Measurements", Phys. Rev. Lett. **99**, 120502 (2007) (Cited on pp. 60, 99).

[81] S. D. Erickson, J. J. Wu, P.-Y. Hou, D. C. Cole, S. Geller, A. Kwiatkowski, S. Glancy, E. Knill, D. H. Slichter, A. C. Wilson, et al., "High-fidelity indirect readout of trapped-ion hyperfine qubits", Physical Review Letters **128**, 160503 (2022) (Cited on p. 60).

[82] J. Koelemeij, B. Roth, and S. Schiller, "Blackbody thermometry with cold molecular ions and application to ion-based frequency standards", Physical Review A—Atomic, Molecular, and Optical Physics **76**, 023413 (2007) (Cited on p. 68).

[83] A. G. Vaidyanathan, W. P. Spencer, and D. Kleppner, "Inhibited Absorption of Blackbody Radiation", Phys. Rev. Lett. **47**, 1592 (1981) (Cited on p. 74).

[84] D. Irimia, D. Dobrikov, R. Kortekaas, H. Voet, D. A. van den Ende, W. A. Groen, and M. H. M. Janssen, "A short pulse (FWHM) and high repetition rate (dc-5kHz) cantilever piezovalve for pulsed atomic and molecular beams", Rev. of Sci. Inst. **80**, 113303 (2009) (Cited on pp. 77, 78).

[85] M. D. Morse, "2 - Supersonic Beam Sources", in *Atomic, Molecular, and Optical Physics: Atoms and Molecules*, Vol. 29, edited by F. Dunning and R. G. Hulet, Experimental Methods in the Physical Sciences (https://www.sciencedirect.com/science/article/pii/S0076695X0860784X, 1996), pp. 21–47 (Cited on pp. 77, 78, 89).

[86] T. C. Briles, "Production, Deceleration, and Detection of OH Radicals", Ph.D. thesis (University of Colorado at Boulder, 2015) (Cited on pp. 77, 80, 89).

[87] J. P. Valleau and J. M. Deckers, "A study of molecular interactions in molecular beams isolated from the exhaust of supersonic nozzles", Canadian Journal of Chemistry **42**, 225 (1964) (Cited on p. 77).

[88] G. Scoles, *Atomic and Molecular Beam Methods*, Vol. 2 (New York: Oxford University Press, 1988) (Cited on p. 77).

[89] U. Even, "Pulsed Supersonic Beams from High Pressure Source: Simulation Results and Experimental Measurements", Advances in Chemistry **2014**, 636042 (2014) (Cited on p. 78).

[90] C. Meng and M. H. M. Janssen, "Measurement of the density profile of pure and seeded molecular beams by femtosecond ion imaging", Rev. of Sci. Inst. **86**, 023110 (2015) (Cited on p. 78).

[91] J. Chang, J. Coursey, R. Dragoset, A. Kishore, K. Olsen, A. Sansonetti, G. Wiersma, D. Zucker, and M. Zucker, *Electron-Impact Cross Sections for Ionization and Excitation Database*, Standard Reference Database 107 (NIST, 2004) (Cited on p. 82).

[92] S. Opitz, D. Proch, T. Trickl, and K. Kompa, “State-selective ionization of nitrogen by resonance-enhanced three- and four-photon excitation”, Chemical Physics **143**, 305 (1990) (Cited on pp. 85, 91).

[93] A. A. S. Gardner, “Experiments toward high resolution spectroscopy of N_2^+”, Ph.D. thesis (University of Sussex, 2015) (Cited on pp. 85, 87).

[94] A. Lofthus and P. H. Krupenie, “The spectrum of molecular nitrogen”, Journal of PHysica and Chemical Reference Data **6**, 113 (1977) (Cited on p. 85).

[95] Z. Meir, G. Hegi, K. Najafian, M. Sinhal, and S. Willitsch, “State-selective coherent motional excitation as a new approach for the manipulation, spectroscopy and state-to-state chemistry of single molecular ions”, Faraday Discuss. **217**, 561 (2019) (Cited on pp. 89, 93).

[96] A. Landau, Eduardus, D. Behar, E. R. Wallach, L. F. Pašteka, S. Faraji, A. Borschevsky, and Y. Shagam, “Chiral molecule candidates for trapped ion spectroscopy by ab initio calculations: From state preparation to parity violation”, The Journal of Chemical Physics **159**, 114307 (2023) (Cited on pp. 89, 91, 101).

[97] P. Aggarwal, H. L. Bethlem, A. Boeschoten, A. Borschevsky, K. Esajas, Y. Hao, S. Hoekstra, K. Jungmann, V. R. Marshall, T. B. Meijknecht, M. C. Mooij, R. G. E. Timmermans, A. Touwen, W. Ubachs, L. Willmann, Y. Yin, and A. Zapara, “A supersonic laser ablation beam source with narrow velocity spreads”, Review of Scientific Instruments **92**, 033202 (2021) (Cited on pp. 89, 99).

[98] B. C. Sawyer, J. G. Bohnet, J. W. Britton, and J. J. Bollinger, “Reversing hydride-ion formation in quantum-information experiments with Be^+”, Phys. Rev. A **91**, 011401 (2015) (Cited on p. 90).

[99] H. Wu, M. Mills, E. West, M. C. Heaven, and E. R. Hudson, “Increase of the barium ion-trap lifetime via photodissociation”, Phys. Rev. A **104**, 063103 (2021) (Cited on p. 90).

[100] P. C. Schmid, J. Greenberg, T. L. Nguyen, J. H. Thorpe, K. J. Catani, O. A. Krohn, M. I. Miller, J. F. Stanton, and H. J. Lewandowski, “Isomer-selected ion–molecule reactions of acetylene cations with propyne and allene”, Phys. Chem. Chem. Phys. **22**, 20303 (2020) (Cited on pp. 90, 99).

[101] O. A. Krohn, K. J. Catani, J. Greenberg, S. P. SUndar, G. da Silva, and H. J. Lewandowski, “Isotope-specific reactions of acetonitrile ($\mathrm{CH_3CN}$) with trapped, translationally cold CCl^+”, J. Chem. Phys. **145**, 074305 (2021) (Cited on pp. 90, 99).

[102] G. Cazzoli, L. Cludi, G. Buffa, and C. Puzzarini, “PRECISE THz MEASUREMENTS OF HCO^+, $\mathrm{N2H}^+$, AND CF^+ FOR ASTROPHYSICAL OBSERVATIONS”, ApJS **203**, 11 (2012) (Cited on pp. 91, 101).

[103] L. Dimauro and T. A. Miller, “Laser-induced fluorescence of CO+ and the CO a3Πi, state produced by multiphoton absorption in a supersonic jet”, Chemical Physics Letters **138**, 175 (1987) (Cited on pp. 91, 100).

[104] A. P. Singh, M. Mitchell, W. Henshon, A. Hartman, A. Lunstad, B. Kuzhan, and D. Hanneke, “State selective preparation and nondestructive detection of trapped O2+”, The Journal of Chemical Physics **162**, 054203 (2025) (Cited on p. 91).

[105] L. Xu, J. Toscano, and S. Willitsch, “Trapping and Sympathetic Cooling of Conformationally Selected Molecular Ions”, Phys. Rev. Lett. **132**, 083001 (2024) (Cited on p. 99).

[106] D. F. Hagen, “Characterization of Iosmeric Compounds by Gas and Plasma Chromatography”, Analytical Chemistry **51**, 870 (1979) (Cited on p. 100).

[107] M. I. Kabachnik, T. A. Mastryukova, E. I. Fedin, M. S. Vaisberg, L. L. Morozov, P. V. Petrovskii, and A. E. Shipov, “Optical Isomers in Solution Investigated by Nuclear Magnetic Resonance”, Russian Chemical Reviews **47**, 821 (1978) (Cited on p. 100).

[108] D. J. Ashline, A. J. Lapadula, Y.-H. Liu, M. Lin, M. Grace, B. Pramanik, and V. N. Reinhold, “Carbohydrate Structural Isomers Analyzed by Sequential Mass Spectrometry”, Analytical Chemistry **79**, PMID: 17397137, 3830 (2007) (Cited on p. 100).

[109] J. F. Lockyear, O. Welz, J. D. Savee, F. Goulay, A. J. Trevitt, C. A. Taatjes, D. L. Osborn, and S. R. Leone, “Isomer Specific Product Detection in the Reaction of CH with Acrolein”, The Journal of Physical Chemistry A **117**, PMID: 24088057, 11013 (2013) (Cited on p. 100).

[110] M. Wu and P. M. Johnson, “A study of some Rydberg states of CO2 by (3+1) multiphoton ionization spectroscopy”, The Journal of Chemical Physics **91**, 7399 (1989) (Cited on p. 100).

[111] E. Herbst, J. M. Norbeck, P. R. Certian, and W. Klemperer, “Interstellar COH^+”, The Astrophysical Journal **207**, 110 (1976) (Cited on p. 101).

[112] H. Liszt and M. Gerin, “Molecular Hydrogen and its Proxies HCO^+ and CO in the Diffuse Interstellar Medium”, The Astrophysical Journal **943**, 172 (2023) (Cited on p. 101).

[113] H. M. Knaack, “Laser-free operations in a mixed-species trapped ion processor”, Ph.D. thesis (University of Colorado at Boulder, 2024) (Cited on p. 112).

[114] X. Li, F. Zhou, M. Ke, P. Xu, X.-D. He, J. Wang, and M.-S. Zhan, “High-resolution ex vacuo objective for cold atom experiments”, Applied optics **57**, 7584 (2018) (Cited on p. 122).

Appendix A

The Stinger cryogenic system

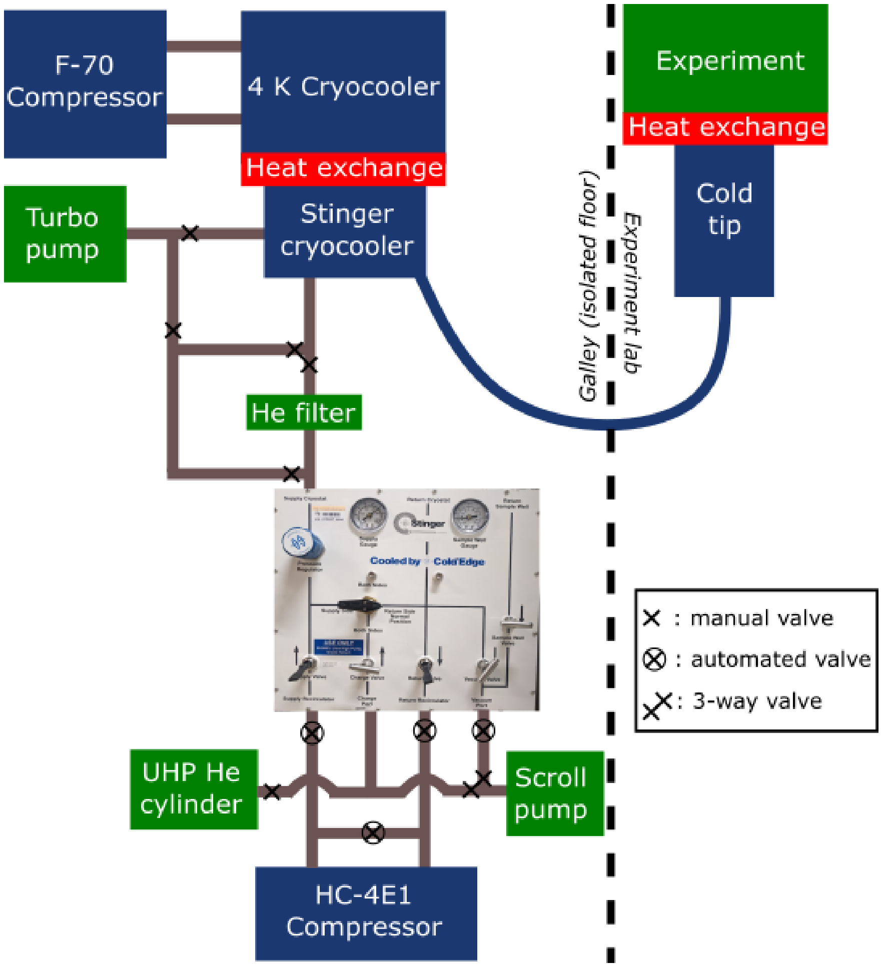

Figure A.1: A schematic of the Stinger system, including both components provided with the commercial system (blue squares and manifold image) and those retrofitted by us (green squares). We have also added a number of valves to the helium and vacuum lines. These allow us to perform a variety of operations, including the unclogging procedures described in the text.

Standard Stinger operating procedures can, of course, be found in the manual provided with the system. However, the Stinger system was not designed to operate continuously at cryogenic temperatures for weeks at a time, as we generally would like to do. When attempting to operate in this mode, the system exhibits a behavior referred to as "clogging," in which the helium flow through the system becomes restricted over some period of time; this is believed to occur due to the accumulation of cryo-pumped contaminants. This can happen suddenly and cause the cold tip temperature to exceed 100 K in a matter of hours if not addressed. Without additional mitigation procedures, our system is observed to clog at least once every six days of cryogenic operation. In order to not experience unexpected clogs, we have had to come up with our own set of procedures, which I will outline below. It should be noted that many of these techniques were pioneered by others; see, e.g., Ref. [113].

We implement the following strategies to mitigate clogging during experimental operation:

- Introducing an adsorbent helium purifier to the Stinger cryocooler helium supply line (see Figure A.1), commercially available from Supelco. This increases our maximum clogging period from 6 to 17 days. The purifier must be regenerated (via a 24-hour, 100°C bake) every month and replaced every 3-4 months. During these procedures, manual valves installed in the helium line allow us to temporarily bypass the filter.

- Running weekly *mini warm-ups* to ∼60 K with the recirculating compressor closed off. This allows the contaminants to degas, at which point they can be pumped away via a scroll pump through the vacuum port of the manifold. These mini warm-ups take about an hour and, after the system has returned to equilibrium, do not significantly affect trapping conditions such as micromotion. We have automated the system with pneumatic valves, serial control of the F-70 compressor, and integrated readout of the cryocooler temperature so that these warm-ups can occur at the click of a button.

- In cases of persistent clogging (such as due to an exhausted filter or accidental contamination), a warm-up to room temperature may be necessary. In extreme cases, the entirety of recirculating helium can be pumped out and replaced.

With a properly-maintained helium filter and regular mini warm-ups we can operate practically indefinitely at cryogenic temperatures.

Appendix B

Experimental control system

Our experimental control system is built in ARTIQ (Advanced Real-Time Infrastructure for Quantum physics). ARTIQ is developed by M-labs, initially in partnership with the Ion Storage Group. Control code is written in Python and compiled onto a Zynq ZC706 FPGA, which routes the FPGA I/O ports to direct digital synthensizers (DDSs), digital-to-analog converters (DACs), and transistor-transistor logic signals (TTLs). DDSs are primarily used to control AOMs; DACs are primarily used to set trap voltages and laser servo setpoints; and TTLs are used for a wide variety of applications, including receiving photon counter signals, pulsing the molecular beam valve, and switching servos on and off. Experiments can be run through a graphical user interface (GUI), which has been programmed for versatile on-the-fly modifications of experimental parameters and provides real-time plotting of experimental results. An example screenshot of the GUI is shown in Fig. B.1.

Control of trap electrode voltage and laser system intensity and frequency output are the primary functions of the control system. Schematics of the RF and DC voltage paths and laser output control (for lasers that employ active intensity servos) are displayed in Fig. B.2. Note that while relative frequency adjustments of the laser systems are provided via DDS outputs to AOMs, absolute frequency stabilization of Ca^+ lasers to a cavity reference is described in Appendix C and Ref. [55].

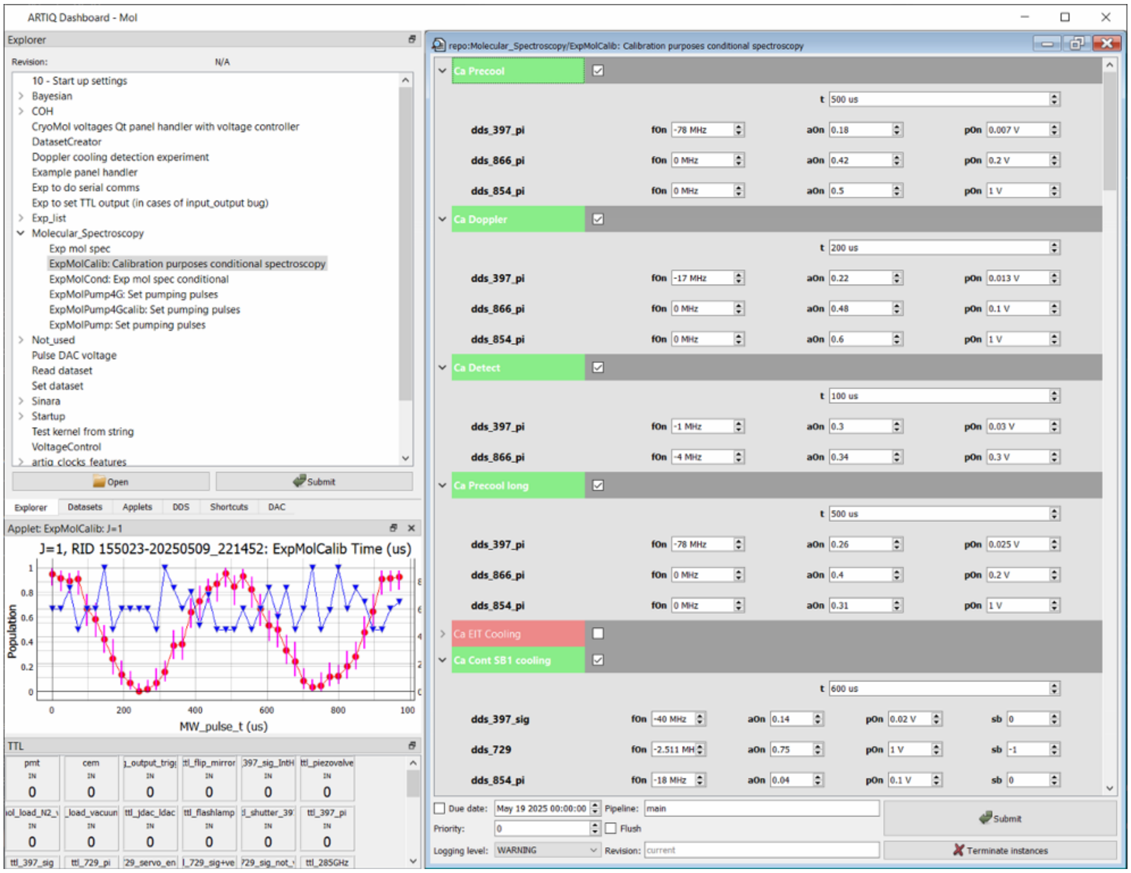

- 10 - Start up settings
- Bayesian
- COH
- CryoMol voltages Qt panel handler with voltage controller
- DatasetCreator
- Doppler cooling detection experiment
- Example panel handler
- Exp to do serial comms
- Exp to set TTL output (in cases of input_output bug)
- Exp_list
- Molecular_Spectroscopy
  - Exp mol spec
  - ExpMolCalib: Calibration purposes conditional spectroscopy
  - ExpMolCond: Exp mol spec conditional
  - ExpMolPump4G: Set pumping pulses
  - ExpMolPump4Gcalib: Set pumping pulses
  - ExpMolPump: Set pumping pulses
- Not_used
- Pulse DAC voltage
- Read dataset
- Set dataset
- Sinara
- Startup
- Test kernel from string
- VoltageControl
- artiq_clocks_features

pmt	cem	j_output_trig	tl_flip_mirror	397_sig_IntH	ttl_piezovalve
IN 0	IN 0	IN 0	IN 0	IN 0	IN 0
iol_load_N2_	**_load_vacuun**	**ttl_jdac_ldac**	**ttl_flashlamp**	**l_shutter_39**	**ttl_397_pi**
IN 0	IN 0	IN 0	IN 0	IN 0	IN 0
ttl_397_sig	**ttl_729_pi**	**29_servo_en**	**l_729_sig+ve**	**729_sig_not_**	**ttl_285GHz**

Ca Precool ☑

t 500 us

	fOn	aOn	pOn
dds_397_pi	-78 MHz	0.18	0.007 V
dds_866_pi	0 MHz	0.42	0.2 V
dds_854_pi	0 MHz	0.5	1 V

Ca Doppler ☑

t 200 us

	fOn	aOn	pOn
dds_397_pi	-17 MHz	0.22	0.013 V
dds_866_pi	0 MHz	0.48	0.1 V
dds_854_pi	0 MHz	0.6	1 V

Ca Detect ☑

t 100 us

	fOn	aOn	pOn
dds_397_pi	-1 MHz	0.3	0.03 V
dds_866_pi	-4 MHz	0.34	0.3 V

Ca Precool long ☑

t 500 us

	fOn	aOn	pOn
dds_397_pi	-78 MHz	0.26	0.025 V
dds_866_pi	0 MHz	0.4	0.2 V
dds_854_pi	0 MHz	0.31	1 V

Ca EIT Cooling ☐

Ca Cont SB1 cooling ☑

t 600 us

	fOn	aOn	pOn	sb
dds_397_sig	-40 MHz	0.14	0.02 V	0
dds_729	-2.511 MH	0.75	1 V	-1
dds_854_pi	-18 MHz	0.04	0.1 V	0

☐ Due date: May 19 2025 00:00:00

Pipeline: main

Priority: 0

☐ Flush

Logging level: WARNING

Revision: current

Figure B.1: A screenshot of the ARTIQ GUI. Panels allowing for experiment selection, modification of experiment parameters, TTL control, and real-time display of current experiment results can be seen.

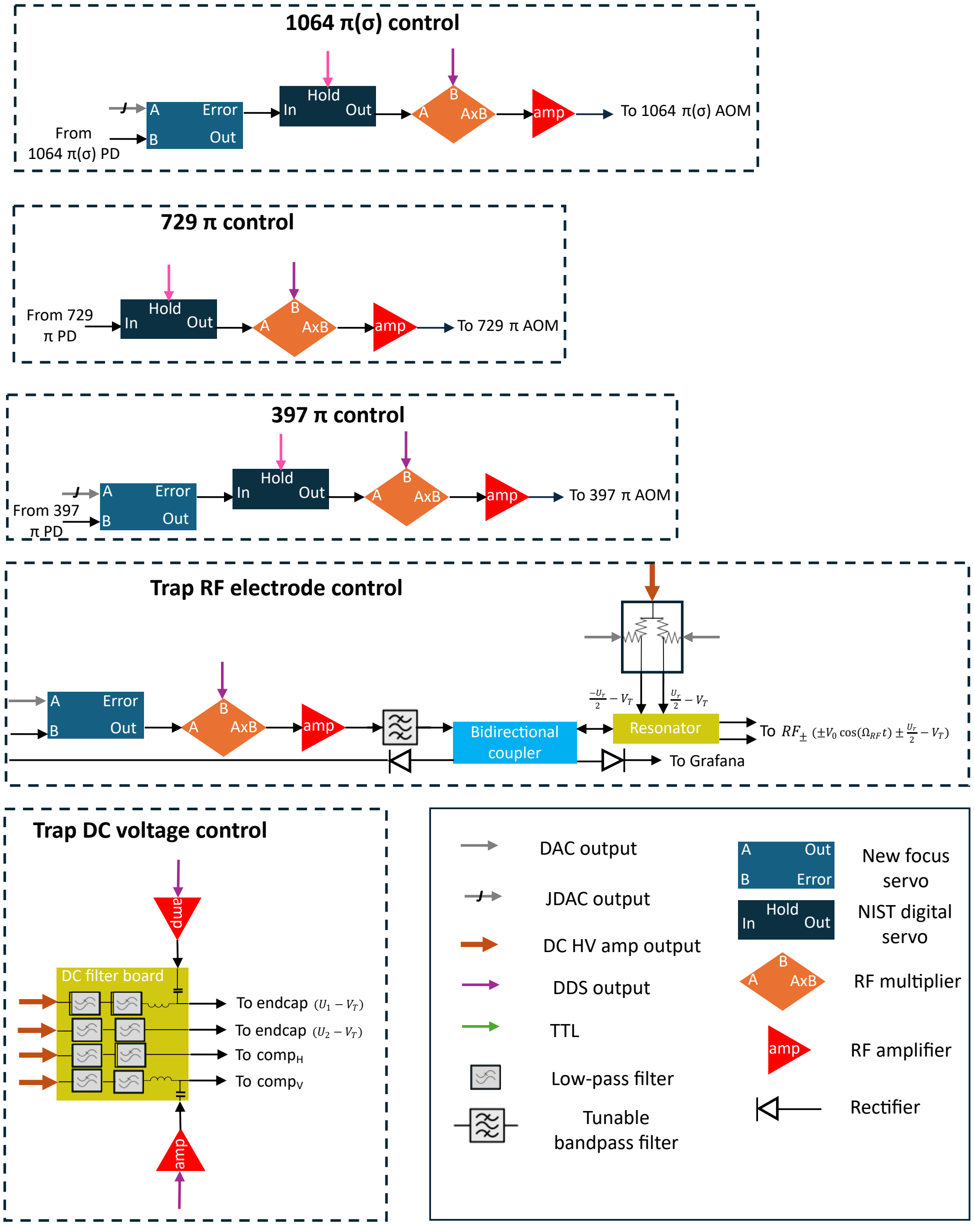

Figure B.2: Schematics showing control of select laser system output and trap voltages. Photodiode (PD) signals are obtained using beam pick-offs near the trap chamber (see Appendix C). All trap electrodes have a common bias $-V_T$ applied in order to maximize the dynamic range of voltage differential between the RF electrodes and the endcap electrodes. Grafana is a data logging software.

Appendix C

Optical systems

Manipulating the quantum states of ions in our experiment requires delivering coherent electromagnetic radiation, primarily in the form of laser light. In this section, I will note the lasers that generate this light, the mechanisms we use to stabilize the frequency of the light, and the systems used to precisely control the frequency, amplitude, and timing of the light that is ultimately delivered to the ion.

C.1 Lasers

At the core of the optical system is a series of commercially available lasers. All of the lasers addressing Ca^+ are located or referenced to lasers in a neighboring Ion Storage Group lab–this lab will henceforth be referred to by its room number, 1H116. Each of these lasers is ultimately referenced to an optical spherical cavity in 1H116. For more details on the Ca^+ lasers and locks in 1H116, see Ref. [55].

The lasers used to address our ion are as follows:

- **397 nm laser:** A Toptica ECDL that can output up to 15 mW. To stabilize the laser frequency, the beatnote between this laser and the 397 nm laser in 1H116 is frequency-locked to 20 MHz via a NIST digital servo box, which feeds back to the laser current for fast compensation and to the laser piezo voltage for slow compensation.

- **729 nm laser:** A Toptica ECDL/TA PRO that can output up to 500 mW. To stabilize the laser frequency, the beatnote between this laser and the 729 nm laser in 1H116 is phase-locked to a ∼1 GHz signal provided by an HP digital synthesizer; fiber noise cancellation has been added to the trans-lab fiber. A Toptica FALC module performs the fast current lock, while a digital servo box provides the slow piezo voltage lock. The ISG room-temperature molecule apparatus has the ability to use measurements on a trapped Ca^+ to feedback directly to an AOM in the optical path of the 1H116 729 nm laser, compensating for slow drifts in cavity parameters.

- **854 and 866 nm lasers**: Both wavelengths of repumping light are taken directly from lasers in 1H116. The 854 nm laser is a Photodigm distributed feedback laser and the 866 nm laser is a Toptica ECDL.
- **1064 nm laser:** The laser generating our Raman beams is an IPG fiber laser that can output up to 5 watts. Since only the relative detuning of the different paths of this laser matters, the absolute frequency does not need to be stabilized.

C.2 AOM boards, beam launchers, and imaging

For space efficiency, ease of use, and alignment stability, we have built all of our AOM optical paths on custom-machined aluminum boards. Each board is 22" x 16" x 0.5” aluminum, holds 2-3 AOMs, and uses 0.5” Polaris optical mounts. All light is fiber coupled on and off the boards. Beams are sent through their corresponding AOMs in a double-passed manner to increase the achievable bandwidth and so that fiber coupling efficiency is not significantly affected by changing the AOM frequency. The AOM board layout is detailed in Fig. C.1, and a picture of the 729 AOM board is included in Fig. C.2. A few more details about each board are as follows:

- **397 board:** This board contains 3 AOMs corresponding to 3 output fibers, but we typically only use the 1st and 3rd (leading to the σ and π port, respectively; the 2nd has been aligned in the past for testing purposes). The 0th order is "recycled", meaning that if the 1st AOM is not receiving RF power, the beam passes along to the 2nd AOM, etc. The complications of this are that if certain optics are adjusted in a particular path, everything downstream must also be adjusted. Additionally, if multiple AOMs are on at the same time, the output power of the downstream AOMs will depend on the deflection efficiency of the previous AOM(s). However, no experiments that we run require different 397 nm beams to be on at the same time.

An additional feature of this board is that the 0th order that passes all the way through all AOMs is retroreflected to the π-port fiber upon actuation of a mechanical shutter. This light is effectively ∼400 MHz red-detuned from the $|S_{1/2}\rangle \leftrightarrow |P_{1/2}\rangle$ transition. Sending this light to the ion during the loading process leads to greatly improved loading efficiency; see Section 3.2.1 for more details.

- **854 + 866 board:** This board has 2 inputs and 2 outputs, one for each wavelength. Both outputs are sent to the 729 board.
- **729 board:** This board has 3 AOMs and corresponding output fibers, which go to the π, σ, and vertical ports, respectively. The 854 and 866 nm beams are combined using dichroics with each other and then with the 729 beam deflected by the first AOM such that they all go through the same fiber leading to the π port. Like the 397 board, the subsequent 729 AOMs use recycled 0th-order light.
- **1064 board:** This board takes as input the fiber leading directly from the fiber laser; light goes through 2 AOMs and corresponding output fibers, leading to the π and σ ports. However, the recycling strategy cannot be used in this case because the beams are used simultaneously to drive Raman transitions. Instead, the input beam is split with a ∼60:40 beamsplitter.

All of the AOM outputs are sent to one of two custom-designed aluminum “beam launcher” breadboards located at the π and σ ports where they are combined and sent to the ion (with the exception of the 729 nm vertical beam, which is sent through the imaging port). The beam launcher board is mounted on a motorized translation stage for alignment to the ion. The 397-nm beampaths

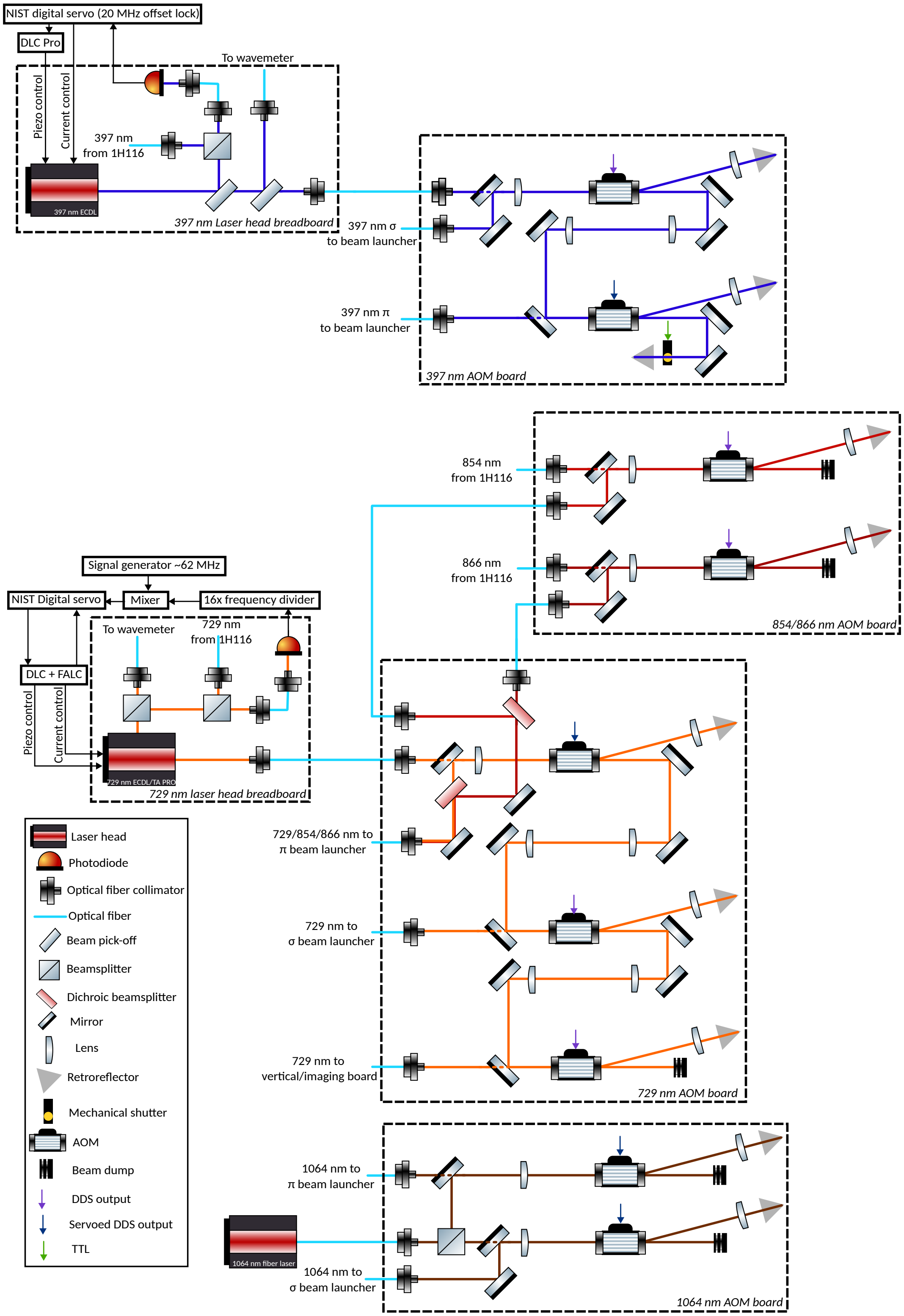

Figure C.1: A diagram showing the optical path of each of the lasers through the AOM boards. After being coupled off the board, they all lead to beam launchers at the experiment chamber, as shown in Fig. C.3.

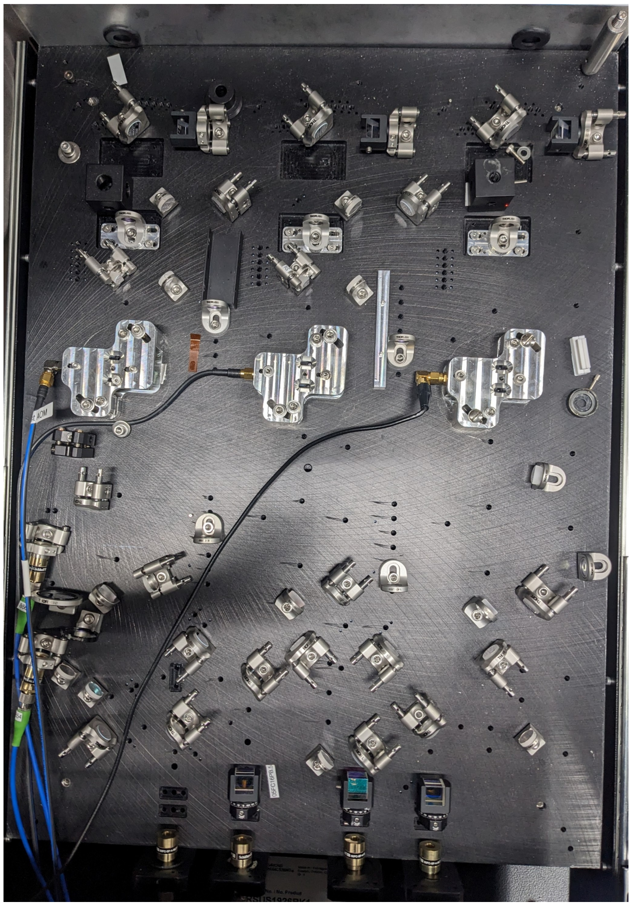

Figure C.2: A picture of the 729 AOM board.

include a PBS and a 50:50 pickoff to a photodiode for intensity servoing; the 397 σ beampath also includes $\lambda/4$ and $\lambda/2$ waveplates. The 729 π and σ beampaths include a beam sampler pickoff for intensity servoing. The 397 and 729 σ beams are not currently servoed. Each 1064 nm beam is expanded to $\sim$12-mm diameter to reduce the beam waist (and thus increase intensity) at the ion, reflected off a gold-coated mirror to minimize polarization fluctuations, and then sent through $\lambda/4$ and $\lambda/2$ waveplates. The 1064 nm collimating lenses are mounted on a motorized translation stage so that these beams can be aligned independently of the Ca^+ beams. Reflections from the dichroics combining the 1064 nm and Ca^+ beams are used to servo the 1064 nm beam intensity. Once combined, all beams at each launcher are sent through a broadband doublet lens ($f = 150$ mm) to the ion. A schematic of the beam launchers is shown in Fig. C.3.

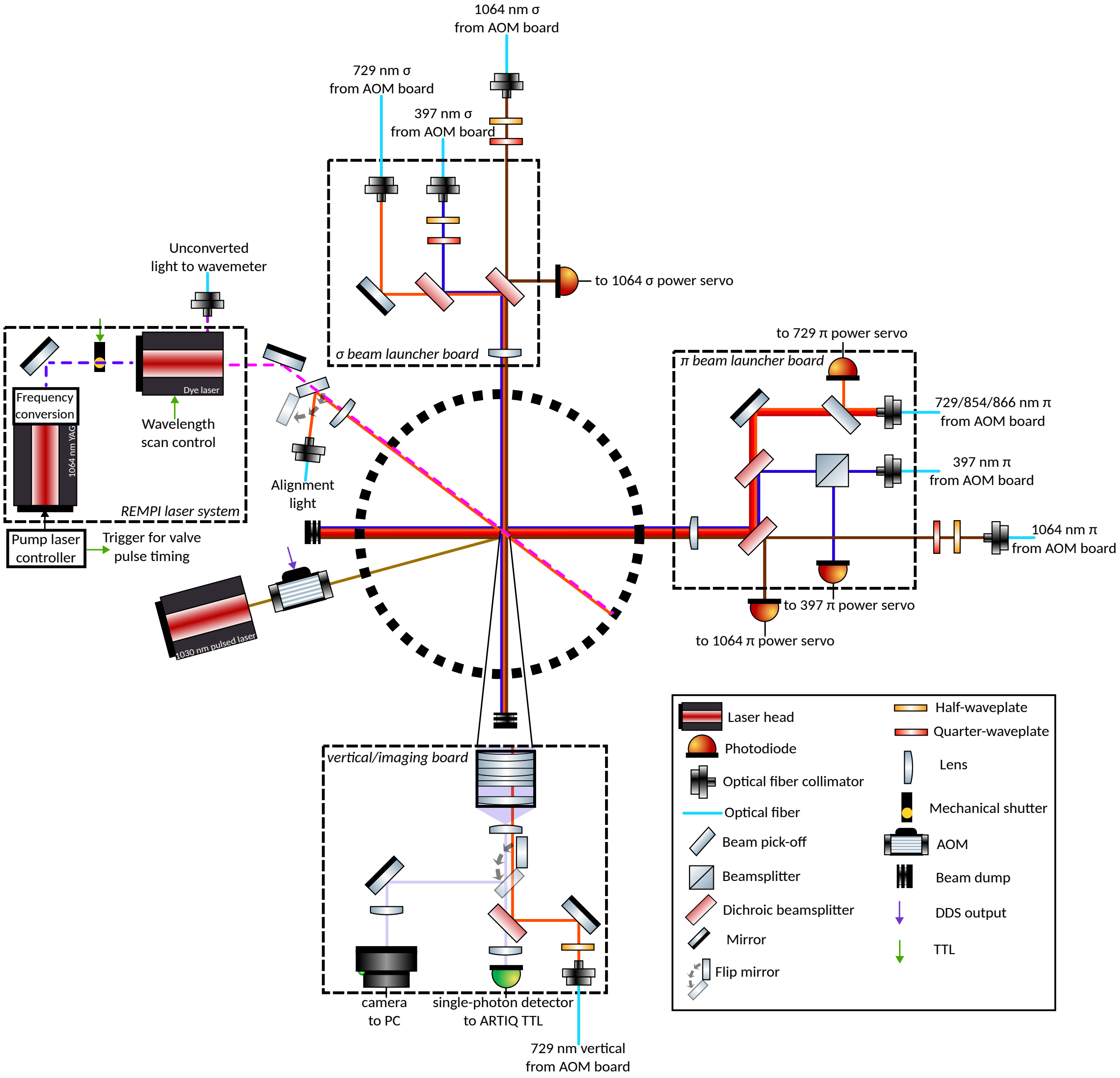

Figure C.3: A diagram showing the optical paths leading to and from the ion.

The imaging system collects photons emitted from the ion from above through a re-entrant viewport designed for high numerical aperture (NA) and thus photon collection efficiency. A 2”-diameter multi-element lens system custom-designed using Zeemax to compensate for aberrations from the in-vacuum windows and viewport (design adapted from Ref. [114]) collimates the photons before they are sent to either the single photon detector or the camera. A PBS allows the vertical 729 nm beam to be sent through the same set of optics to the ion. This beam must be offset from center to avoid being blocked by the trap chip.